



**Epitaxial Sm-Co Thin Films  
Growth, Texture and Magnetic  
Properties**



---

Aarti Singh



# **Epitaxial Sm-Co Thin Films Growth, Texture and Magnetic Properties**

DISSERTATION

for the partial fulfillment of the requirements  
for the academic degree of

Doctor rerum naturalium  
(Dr. rer. nat.)

by

**M.Sc. M. Tech. Aarti Singh**  
born on 20th May 1978 in Panjim, India

submitted to  
Faculty of Mathematics and Natural Sciences  
Technical University Dresden

2006

### **Bibliografische Information Der Deutschen Bibliothek**

Die Deutsche Bibliothek verzeichnet diese Publikation in der Deutschen Nationalbibliografie; detaillierte bibliografische Daten sind im Internet über <http://dnb.ddb.de> abrufbar.

1. Aufl. - Göttingen : Cuvillier, 2006  
Zugl.: (TU) Dresden, Univ., Diss., 2006

ISBN 13: 978-3-86727-107-3

1. Gutachter: Prof. Dr. L. Schultz
2. Gutachter: Prof. Dr. D. Givord
3. Gutachter: Prof. Dr. H. Kronmüller

Eingereicht am: 28. 04. 06

Tag der Verteidigung: 04 .09 .06

© CUVILLIER VERLAG, Göttingen 2006  
Nonnenstieg 8, 37075 Göttingen  
Telefon: 0551-54724-0  
Telefax: 0551-54724-21  
[www.cuvillier.de](http://www.cuvillier.de)

Alle Rechte vorbehalten. Ohne ausdrückliche Genehmigung des Verlages ist es nicht gestattet, das Buch oder Teile daraus auf fotomechanischem Weg (Fotokopie, Mikrokopie) zu vervielfältigen.

1. Auflage, 2006

Gedruckt auf säurefreiem Papier

ISBN 13: 978-3-86727-107-3

## Abstract

The work in this thesis focusses on preparation of epitaxial Sm-Co thin films using pulsed laser deposition with the purpose of obtaining highly textured samples with good hard magnetic properties that are suitable for detailed magnetic measurements and for basic understanding of the magnetic processes happening inside the material.  $\text{Sm}_2\text{Co}_7$  and  $\text{SmCo}_5$  samples were prepared on different orientations of single crystal MgO substrates in order to obtain different but well regulated textures of the magnetic easy axis in these films.

The epitaxial films were suitable for performing magnetisation measurements such as coercivity analysis using the micro-magnetic model (temperature dependent and angular dependent coercivity analysis) and investigating recoil loops. These magnetic measurements correlate the globally observed magnetic properties of the bulk sample with the intrinsic properties of the material and the sample microstructure namely the grain sizes, defect structure and are capable of probing the kind of magnetic interaction present. A very good agreement has been obtained between the measured and predicted angular dependence of coercivity for a pinning controlled magnetisation reversal.

## Kurzfassung

Der Schwerpunkt dieser Dissertationsarbeit ist die Präparation dünner epitaktischer Sm-Co-Schichten mittels gepulster Laserdeposition mit dem Ziel, sehr gut texturierte Proben mit guten magnetischen Eigenschaften zu erhalten, die damit erlauben über detaillierte magnetische Messungen die mikroskopischen Magnetisierungsprozesse im Inneren des Materials zu verstehen.  $\text{Sm}_2\text{Co}_7$ - und  $\text{SmCo}_5$ -Proben wurden auf unterschiedlich orientierten MgO-Einkristallsubstraten präpariert, um unterschiedliche, aber wohlorientierte Anordnungen der magnetisch leichten Achse einzustellen.

Die epitaktischen Schichten eigneten sich für die Untersuchung der Magnetisierungsprozesse mittels Koerzitivitätsanalyse nach dem mikromagnetischen Modell (temperatur- und winkelabhängige Koerzitivfeldmessungen) und zur Untersuchung von inneren Hystereseschleifen. Diese magnetischen Messungen korrelieren die globalen magnetischen Eigenschaften der Probe mit den intrinsischen Eigenschaften des Materials und mit der speziellen Mikrostruktur, insbesondere mit mittlerer Korngröße und Defektstruktur, und ermöglichen die Aufklärung der auftretenden magnetischen Wechselwirkungen. Unter der Annahme eines pinning-kontrollierten Entmagnetisierungsprozesses wurde eine sehr gute Übereinstimmung zwischen der gemessenen und der erwarteten Winkelabhängigkeit der Koerzitivfeldstärke gefunden.

# Contents

<b>1</b>	<b>Introduction</b>	<b>6</b>
<b>2</b>	<b>Rare-Earth (R) Transition Metal (T) Magnets</b>	<b>11</b>
2.1	3d-4f Magnetism in R-T Intermetallics . . . . .	11
2.2	Magnetic Anisotropy . . . . .	12
2.3	Origin of Coercivity . . . . .	15
2.3.1	Micro-magnetic Model . . . . .	17
2.3.2	Confirmation of Pinning . . . . .	20
2.4	Intergranular Exchange Coupling . . . . .	22
2.4.1	Recoil Loops . . . . .	23
2.4.2	Inter-grain Interactions – $\delta J$ Plot/Henkel Plot . . . . .	23
2.5	The Sm-Co System – An Introduction . . . . .	24
2.6	Review: Magnetisation Reversal – Rotational or Non-Rotational Processes? . . . .	28
2.7	Review: Remanence Measurements . . . . .	30
<b>3</b>	<b>Thin Film Structures</b>	<b>32</b>
3.1	Growth Modes – Nucleation to Continuous Films . . . . .	32
3.2	Epitaxial Thin films . . . . .	33
3.3	Review: Sm-Co Thin Film Growth . . . . .	35
3.3.1	Textured Sm-Co Films . . . . .	35
3.3.2	Epitaxial Sm-Co Films . . . . .	37
<b>4</b>	<b>Film Preparation and Characterisation Techniques</b>	<b>39</b>
4.1	Pulsed Laser Deposition . . . . .	39
4.2	Phase and Texture Analysis . . . . .	41
4.3	Microscopical Investigations . . . . .	45
4.4	Magnetic Measurements . . . . .	47
<b>5</b>	<b>Growth and Epitaxial Relation of Sm-Co Films on Different Substrates</b>	<b>49</b>
5.1	Sm-Co Films on MgO (100) Single Crystal Substrates . . . . .	49

5.1.1	Growth of Sm <sub>2</sub> Co <sub>7</sub> Phase . . . . .	50
5.1.2	Growth of SmCo <sub>5</sub> Phase . . . . .	60
5.1.3	Stoichiometric Variation of Co Content . . . . .	64
5.2	SmCo <sub>5</sub> Films on MgO(110) Single Crystal Substrates . . . . .	66
5.2.1	Analysis and Optimisation of Cr Buffer . . . . .	67
5.2.2	Epitaxial SmCo <sub>5</sub> Films on Improved Cr Buffer . . . . .	70
5.3	Sm <sub>2</sub> Co <sub>7</sub> Films on IBAD MgO(100) Buffered a-Si Substrates . . . . .	71
5.4	Summary and Discussion of Epitaxially Prepared Sm-Co Films . . . . .	75
<b>6</b>	<b>Magnetisation and Demagnetisation Mechanism</b>	<b>78</b>
6.1	Magnetisation Reversal - Coherent Rotation, Nucleation or Pinning Dominated? . .	78
6.1.1	Angular Dependence of Coercivity . . . . .	79
6.1.2	Micro-Magnetic Model . . . . .	82
6.2	Verification of Intergranular Exchange Coupling . . . . .	90
6.2.1	Measurement of Recoil Loops - $\delta J$ Plot . . . . .	91
6.2.2	Summary and Discussion on Intergranular Coupling . . . . .	95
<b>7</b>	<b>Conclusions and Future Work</b>	<b>97</b>
	<b>Bibliography</b>	<b>101</b>
	<b>Publication List</b>	<b>110</b>
	<b>Acknowledgements</b>	<b>111</b>

# 1 Introduction

Ferromagnets are materials that show long-range magnetic order at the atomic level resulting in parallel alignment of unpaired electron spins within small magnetic regions called *magnetic domains*. The magnetic moment within a domain is the *spontaneous magnetisation* of the material and even exists in the absence of any externally applied field (only below a certain critical temperature called the *Curie temperature*  $T_C$ , which is an intrinsic property of the material), making ferromagnetic materials unique in their existence. Although spontaneous magnetisation exists in these materials, there is no net magnetic moment for a bulk sample due to random orientation of these tiny magnetic domains with respect to each other. However, once exposed to external magnetic fields, they exhibit high magnetisation due to alignment of the magnetisation in different magnetic domains along the applied field direction. Depending on whether the ferromagnets retain their high magnetisation after removal and reversal of the applied field direction, they may be classified as hard or soft ferromagnets. The soft ferromagnets are ferromagnetic materials that reverse their magnetisation direction almost as soon as the direction of applied field is reversed exhibiting very *low coercivities* (reverse field at which magnetisation is zero) and no *magneto-crystalline anisotropy* as opposed to hard magnets which display very high coercivities. *Permanent magnets / hard magnets* are ferromagnetic material that retain their magnetisation once exposed to strong external fields up to large reverse fields and thereby exhibit large *hysteresis* in their magnetic properties. These are normally characterised with a high value of the magnetic energy product,  $(BH)_{\max}$ , which is a measure of the magnetic energy they can retain. Hence, a permanent magnet can be taken in close analogy to the mechanical spring, which stores mechanical energy whereas a permanent magnet stores magnetic energy [Kir96]. The rare-earth (*R*) compounds are a special class of permanent-magnet systems, which often achieve high  $(BH)_{\max}$ .

The name 'rare earth' is a misnomer and originated from scarcity of the element (rare) and the difficulty of extracting these elements from their ores (earth), neither of which is true any more. Discovered in the 1960-70 decade (Fig. 1.1), the rare-earth compounds have proven themselves to be potentially much stronger for permanent-magnet applications than the then-famous Ferrite magnets or the AlNiCos. The maximum energy products achievable with some of the present day rare earth compounds (300–400 kJ/m<sup>3</sup>) are many orders of magnitude higher than those for the AlNiCo magnets. The magnetism of the rare earths has been known for several years [Tro90] and particularly their high anisotropy fields [Rad87]. However, the low Curie temperature for all of

these elements (well below room temperature – where Gd is an exception with Curie temperature  $\simeq 20^\circ\text{C}$ ) makes them less attractive for isolated usage as permanent magnets. Alloying these elements with the high-magnetisation, high Curie temperature transition metals ( $T$ ) results in very attractive permanent-magnet applicants. Some among the popular  $R$ - $T$  systems are the Sm-Co compounds, Nd-Fe-B magnets and the Sm-Fe-N system, which have been exploited both in bulk as well as for thin film applications.

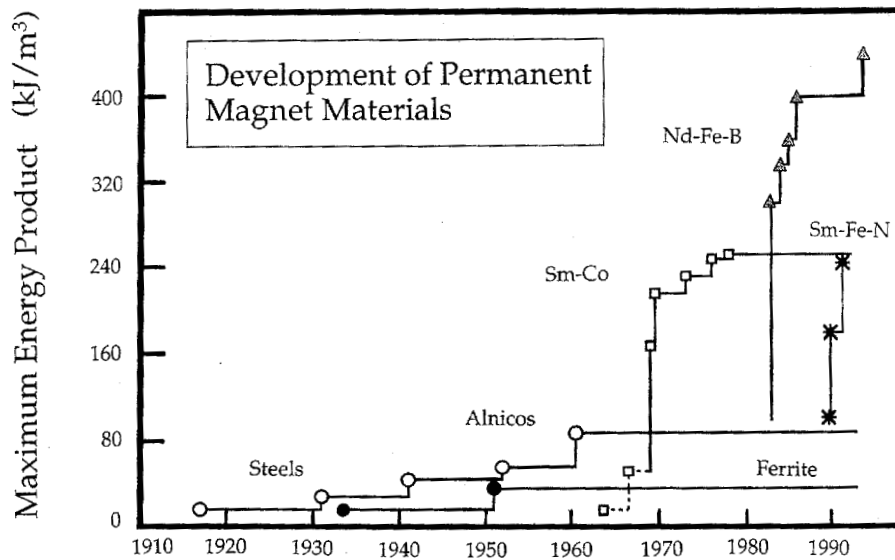


**Fig. 1.1:** The improvement in the magnetic energy product over the last century [Coe96].

A permanent magnet promising high  $(BH)_{\max}$  requires high remanence, high coercivity and a well known magnetisation reversal process, all of which must be stable up to high operating temperatures. The upper bound on these properties is superimposed by a crucial interplay between the intrinsic properties of the materials (namely the saturation moment, which decides the maximum remanence that can be obtained, the anisotropy field, which limits the coercivity in the material, and the Curie temperature, which decides the maximum operating temperature of the magnet) and the processed microstructure. Hence, the evolution of novel materials needs a thorough insight into the intrinsic properties of the magnetic material and the processing techniques responsible for a suitable microstructure.

The best exploitation of saturation magnetisation (single domain magnetisation value) in a uniaxial magnet can be done if the material is extremely well textured, such that the whole sample even though still a multi-grain, multi-domain ensemble, behaves essentially as a single grain entity. More appropriately or practically, the realisation of a “single grain” system would be equivalent to a highly textured material, where the grain misalignment is tolerably tiny. In this case, epitax-

ial films are one very plausible solution. Additionally, an epitaxial growth that forces the easy magnetisation axis to be aligned along only one substrate axis, would bring the system exhibiting uni-axial anisotropy closest to its natural state and suitable for any further investigations. This film as a highly textured magnet has a remanent moment equal to the saturation moment along the easy axis as depicted in Fig. 1.2 and the hard axis contains no remanence or ideally no hysteresis. The realisation of nicely textured films where all the magneto-crystalline energy is stored only along one easy axis was one important task of this work.

The permanent magnet material under investigation is the Sm-Co system. Figure 1.1 confirms the capability of Sm-Co compounds in providing extremely high  $(BH)_{\max}$ , surpassed only by the Nd-Fe-B magnets. A complementary Curie temperature,  $T_C$ , of Sm-Co magnets (above room temperature for all Sm-Co phases) makes them very suitable for high temperature applications. In this work, Sm-Co films were investigated on different substrates. The knowledge of substrate symmetry was exploited, to manoeuvre the growth and orientation of the easy axis (c-axis in Sm-Co) towards a uniaxial growth. Textured films with a remanence as high as 91% of the saturation magnetisation could be achieved on MgO(110) single crystal substrates. A complete overview of the properties, phases and the work done on Sm-Co may be found in chapter 3.

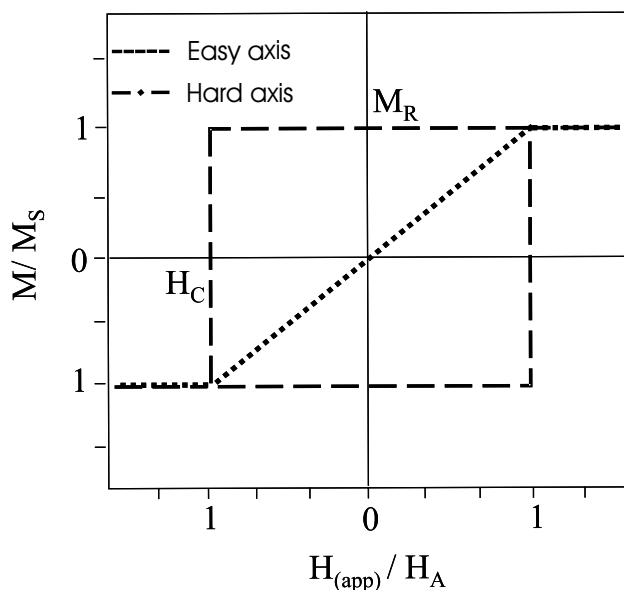


**Fig. 1.2:** Hysteresis in an ideal ferromagnet as a  $M$ - $H$  loop along the easy magnetisation axis (large  $H_C$  and high  $M_R$ ) and hard magnetisation axis.

An equally important requirement for high performance hard magnets is to have a high coercivity, which may be modified by tuning the microstructure (depending on the switching mechanism). An ideal microstructure resulting in high coercivities would require small grain sizes and sufficient pinning sites (for the particular case of Sm-Co films where pinning will be shown to be the magnetisation reversal mechanism) to cause as hard a switching as possible. Pinning defects block

domain walls from expanding freely into the hard phase after an easy nucleation and, hence, lead to coercivities that are typically higher than the nucleation fields. And therefore, the higher the density of these defects, the more effective would be pinning in the system, to a first approximation. A schematic microstructure is presented in Fig. 1.3 showing the mechanism of nucleation and pinning in hard magnets. Regions A, B and C present areas where easy nucleation of a reverse domain occurs and the magnetisation is reversed. However, inhomogeneities present in the system shown as pinning centres close to region C, hinder free expansion of this reversed domain, resulting in a delayed overall reversal of the entire sample magnetisation and therefore result in higher coercivities. The magnetisation reversal in the sample in this case is pinning controlled and can be visualised with the help of schematic 1.3b. The domain wall tries to smoothly sweep through the entire sample dimensions causing the already reversed domain to increase in size and the entire sample magnetisation to reverse. But as soon as it encounters a pinning center or a defect in the material where the regular crystal structure is disrupted, the energy barrier for the domain wall to pass through is higher and the domain wall is trapped or pinned until sufficient energy is available to overcome this increased barrier presented by the defect site. Hence, the magnetisation reversal is delayed and occurs at higher externally applied fields. The realisation of this microstructure which contains sufficient effective pinning sites depends on processing kinetics and nature of intrusions/defects introduced.

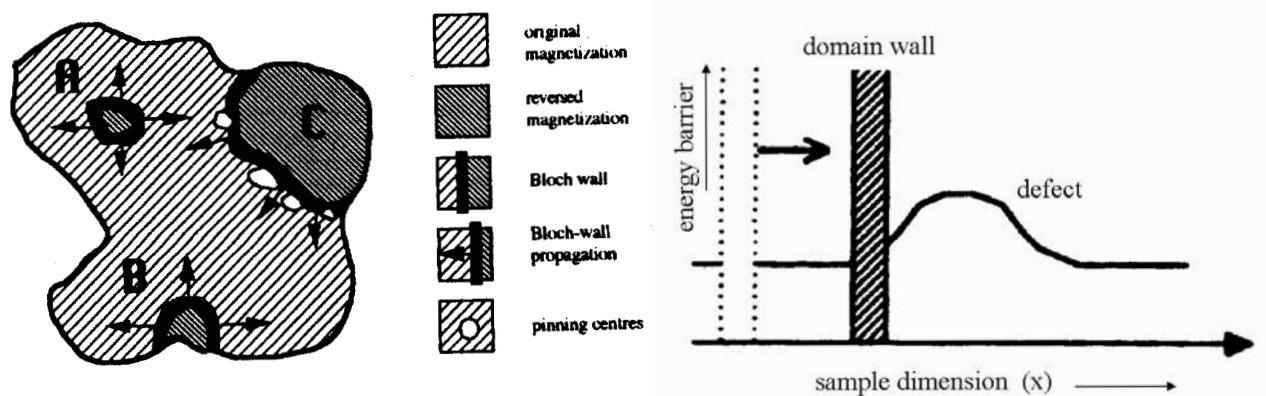


**Fig. 1.3:** (a) Hard grain with regions A, B and C showing schematically the beginning of a nucleation process and pinning of a domain wall at pinning sites. (b) Schematic of a domain wall pinned at a defect site due to increased energy barrier at the defect site [Sko99].

However, even in the best case of most effective pinning, the achievable coercivities are restricted to a third of the total anisotropy field of the magnet (the theoretical externally applied magnetic field at which the magnetisation reversal of the sample occurs) [Kro87]. This limit for a system like  $\text{SmCo}_5$  (with anisotropy fields = 30 T) would still predict exorbitantly high coercivity values of more than 10 T. Surprisingly  $H_C \sim 10$  T has never been observed for  $\text{SmCo}_5$  and even

the highest reported values are well over a factor 3 smaller than these predicted values [Pra99], [Zho00], [Liu02]. This suggests that there still exists a huge room for enhancing the “High” and “Giant” coercivities to even gigantic numbers.

The aim of this work is the preparation of epitaxial hard-magnetic Sm-Co thin film magnets with optimum growth conditions to achieve the best combination of coercivity, remanence and energy products and making a sincere attempt towards correlating the observed global macroscopic properties with the basic magnetisation processes at the microscopic level. Chapter 2 describes the origin of magnetism in these *R-T* compounds, followed by a brief discussion of their intrinsic properties (anisotropy field and constants), hysteresis loop, the origin of coercivity and the models available for understanding magnetisation reversal mechanisms. It continues with the basic demagnetisation process for exploring the possibility of intergranular exchange coupling and finally an introduction to one special phase of the *R-T* system – the Sm-Co system. Hence, this chapter essentially builds up the necessary infrastructure for subsequent discussion of results in chapter 5 and 6. Chapter 2 is concluded with an overview of the reports available on analysing and interpreting hysteresis loops to get information on magnetisation reversal and inter-grain exchange coupling.

Since a very balanced part of the work focusses on obtaining epitaxial thin films, chapter 3 engages itself with processes involved during thin film deposition, starting with fundamentals of nucleation to factors deciding the growth of continuous films. A short recap into physics of epitaxial films follows thereafter touching only relevant aspects which arise later in chapter 5. This chapter is concluded with a short review on the current status of Sm-Co thin film development.

The experimental techniques involved in the course of this work are fairly described in chapter 4. Chapter 5 contains the main results and discussions pertaining to epitaxial growth of Sm-Co thin films on single-crystal substrates of different orientations using pulsed laser deposition. Chapter 6 is restricted to magnetic measurements that subdivide into analysing the mechanism of magnetisation reversal in these thin-film magnets and evaluating the presence of intergranular exchange coupling through measurement of recoil magnetisation loops and constructing  $\delta J$  plots. A concise conclusion chapter summarises the most important scientific work of this thesis.

## 2 Rare-Earth (R) Transition Metal (T) Magnets

The following chapter focusses on the briefest introduction to some of the basic concepts of  $R$ - $T$  magnetism which are relevant for a successful discussion of results of this work. Through each of these sections, references have been made from [Cul72] for basic understanding of magnetism and [Coe96], [Sko99], [Tre05] for more specialised themes of  $R$ - $T$  magnetism.

### 2.1 3d-4f Magnetism in R-T Intermetallics

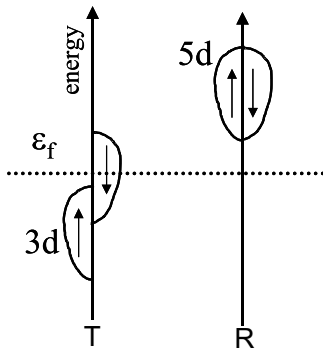


**Fig. 2.1:** 3d and 5d bands of the transition element and rare earth [Tre05].

Magnetic coupling in  $R$ - $T$  compounds is studied by many groups worldwide [Cam72], [Cad87b], [Ric98], [Rad02] due to the interesting phenomenon. The magnetism in these complex intermetallics arises from the coupling between partially filled 3d shells of the transition metal and the 4f of the rare-earth system. Several approaches towards understanding this magnetism have been proposed, but the one from Campbell in 1972 [Cam72], regarding the intervention of 5d electrons of the rare-earth elements, has been most widely accepted.

The overall coupling is then visualised as a superposition of coupling between the 4f and 5d orbital of the rare earth (intra-atomic coupling) and a second contribution coming from the coupling between the 5d orbital of the rare earth and the 3d orbital of the transition metal (inter-atomic coupling). The 4f-5d coupling (intra-atomic coupling) is always ferromagnetic. The 3d-5d coupling (inter-atomic coupling) occurs through hybridisation of these orbitals. This overlap between the 5d $\downarrow$  orbital states with those of

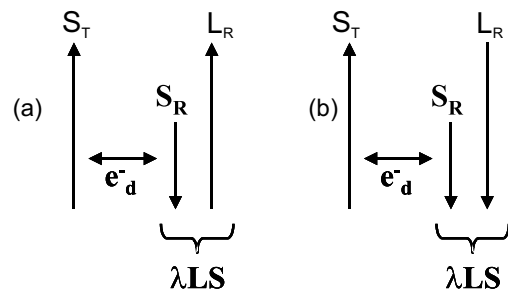


**Fig. 2.2:** Total angular momenta of the (a) light and (b) heavy rare earth (R) and the transition metal (T) elements showing that the coupling between transition element and the light rare earth elements is ferromagnetic (case (a)) and anti-ferromagnetic in the case of heavy rare earth and transition element (case (b)) [Tre05].

the  $3d\downarrow$  is much greater than the corresponding overlap between  $5d\uparrow$  and the  $3d\uparrow$  orbitals, since the amount of hybridisation is proportional to the distance between the orbitals (Fig. 2.1). This causes the available  $d\downarrow$  states to be more in number than the available  $d\uparrow$  states resulting in an antiferromagnetic coupling between the  $3d$  and  $5d$  states. The antiferromagnetic  $3d$ - $5d$  coupling causes a strong antiparallel exchange coupling between the  $3d$  spins and  $4f$  spins. Hence, the magnetisations of the light rare earth ( $J = L - S$ , for light rare earths, as per the Hund's rule) and the transition metal are parallel, and the magnetisation of the heavy rare earth ( $J = L + S$ ) is antiparallel to the transition metal magnetisation leading to an anti-ferromagnetic  $R$ - $T$  coupling (Fig. 2.2). The strong ferromagnetic coupling in the light rare earth  $R$ - $T$  compounds makes them very attractive permanent magnets because the rare earth's moments can remain ordered to high temperatures (far above room temperature benefitting from the high  $T_C$  of transition metals) and the transition metal atoms, which have very low magnetic anisotropy, gain from the high intrinsic magnetic anisotropy of the rare-earths.

## 2.2 Magnetic Anisotropy

Anisotropy of a material means that the measured properties are different along different crystallographic directions. It is, hence, one key property which decides the shape of its magnetic hysteresis. Anisotropy in hard magnetic materials is essentially of two kinds:

### (a) Crystal Anisotropy

Also referred to as magneto-crystalline anisotropy, crystal anisotropy is the cause of intrinsic anisotropy in ferromagnetic materials. It may be viewed as a force that binds the magnetisation to a certain direction (or form of directions) in the crystal. For  $\text{SmCo}_5$  [Kir96], which has a hexagonal crystal symmetry, the magnetisation increases rapidly with the applied field along the  $c$ -axis and attains saturation very fast (Fig. 2.3). This axis, therefore, is called the easy axis since the magnetisation is easy to saturate. But when the field is applied along any other direction in the  $a$ - $b$  basal plane, the magnetisation increases at a constant rate (or in other words, the magnetic susceptibility  $\chi = \partial M / \partial H$  is low) until it saturates at the same value as for the easy axis. Since it is more difficult to saturate the magnetisation along this axis, it is called the hard axis direction. Both, the easy and the hard axis for  $\text{SmCo}_5$  are depicted in Fig. 2.3.

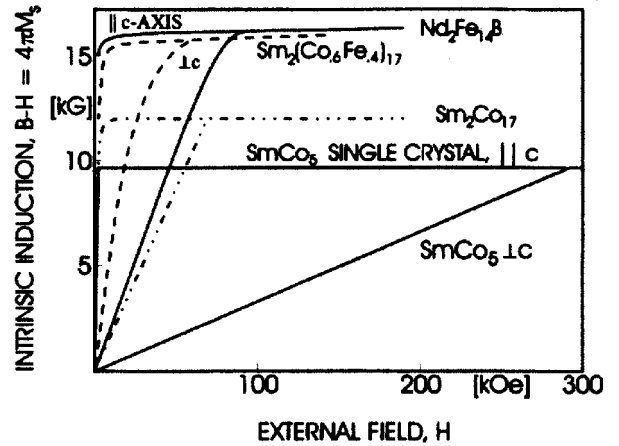


Fig. 2.3: Intrinsic anisotropy in  $\text{SmCo}_5$  [Kir96].

The increase in magnetisation occurs through domain wall motion or rotation, and the applied field must do work to turn the magnetisation vector away from the easy direction by a small angle  $\theta$ . This work gets stored as the crystal anisotropy energy  $E_K$  and for the specific case of hexagonal crystals with uniaxial anisotropy, it is given as [God65]:

$$E_K = K_0 + K_1 \sin^2 \theta + K_2 \sin^4 \theta + O(\theta^6) \quad (2.1)$$

where  $\theta$  is the angle between the easy axis and the applied field. Hence,  $E_K$  varies as orders of  $\sin^2 \theta$  and  $K_0$ ,  $K_1$ ,  $K_2$  are the zeroth, first, second order anisotropy constants which measure the weight of the successive  $\sin^2 \theta$  terms in the anisotropy energy equation.  $O(\sin^6 \theta)$  represents the higher order terms in  $\sin \theta$ . Generally,  $K_0$  is neglected because it is direction independent and  $K_1$ ,  $K_2$  and other higher order constants are considered if they have significant values.

For the case of Sm-Co,  $K_2$  is much smaller than  $K_1$  and hence  $K_2$  is neglected too. The anisotropy constants are strongly temperature dependent. The measured and calculated temperature dependence of  $K_1$  for  $\text{SmCo}_5$  [Szp79] [San75] is shown in Fig. 2.4. Since  $K_2$  is negligibly small, only the calculated temperature dependence of  $K_2$  is presented. Equation 2.1 presents a domain structure where in the demagnetised state the domains point either up or down.

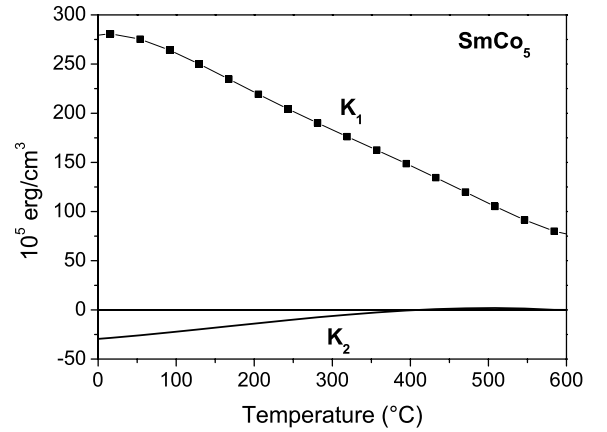


**Fig. 2.4:** Calculated and measured temperature dependence of  $K_1$  and  $K_2$  of  $\text{SmCo}_5$  [Szp79].

The anisotropy energy can also be expressed in terms of another concept, namely that of an anisotropy field  $H_K$ , which is the field that reproduces the energy necessary for small deviations from the easy axis. Hence, if a small deviation  $\delta\theta$  of the magnetisation  $M_S$  away from the easy axis changes  $E_K(\theta)$  correspondingly to  $\delta E_K(\theta)$ , then a restoring torque  $L(\theta)$  acts on  $M_S$  in the opposite direction, which tries to decrease  $\theta$ .

$$-L(\theta) \delta\theta = \delta E_K(\theta) \quad (2.2)$$

$$L(\theta) = -\frac{\partial E_K}{\partial \theta} \quad (2.3)$$

Equation 2.1 leads to

$$L(\theta) = -2K_1\theta \quad (2.4)$$

for small angular deviations  $\theta$ .

Alternatively, the torque exerted by the anisotropy field  $H_K$  on  $M_S$  is the work done by the anisotropy field in restoring the magnetisation again to its easy direction and, hence, is given by

the moment of the anisotropy field. Therefore,

$$L(\theta) = -\mu_0 H_K M_S \sin \theta \quad (2.5)$$

which for small angular deviations from the easy axis reduces to  $-\mu_0 H_K M_S \theta$ . And, hence,

$$\mu_0 H_K M_S \theta = 2K_1 \theta \quad (2.6)$$

$$H_K = \frac{2K_1}{\mu_0 M_S} \quad (2.7)$$

The anisotropy field at room temperature of the thin-film magnets under investigation in this work is 28 T, obtained by extrapolating the easy-axis curve and the hard-axis magnetisation curve to intersection. This compares very well with reports from Kirchmayr, Scholz and others [Kir96], [Szp79], [Sch03]. Whereas the anisotropy field takes account of restoration of small angle deviations of the magnetisation from the easy axis, the saturation field  $H_S$  is responsible for aligning all the spins along the applied field direction when the field points along a non-easy axis (or more appropriately, the hard axis). Thus,  $H_S$  is expressed as:

$$H_S = \frac{2K_1 + 4K_2}{\mu_0 M_S} \quad (2.8)$$

and is theoretically higher than  $H_K$ .

### (b) Shape Anisotropy

A second and equally important contribution to overall anisotropy in materials comes from the shape or geometry of the sample. Upon magnetising a sample in a strong externally applied field, positive and negative surface charges develop, forming magnetic dipoles in the sample. The direction of magnetic field generated by this dipole is opposite to the magnetisation of the sample. This field which intends to “demagnetise” the sample is called the demagnetising field and is given by

$$H_d = N_d M_S \quad (2.9)$$

where the coefficient  $N_d$  is the demagnetising factor. It is the second important field that determines the overall anisotropy in ferromagnets besides the intrinsic crystal anisotropy.

The demagnetising field is strongly influenced by the shape/geometry of the sample. For a polycrystalline sample, which has its grains oriented in all possible directions, there exists no overall crystal anisotropy. If it is additionally spherical, the magnetic moments average out and cancel one another. However, if the crystal is non-spherical, it is easier to magnetise it along the long axis as along the short axis due to a smaller demagnetising field along the long axis compared to the short axis. The energy that is associated with the demagnetising field of the sample (prolate ellipsoid) is

$$E_{SF} = \frac{1}{2} \mu_0 M_S^2 N_{\parallel} + \frac{1}{2} (N_{\perp} - N_{\parallel}) \mu_0 M_S^2 \sin^2 \theta \quad (2.10)$$

where  $\theta$  is the angle between the magnetisation vector and the long axis.  $N_{\parallel}$  and  $N_{\perp}$  are the demagnetisation factors along the long and the short axis of the ellipse, respectively. Hence,  $E_{\text{SF}}$  has the same form and angular dependence as the crystal anisotropy energy. Therefore, the shape anisotropy constant  $K_S$  [Kro85] can be deduced from Eq. (2.5) in analogy to the crystal anisotropy constant  $K_1$ :

$$K_S = \frac{1}{2}(N_{\perp} - N_{\parallel})\mu_0 M_S^2 \quad (2.11)$$

Back-calculating the *total anisotropy field*  $H_A$  with the shape anisotropy contribution in addition to the crystal anisotropy leads to:

$$H_A = \frac{2K_1}{\mu_0 M_S} - (N_{\parallel} - N_{\perp}) M_S \quad (2.12)$$

Although the two forms of anisotropies discussed above are the main contributors in most ferromagnetic materials, some others like exchange anisotropy or the magnetoelastic anisotropy may also exist. The magnetoelastic anisotropy has the same origin as the magneto-crystalline anisotropy (spin-orbit coupling) and arises from stresses or defects in the sample. However, in ideal defect free hard-magnetic ferromagnets, the magneto-crystalline anisotropy is very high and therefore, it makes the contribution of magnetoelastic anisotropy negligible.

## 2.3 Origin of Coercivity

Ferromagnets in an external magnetic field display the property of magnetic hysteresis. Hysteresis is the response of the magnetic material to an externally applied field to resist the demagnetisation process. This means that upon saturation (starting from a single domain state), when the applied field direction is reversed, the magnetisation lags behind the field and does not go to zero even when the external field is zero. Therefore, hysteresis simply comes from the remembrance of the magnetic history by ferromagnetic materials. The magnetisation that is left in the system upon field removal is the *remanent magnetisation*  $M_R$ . It is the maximum flux density that can be produced outside the permanent magnet near its surface.

The remanent magnetisation  $M_R$  is generally smaller than the saturation magnetisation  $M_S$ , which is the single domain magnetic moment. The ratio,  $M_R/M_S$ , is an important parameter for

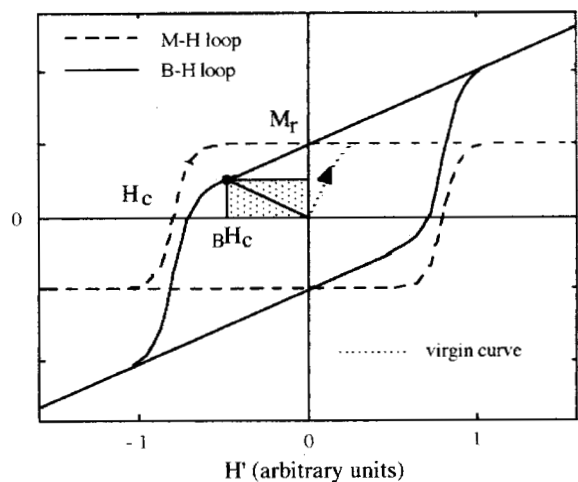


**Fig. 2.5:** Hysteresis in ferromagnets as B-H (solid) and M-H loop (dotted) showing the initial magnetisation loop (virgin loop), coercivity  $H_C$ , remanence  $M_r$  and the maximum energy product  $BH_{\text{max}}$  [Sko99].

permanent magnets and the closer this ratio comes to one, the better is the system for permanent magnet applications. A certain field equal to the *coercive field*  $H_C$  is needed to return the magnetisation to zero and the system again into a multi-domain state. The coercive field measures the broadness of the curve, which is directly related to the amount of hysteresis. A good permanent magnet has a coercivity  $H_C \geq M_R/2$  (Fig. 2.5). The hysteresis in ferromagnets can be expressed as  $B$ - $H$  loops (Hysteresis in magnetic induction  $B$  with field  $H$ ) or as  $M$ - $H$  loops (Hysteresis in magnetisation  $M$  with field  $H$ ).

Since

$$B = \mu_0 H + M \quad (2.13)$$

the two descriptions are qualitatively the same. The description above is valid for  $M$ - $H$  loops and the coercive field (where the magnetisation goes to zero) is not the same in the two descriptions. An obvious advantage of the  $B$ - $H$  loop is in the calculation of the maximum energy product  $(BH)_{\max}$ , which is a measure of the performance of the permanent magnet. It is the area of the largest square falling under the demagnetising branch in the  $B$ - $H$  curve. The quantity depends strongly on the coercivity, the remanence and the hysteresis loop squareness of the magnet and can have a maximum value  $(\mu_0 M_R)^2/4$ .

A magnet that has been saturated along the easy axis is now in its metastable energy minimum under the influence of a reverse magnetic field. The problem of understanding magnetisation reversal requires finding this local energy minimum and the energy barrier in the system, which is obtained by minimising the total energy of the system  $E_{\text{tot}}$ ,

$$E_{\text{tot}} = E_K + E_{\text{MS}} + E_{\text{EX}} + E_{\text{SF}} \quad (2.14)$$

$E_{\text{tot}}$  has contributions coming from :

$E_K$  : Crystal anisotropy energy

$E_{\text{MS}}$  : Magnetostatic energy

$E_{\text{EX}}$  : Exchange energy

$E_{\text{SF}}$  : Stray field energy

The solution of the above equation results in two local energy minima as shown by Kronmüller [Kro85]. On applying a reverse magnetic field of increasing magnitude, the relative potentials of the two minima change and one of them is favoured more than the other. The *nucleation field* is defined as the field at which the instability first sets in. It is necessary but may not be sufficient to overcome the energy barrier and, hence, cause magnetisation reversal.

In 1945, Brown [Bro45] calculated from purely energy considerations that the coercive field  $\mu_0 H_C$  must satisfy

$$H_C \geq \frac{2K_1}{\mu_0 M_S} - NM_S \quad (2.15)$$

which implies,

$$H_C \geq H_K + H_{SF} \quad (2.16)$$

and therefore, it is impossible to cause magnetisation reversal at fields  $H_C$  that are smaller than  $H_K$ . This inconsistency with reality is known as *Brown's Paradox*, since the experimentally measured coercivities can be up to an order of magnitude smaller than the anisotropy field.

An alternative method for magnetisation reversal is presented in the *Stoner-Wohlfarth model*, which considers homogeneously magnetised, single domain, magnetically uni-axial, non-interacting, ellipsoidal particles [Sto48]. The energy minimisation results in a nucleation field  $H_N$  (where  $\partial^2 E_{\text{tot}}/\partial\theta^2 = 0$ ), which is the same as the coercivity (where the energy minimum disappears),

$$H_C = \frac{2K_1}{\mu_0 M_S} - N_{\text{eff}} M_S \quad (2.17)$$

This is in accordance with the prediction of Brown's theory, which states that  $H_C$  is the lower bound of the anisotropy field. In reality, it is almost impossible to achieve even this lower bound of  $H_K$  and the observed coercivities are usually much smaller than the anisotropy field. Only in certain cases like the absolutely perfect iron whiskers as was shown by DeBlois and Bean [DeB59] and for the case of NdFeB films where the hard magnetic grains were richly diluted with Nd [Cre02] does the coercivity approach this theoretical lower bound. However, the difficulty in achieving these values is because Brown's micro-magnetic model and the Stoner-Wohlfarth solution are based on a homogenous, defect free, ideal system, which is difficult to realise. Furthermore, the effect of inhomogeneities that can cause magnetisation reversal at much lower fields as compared to the anisotropy field is not taken into account. These effects will be discussed in the next subsections.

### 2.3.1 Micro-magnetic Model

Of several approaches that exist in literature [Giv88b], [Giv88a] on considering real magnet structures, this work focusses on the micro-magnetic approach and tries to describe its usage appropriately to understand coercivity in real systems.

Coercivity in real magnets depends on the formation of a nucleus of reversed magnetisation at a defect site of very low or no anisotropy. This initial nucleation process requires an energy barrier equal to the nucleation field  $H_N$  to be overcome. The magnetisation reversal continues by propagation of domain walls from the defect into the hard phase of anisotropy constant  $K_1$ , requiring a propagation field  $H_{\text{pr}}$ , followed by expansion of the domain wall and finally the pinning and depinning of the domain wall at defect sites of strength  $H_{\text{pin}}$ . Each of these individual processes requires its own characteristic energy and field and the largest of these ultimately results in magnetisation reversal determining the coercive field.

The micro-magnetic model was developed by Aharoni [Aha60] and taken strongly further by Kronmüller [Kro87], [Kro88]. It assumes that the magnetisation reversal starts at a critical position

in the grain that is completely soft and has no anisotropy. Thus, the energy barrier is proportional to the magneto-crystalline energy of the hard-phase  $K_1$ . Nucleation is defined as the first reduction in magnetisation from saturation magnetisation value and the rest of the reversal occurs through coherent rotation of magnetisation as described by the Stoner-Wohlfarth theory by minimisation of the total magnetic energy. The solution of Eq. (2.14) in the case of  $K_2 = 0$ , gives the coercivity of the system similar to equation (2.17).

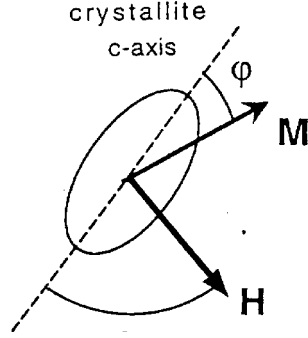


**Fig. 2.6:** Field and magnetisation directions in ellipsoidal grain [Coe96].

### (a) Effect of grain misorientation

When the external field is applied at an angle  $\theta_{cH}$ , towards the negative c-axis, and the magnetisation at  $\phi$  to the positive c-axis as illustrated in Fig. 2.6, the  $H_C(\theta_{cH})$  is:

$$H_C(\theta_{cH}) = \left( \frac{2K_1}{\mu_0 M_S} - N_{\text{eff}} M_S \right) \frac{1}{(\cos^{2/3} \theta + \sin^{2/3} \theta)^{3/2}} \quad (2.18a)$$

$$= \frac{2K_1}{\mu_0 M_S} \alpha_{\theta_{cH}} - N'_{\text{eff}} M_S \quad (2.18b)$$

$$\text{where } \alpha_{\theta_{cH}} = \frac{1}{(\cos^{2/3} \theta_{cH} + \sin^{2/3} \theta_{cH})^{3/2}} \quad \text{and } N'_{\text{eff}} = \alpha_{\theta_{cH}} N_{\text{eff}}.$$

This angular dependence dictates the coercivity to vary from  $H_A$  to  $H_A/2$  as  $\theta_{cH}$  varies from 0 to  $\pi/4$  and then increases again to  $H_A$  at a  $\theta_{cH}$  of  $\pi/2$ , resulting in a positive parabolic variation of  $H_C$  over  $\theta_{cH}$  as shown in Fig. 2.7. A strong decrease in coercivity of the system as compared to the anisotropy field is observed as the angle between the applied field and the c-axis is increased. If the easy magnetisation direction is along the c-axis (such that  $\phi = 0$ ), and also, the externally applied field is along the negative c-axis (such that  $\theta_{cH} = 0$ ) but the magnet is composed of an assembly of misoriented grains where the misorientation angle of a single grain is  $\phi$ , then Eq. (2.15) gets modified to

$$H_C(\phi) = \frac{2K_1}{\mu_0 M_S} \alpha_{\phi}^{\text{ass}} - N'_{\text{eff}}^{\text{ass}} M_S \quad (2.19)$$

where  $\alpha_{\phi}^{\text{ass}}$  is the parameter that takes care of grain misorientation of the entire grain assembly of

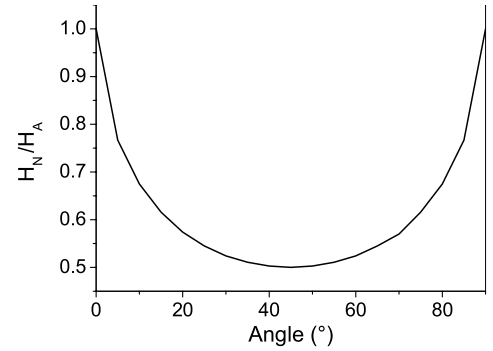


**Fig. 2.7:** Stoner-Wohlfarth angular dependence for ellipsoidal, single domain particles reversing their magnetisation by uniform coherent rotation.

the sample and depends on the individual grain misorientation angles  $\phi$  as

$$\alpha_{\phi}^{\text{ass}} = \int \alpha_{\phi}^{\text{grain}} f(\phi) d(\phi) \quad (2.20)$$

$$\alpha_{\phi}^{\text{grain}} = \frac{1}{(\cos^{2/3} \phi + \sin^{2/3} \phi)^{3/2}} \quad (2.21)$$

$$N'_{\text{eff}} = \alpha_{\phi}^{\text{grain}} N_{\text{eff}} \quad (2.22)$$

and  $f(\phi)$  is the distribution function of misorientation angle  $\phi$  of the entire sample assembly.

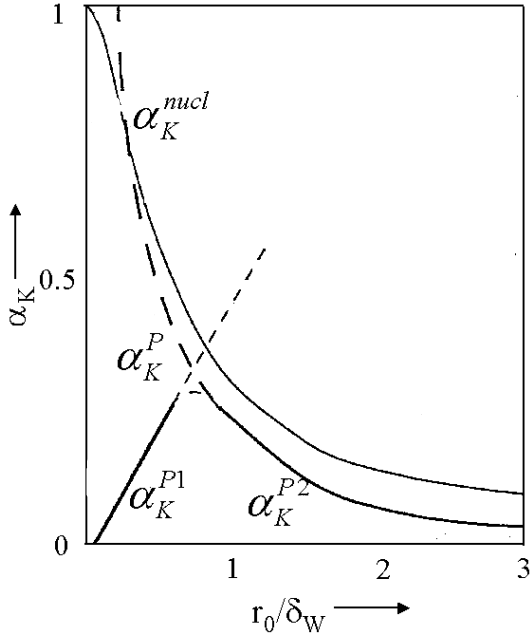


**Fig. 2.8:** Dependence of  $\alpha$  on the normalised defect size [Kro88].

$$H_C = \frac{2K_1}{\mu_0 M_S} \alpha_K - N'_{\text{eff}} M_S \quad (2.24)$$

Here, the first term describes the nucleation field and  $\alpha_K$  and  $N'_{\text{eff}}$  are parameters that incorporate the effect of planar inhomogeneity and again determine the relative importance of the anisotropy field and the demagnetising field. Along with  $\alpha_{\phi}^{\text{ass}}$ , which takes care of grain misalignment of the entire sample ensemble, Eq. (2.24) gets modified to

$$H_C = \frac{2K_1}{\mu_0 M_S} \alpha_K \alpha_{\phi}^{\text{ass}} - N'_{\text{eff}} M_S \quad (2.25)$$

where  $\alpha_K$  is a microstructural parameter and is given by

$$\alpha_K(r_0) = 1 - \frac{1}{4\pi^2} \frac{\delta_W^2}{r_0^2} \left[ 1 - \sqrt{1 + \frac{4\pi^2 r_0^2}{\delta_B^2}} \right]^2 \quad (2.26)$$

### (b) Effect of inhomogeneities

To consider the effect of inhomogeneities on the magnetisation reversal process, Kronmüller and co-workers [Kro87] investigated the effect of a planar defect within which the anisotropy follows a spatial variation of the form

$$K_1(z) = K_1(\infty) - \frac{\Delta K_1}{\cosh^2(z/r_0)} \quad (2.23)$$

and has a halfwidth  $r_0$ .  $K_1(\infty)$  is the anisotropy constant in the hard phase and  $\Delta K_1$  is the reduction of anisotropy in the defect. Inserting this anisotropy variation in Eq. 2.12 and minimising the total energy leads to

with the domain wall width  $\delta_W = \pi \sqrt{A_{\text{ex}}/\Delta K_1}$ .

As seen from Eq. (2.25),  $H_C$  has a direct dependence on  $\alpha_K$ , which in turn has a characteristic dependence on the width of the planar defect normalised to the domain wall width, *i.e.*  $r_0/\delta_W$ . This indirect dependence of  $H_C$  on the normalised defect size is shown in Fig. 2.8 through the plot of  $\alpha_K$  versus  $r_0/\delta_W$ . The variation of  $\alpha_K$  with  $r_0/\delta_W$  also establishes the link between the magnetisation reversal mechanisms of nucleation or pinning with the defect size. The absolute value of  $\alpha_K$  decreases with the normalised defect size for the nucleation type magnets since the larger the low-anisotropy defect, the more easily the magnetisation in the whole grain would switch.

However for the case of pinning, there exists a critical defect size, correlated to the domain wall width where the pinning is most effective, resulting in a maximum in  $\alpha_K$  for the defect size  $2r_0 \sim \delta_W$  (domain wall width). On either side of this maximum, a decrease in pinning efficiency is observed. Defects with sizes that are much smaller than the critical domain width ( $r_0 \ll \delta_W$ ) are incapable of impeding domain wall motion and hence cause ineffective pinning. On the other hand, defects much larger than the domain wall width do not offer a strong hindrance to wall propagation either, as these are not viewed as defects anymore, and rather may be considered equivalent to domain wall propagating through a second phase.

### 2.3.2 Confirmation of Pinning

#### (a) Low $\alpha_K$

Pinning of domain walls in magnetic systems can be visualised as a membrane fixed (*pinned*) at several points on its surface by various defects (*pins*). Pinning sites are characterised as strong or weak depending on the amount of restoring force  $f$  they are able to exert on the domain wall to hinder its movement. The propagation field  $H_{\text{pr}}$  is given as [Coe96]:

$$H_{\text{pr}} = f / 2\mu_0 M_S S \quad (2.27)$$

where  $S$  is the area of the domain wall on which the pinning force  $f$  of a single pin is effective. Intuitively, a smaller  $S$  would provide more effective pinning and, hence, larger  $H_{\text{pr}}$ . And hence, a very large number of pins/defects are desired for effective pinning. Alternatively, for practical reasons it is better to have planar defects than a large density of point defects to achieve the same pinning forces.

If the pins are planar defects, for very small defects with  $2r_0 < \delta_W$  (see Fig. 2.8)

$$H_{\text{pr}} = H_A \frac{\pi}{3\sqrt{3}} \frac{r_0}{\delta_W} \quad (2.28)$$

which clearly says that the propagation field increases with the increase in defect size of the small defects. For the case of extended defects,  $r_0 > \delta_W$ ,

$$H_{\text{pr}} = H_A \frac{2\delta_W}{3\pi r_0} \quad (2.29)$$

Hence,  $H_{pr}$  decreases as the width of the planar defect increases. Both the relations are plotted in Fig. 2.8 in the pinning regime of magnetisation reversal. When  $2r_0 \simeq \delta$ , a maximum is obtained in the propagation field where  $H_{pr} \simeq 0.3 H_A$ , confirming that the maximum  $\alpha_K$  for a pinning magnet can be as high as 0.3–0.35.

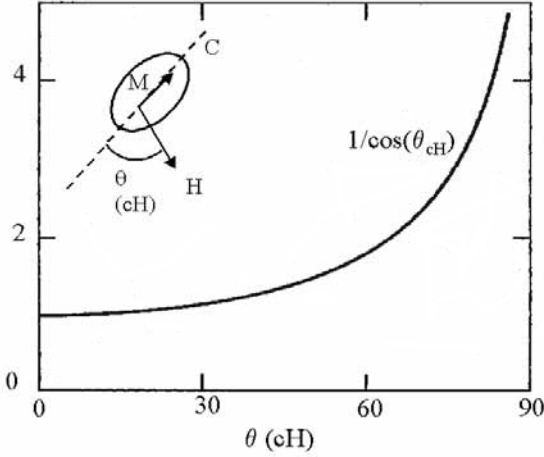


**Fig. 2.9:**  $1/\cos \theta$  variation of normalised coercivity due to non-uniform reversal processes. [Coe96]

### b) Angular Dependent Measurements

As a follow up from the section before, magnetisation reversal by pinning of domain walls at grain boundaries or other defect sites can cause this huge decrease in  $H_C$  compared to  $H_A$ . Additional processes that involve incoherent or non-uniform reversal processes like curling, buckling etc. [Sht57], [Aha58], [Aha60] are also capable of reducing coercivity drastically. In this case, the Stoner-Wohlfarth type coherent rotation is not the dominant reversal mechanism.

If a prolate grain is placed in a reverse external field applied at  $\theta_{cH}$  (inset of Fig. 2.9), the effect of the external field can be considered in terms of the vertical component of  $H_{app}$ ,  $H_V = H_{app} \sin \theta$  and its horizontal component  $H_H = H_{app} \cos \theta$ . The component  $H_V$  causes uniform Stoner-Wohlfarth rotation of the magnetisation but since  $H_C \ll H_A$ , the rotation of moments is very small and negligible and the only angular dependence results from the horizontal component  $H_H$ , causing reversal at  $H_H = H_{app} \cos \theta_{cH}$  [Kon40]. In this case, the reversal field follows a  $1/\cos \phi$  dependence as is seen in Fig. 2.9.

### (c) Low Initial Susceptibility in Hysteresis

Additionally, information on the magnetisation reversal mechanism of the sample is also obtained from the initial magnetisation curve, which is measured starting from the thermally demagnetised state. The two cases of nucleation and pinning may be distinguished based on the values of the initial susceptibility,  $\chi_{ini}$ :

$$\chi_{ini} = \left( \frac{\partial M}{\partial B} \right)_{B \rightarrow 0} \quad (2.30)$$

In the initial thermally demagnetised state, there are two sorts of domains in which the magnetisation points parallel and antiparallel to the easy axis. For the case of nucleation dominated magnets, an external field applied parallel to one sort of domains favours the growth of these domain (domains with magnetisation parallel to the external field) and the domain wall sweeps across the entire sample without any further hindrance. This causes the initial magnetisation to increase

rapidly even at small applied fields and the measured  $\chi_{ini}$  in this case is, therefore, very high.

On the other hand for pinning dominated magnets, an external magnetic field applied parallel to the magnetisation in one type of domain can still not increase the magnetisation of the entire sample rapidly due to the presence of pinning defects in the system. These defects require their own characteristic energy thresholds and block the domain wall from expanding or the magnetisation of the whole system to increase, until sufficient energy is supplied to overcome these pinning barriers. This situation results in an initial susceptibility  $\chi_{ini}$  which remains low up to large applied fields and only at higher applied fields when the pinning forces are overcome does the magnetisation increase. External fields larger than depinning fields of strong defects are necessary to overcome the pinning barrier and increase the magnetisation of the entire grain ensemble. The measurement of the initial magnetisation curve may therefore yield first-hand information on the nature of the reversal mechanism.

## 2.4 Intergranular Exchange Coupling

A very important property for ferromagnetic materials as seen and discussed in the section before is to have a high remanence. High remanences along with high coercivities are the key to high energy products. However, if the sample is completely isotropic and non-interacting, the achievable remanence is restricted to half of the saturation magnetisation (for uniaxially anisotropic materials), which is an intrinsic limitation of the material (i.e.  $J_R \leq J_S/2$ ) [Sto48].

This limit on the maximum achievable remanence in the system can be overcome if the grains are *exchange coupled* [Mei56]. The phenomenon of exchange coupling is active across the interfacial region of neighbouring crystallites where the moments in different grains try to align themselves parallel and deviate from the easy-axis direction of the individual crystallites as is shown in Fig. 2.10. A strong exchange coupling in magnetic systems is not only visible in the remanent magnetisation but it may affect the shape of the entire hysteresis loop. The more strongly bound the magnetic grains in a system are, the more coherent and spontaneous would be the magnetisation switching of the entire sample after saturation and the whole sample reverses its magnetisation at the same applied field value. Hence, the hysteresis of an exchange coupled system is more square-shaped, increasing its RSQ. As the grains become smaller, the interfacial area where the interaction is active becomes larger. This increases the amount of exchange coupling and thereby enhances its contribution to the overall magnetisation.

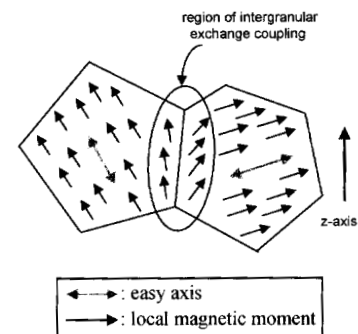


**Fig. 2.10:** Deflection of magnetisation axis from the local easy axis [Neu98], [Bol03].

Besides the grain sizes, the crystallographic texture of the sample also affects exchange coupling and, hence, the better the texture, the greater is the extent of intergranular exchange coupling. A well aligned c-axis in a uniaxially anisotropic material predicts domains parallel and anti-parallel to the c-axis. The presence of an additional exchange coupling in this system results in large domains which span several of the crystallographic well-aligned sample grains forming *interaction domains* (and the grain size is much smaller than the domain size). Or, vice-versa, the presence of large interaction domains signals the presence of exchange coupling in the system. The amount of exchange coupling in magnetic systems becomes also evident in the recoil loops which will be described in the next subsections.

### 2.4.1 Recoil Loops

For a system of non-interacting, single domain particles with uniaxial anisotropy, the remanence relation

$$J_R^D(H_m) = J_R - J_R^m(H_m) \quad (2.31)$$

must hold for all kinds of easy axis distributions [Woh58]. Here,  $J_R^D(H_m)$  represents the polarisation in the demagnetising branch after applying a reverse field  $H_m$  to the saturated sample.  $J_R$  is the remanence of the sample after  $H = \infty$  and  $J_R^m$  is the remanence of the sample after applying a field  $H_m$  starting from the thermally demagnetised state. Subsequent repetition of this process, of applying and removal of the external field of increasing magnitude in the magnetising branch and in the demagnetising branch, produces *recoil loops*.

### 2.4.2 Inter-grain Interactions – $\delta J$ Plot/Henkel Plot

A direct evidence for an exchange coupled system or in other words the denial of a Stoner-Wohlfarth system of non-interacting particles can be seen in the plot of  $J_R^D(H_m)/J_R$  vs.  $J_R^m(H_m)/J_R$ . This plot must be a straight line (Fig. 2.11) for single domain particles with uni-axial anisotropy which are non-interacting. Any deviation from the conditions listed above results in a non-linear fit and hints coupling in the system. This plot is the so-called *Henkel-plot* [Hen64] and is shown in Fig. 2.11 for an ideal system and systems that deviate from the ideal conditions.

The difference,  $\delta J = [J_R^D(H_m) - \{J_R - J_R^m(H_m)\}] / J_R$  is a more intuitive representation for verifying the presence of coupling in the system.  $\delta J$  measures the difference between remanent magnetisations of the sample in the magnetising (from thermally demagnetised level) and demagnetising branches (after saturation). In other words, it is a measure of the ease of magnetisation for the two branches of the hysteresis loop and in an ideal situation, the processes of magnetisation and demagnetisation must be similar thereby resulting in a  $\delta J$  which is zero for all applied fields. Any process that favours one of the two processes (magnetisation or demagnetisation), i.e. makes one of the two processes easier, would result in a deflection of  $\delta J$  from zero and indicate a *coupling* in

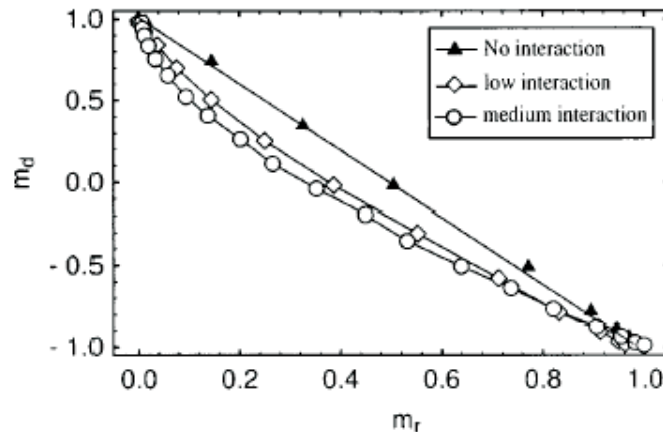


**Fig. 2.11:** Henkel Plot for non-interacting and interacting system [Gar00].

the system.

Commonly called the  $\delta J$  or the  $\delta M$  plots are the plots of measured  $\delta J$  with the magnetic field  $H_m$ . For non-zero  $\delta J$  depending on the sign of  $\delta J$ , two kinds of interactions are distinguished – exchange interactions and magnetostatic interactions. While exchange interactions are intense and short range interactions responsible for aligning the magnetic spins parallel to one another, the magnetostatic interactions are much weaker and extend over larger dimensions. They are mediated from stray fields between neighbouring spins and compete with exchange interactions. Stray field minimisation requires the magnetisation in nearest domains to be anti-parallel and, hence, completely opposes the exchange energy requirements for parallel alignment of spins. A positive deflection in  $\delta J$  would mean that the process of demagnetisation is more difficult than magnetisation. This is because exchange interactions force the neighbouring spins in the remanent state to remain parallel and it dominates over magnetostatic coupling. On the other hand, if magnetisation of the sample is more difficult than demagnetisation (negative  $\delta J$ ), it would indicate that the sample has a tendency to remain in a multi-domain state, where the stray field energy is minimised. Therefore, in this case magnetostatic coupling dominates over exchange coupling which tries to align the neighbouring spins parallel. Hence, all positive deviations of  $\delta J$  are attributed to an exchange coupled system and negative deviations from  $\delta J = 0$  would refer to magnetostatic interactions [Bea91], [Min91] and [Zha03].

## 2.5 The Sm-Co System – An Introduction

The quest for better and better magnetic materials and phases has continued for decades. Discovered in 1967 by Strnat *et al.* [Str67], Sm-Co bulk magnets showed tremendous potential promising high  $(BH)_{\max}$  values compared to the ferrites and AlNiCos where the energy density was restricted to  $40 \text{ kJ/m}^3$ . As already mentioned, the combination of Rare-earth (R) and Transition metal (T) is

a novel combination in the sense that  $T$  benefits from the high magneto-crystalline anisotropy of the  $R$  and the rare-earth element can preserve its magnetic moment and the anisotropy up to high temperatures.

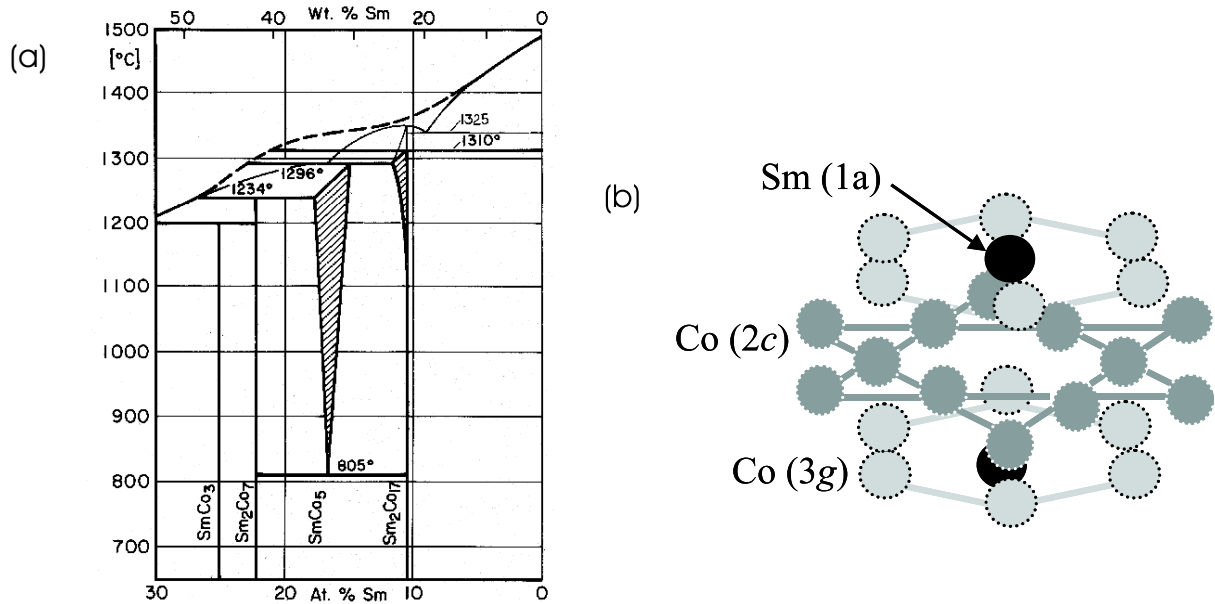


**Fig. 2.12:** (a)  $\text{Sm-Co}$  phase diagram showing predominance of  $\text{SmCo}_5$  and  $\text{Sm}_2\text{Co}_{17}$  among the four phases shown as per [Bus98] (b)  $\text{SmCo}_5$  unit cell.

The phase diagram of  $\text{Sm-Co}$  is shown in Fig. 2.12. Out of seven major and several other minority phases existing for  $\text{Sm-Co}$ , four phases are seen in this restricted  $\text{Sm-Co}$  phase diagram which exist close to the composition range investigated in this work. The phase diagram starts at the very rare-earth poor  $\text{Sm}_2\text{Co}_{17}$  phase corresponding to 12 at.% Sm and continues to phases with very high Sm content as in  $\text{SmCo}_3$  (25 at.% Sm). All of the phases of  $\text{Sm-Co}$  possess hard magnetic properties with  $T_C \gg 300$  K (room temperature) and for some of these relevant phases, the intrinsic properties are listed in Tab. 2.1. Both the  $\text{Sm}_2\text{Co}_{17}$  and the  $\text{SmCo}_5$  phases are stable over broader composition ranges and larger temperature spans and, hence, occupy the largest areas in the phase diagram. Both the phases have hexagonal crystal symmetry, a high saturation polarisation of more than 1 T, very high Curie temperatures and positive values for the first anisotropy constant  $K_1$  but the  $\text{Sm}_2\text{Co}_{17}$  phase has a lower anisotropy field compared to the  $\text{SmCo}_5$  making it less attractive for permanent-magnet applications.

$\text{SmCo}_5$  has a hexagonal  $\text{CaCu}_5$  type structure, belonging to the  $P6/mmm$  space group. It has 6 atoms per unit cell. The atomic arrangement resembles a layer-by-layer stacking along the  $c$ -axis of a layer of Co atoms and the next containing both Sm and Co atoms. In the Sm and Co *sub-layer*, the two sub-structures are rotated by  $30^\circ$  with respect to each other. The Sm atoms occupy one 1a crystallographic site and the Co atoms fall on two kinds of sites, the 2c with twofold multiplicity

**Table 2.1:** *Intrinsic magnetic properties for some of the Sm-Co phases.*

Phase	Sm (at.%)	$T_C(^{\circ}\text{C})$	$\mu_0 H_A(\text{T})$	$J_S(\text{T})$
2:7	22.2	420	20	0.79
1:5	16.7	720	30	1.14
1:7	12.5	800	10–20	1.2
2:17	10.5	900	7	1.25

and the 3g sites with threefold multiplicity [Zha00], [Str79]. The anisotropy in  $\text{SmCo}_5$  is supposed to originate from the large orbital moment of the Co atoms and their anisotropic coupling with the Sm atoms through spin-orbit coupling. The 3d orbitals of Co at 2c sites have a large magnetisation density which is essentially extended in the basal plane of the unit cell, perpendicular to the c-axis. Hence, these atoms make a larger contribution to the spin-orbit coupling with the Sm atoms, yielding a positive contribution to the crystal anisotropy. However, the magnetic moments of the Co atoms at 3g sites have no preferred direction. They contribute only negligibly to the 3d-4f coupling and give a small negative contribution to the overall crystal anisotropy. Among several phases of Sm-Co compounds possible, the  $\text{SmCo}_5$  phase has, for comparable saturation magnetisations of these phases (with the exception of  $\text{Sm}_2\text{Co}_7$  which even has a smaller  $M_S$ ), the highest anisotropy field [Str67], [Bar76], [Der79], [Erm76], [Str72], [Tat70], which makes it extremely attractive for its use as permanent magnet.  $\text{SmCo}_5$  exhibits uniaxial anisotropy where the c-axis is the axis of easy magnetisation.

The  $\text{Sm}_2\text{Co}_7$  is another interesting phase from the Sm-Co system. It corresponds to 22 at.% Sm and has a  $J_S = 0.84$  T. It has hexagonal crystal symmetry like  $\text{SmCo}_5$ , but is slightly more complicated with 36 atoms per unit cell (8 Sm atoms + 28 Co atoms). The lattice constant in the basal plane, a, of  $\text{SmCo}_5$  and  $\text{Sm}_2\text{Co}_7$  are very similar and comparable whereas the lattice constant normal to the basal plane, c, is six times larger in the case of  $\text{Sm}_2\text{Co}_7$  than in the  $\text{SmCo}_5$  phase (Fig. 2.13a). The long c-axis is again the axis of easy magnetisation like for  $\text{SmCo}_5$ , which means that the magnetisation attains its full saturation value at low fields along this axis and it is difficult to magnetise it along any other direction in the basal plane. These properties are clearly seen in the hysteresis loop in section (2.2). Due to their similarity in crystal structure, identification and precise determination of their reflections is necessary. A methodology to distinguish as accurately as possible between the two phases requires finding non-equivalent reflections from the two phases and compare them to the reflections in the sample. The XRD Pdf (powder diffraction) data for the two phases are presented in Fig. 2.13b. One finds that the reflections (112), (113), (222) in the  $\text{SmCo}_5$  phase have no parallel reflections from the  $\text{Sm}_2\text{Co}_7$  phase, however, due to the weak

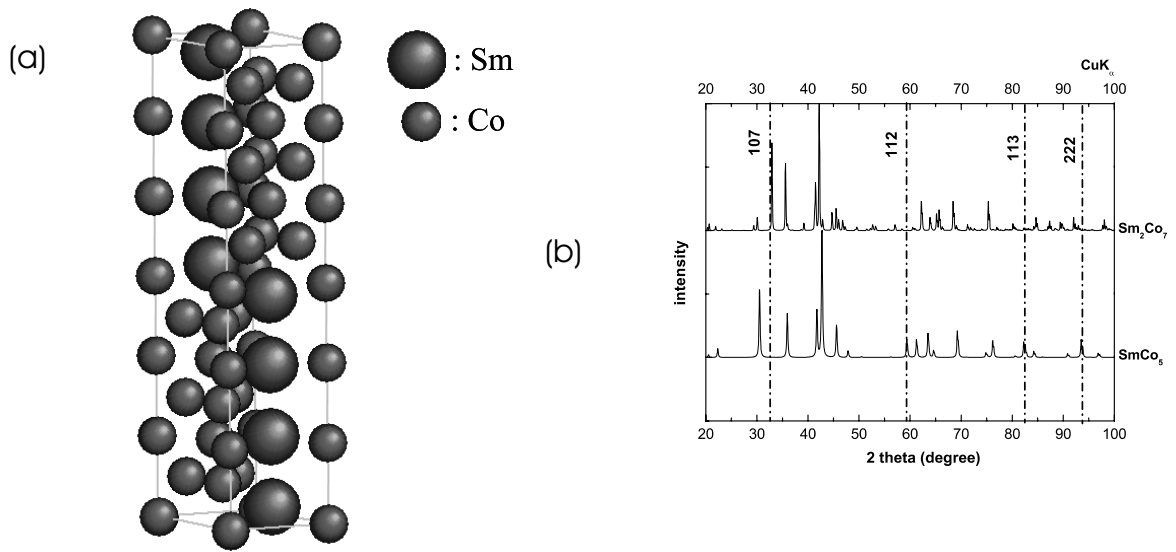


**Fig. 2.13:** (a)  $\text{Sm}_2\text{Co}_7$  unit cell. (b) Powder diffraction data for  $\text{SmCo}_5$  and  $\text{Sm}_2\text{Co}_7$ .

intensity of all these peaks, identifying them in the sample would also pose a serious problem. On the other hand, there exists the (107) peak in the  $\text{Sm}_2\text{Co}_7$  phase which has no equivalent counterpart in the  $\text{SmCo}_5$  phase. Additionally, this peak possesses 50% intensity of the maximum measured intensity displayed by the (111) reflection. Hence, this peak can be used as a marker for distinction between the two phases.

Sm-Co compounds are potential candidates for permanent-magnet applications due to their very attractive hard magnetic properties [Bud02]. Work on Sm-Co magnets has varied from optimising grain sizes to increasing energy products by means of remanence enhancement or exchange coupling [Pra99] where, starting from meagre values of  $(BH)_{\max} \sim 40 \text{ kJ/m}^3$  [5MGOe] [Str67] for the pure  $\text{SmCo}_5$ , energy products of the order of  $254 \text{ kJ/m}^3$  [32 MGOe] [Zha05] have been obtained to-date. Research has continued on attempts to understand the fundamental mechanisms of coupling in the 3d-4f shells [Cad87b], [Ric98], [Rad02], the limitations on coercivity, probing intergranular exchange [Pow02], developing high performance magnets [Kum86], [Kub99] along with textured thin films [Ful97], [Neu99] and nanostructured devices [Sko03], [Zho05]. Furthermore, Sm-Co continues to be an attractive source of magnetism to magnetism researchers [Tro90], [Kum88], [Giv03], still holding intrinsic anisotropy values that might be record breaking.

## 2.6 Review: Magnetisation Reversal – Rotational or Non-Rotational Processes?

The performance of magnets suitable for application requires a deeper understanding of the processes that determine the magnetic properties. High coercivities can be achieved only if the underlying mechanism that determines the coercivities in these systems is known and well exploited. Brown's micro-magnetic approach is to-date the most widely used theory for determining magnetisation reversal [Bro45]. The approach is extremely general and is made practical for reversal in real systems by Stoner and Wohlfarth [Sto48] for particles reversing their magnetisation by uniform rotational processes and by Kondorsky [Kon40] for particles where no uniform rotation is possible due to  $H_C \ll H_A$ . These two approaches differ essentially in the angular variation of  $H_N$  in the magnetisation processes. To best describe the reversal phenomenon, one requires further experiments to distinguish between non-rotational processes (that can also cause  $H_C \ll H_A$  for curling, buckling etc.

citeAha1960, [Aha58], [Sht57]) or pinning mechanisms. This may be achieved by a temperature dependent  $H_C$  analysis and interpreting  $\alpha$  as was described in section 2.3.1 or by direct observation of domain nucleation and pinning by state-of-art microscopy techniques. Both of these approaches are available in literature to describe the magnetisation reversal, the former more than the latter. This section is devoted to a collection of consistent work that is available in literature to understand magnetisation reversal. Givord *et al.* have presented a thorough summary on the general theory of nucleation and pinning type magnets [Giv91].

In 1972 [Bec72] while studying single particle magnetisation reversal in  $\text{GdCo}_5$ , Becker demonstrated the inverse  $\cos \theta$  dependence of  $H_N$ . He ascribed it to reversal occurring through "nucleation" of  $180^\circ$  domain walls and the negligibility of rotational processes, which is justifiable for  $H_N \sim 1\% H_A$ . In angular dependent experiments on  $H_C$  of single-crystal  $\text{SmCo}_5$ , Menth and co-workers [Men74] found an excellent fit between the measured  $1/\cos \theta$  dependence of  $H_C$  as predicted by Kondorsky [Kon40]. The experiments on  $\text{SmCo}_5$  samples prepared by powder metallurgy, however, show a much poorer fit with theory. Pastushenkov *et al.* showed with detailed measurements on magnetisation reversal of a group of sintered grains [Pas95], that all critical fields ( $H_S$ ,  $H_K$ ,  $H_N$ ) follow an inverse  $\cos \theta$  dependence, where  $\theta$  is the angle between the external field and the sample texture axis. Using Kerrmicroscopy, they further demonstrated that the deviation from this behaviour is largest for  $H_N$  and concluded that the individual nucleation fields of particles are strongly a function of the distance between these particles and their local environments [Pas96].

Kronmüller and co-workers made a strong contribution to Brown's micro-magnetic theory by introducing the microstructural parameter,  $\alpha_K$ , and the grain misorientation parameter  $\alpha_\phi$  [Kro87].

The experimental angular dependence of  $\alpha_\phi$  enabled authentic distinction between the nucleation and the pinning mechanism. For sintered Nd-Fe-B magnets,  $\alpha_\phi$  values lay between the theoretical predictions for nucleation and pinning models. However, it could well be explained with a nucleation model by merely introducing a grain misorientation of  $20^\circ$ . Both nucleation and pinning have been observed in the same magnet, at different temperatures [Tel97].

Furthermore, Kronmüller and co-workers demonstrated that  $\alpha_K$  has a characteristic dependence on the defect size [Kro88], and that the absolute value of  $\alpha_K$  is also a deciding factor between nucleation and pinning, provided  $H_C$  decreases monotonically with increasing temperature. This case, however, as could be seen from Fig. 2.8, is slightly biased towards nucleation type magnets, because a high  $\alpha_K$  ( $> 0.3$ ) suggests nucleation in the system unambiguously, a lower  $\alpha_K$  on the other hand, rules out neither pinning nor nucleation in the system. Hence, the only shortcoming of the model lies in assigning low values of  $\alpha_K$  to pinning.

Tellez-Blanco and co-workers studied the behaviour of Fe, Cu, Zr doped  $\text{Sm}_2\text{Co}_{17}$  sintered magnets [Tel97] and reported that for both anisotropic and isotropic magnets the temperature dependent micro-magnetic model results in nucleation controlled reversal at high temperatures ( $> 460\text{--}520^\circ\text{C}$ ), which changes to a pinning type behaviour (characterised by a low value of  $\alpha_K$ ) in the low temperature regime. The temperature dependence of  $H_C$  was systematically studied by Tang *et al.* [Tan01] in Cu-doped bulk  $\text{Sm}_2\text{Co}_{17}$  samples. They observed an unusual behaviour in  $H_C(T)$  where for samples with low Cu content,  $H_C$  decreased with temperature up to a critical temperature, showed an upturn and then continued the usual monotonic decrease with increasing temperature again. This anomalous behaviour is said to arise from a weak repulsive pinning of the domain walls by the  $\text{SmCo}_5$  phase at low Cu contents, which changes to the normal monotonic decrease of  $H_C$  with temperature at higher Cu contents due to an attractive pinning of the domain walls in the  $\text{Sm}_2\text{Co}_{17}$  phase by the  $\text{SmCo}_5$  phase. Further work on bulk Sm-Co magnets has been reported by Chen *et al.* [Che97]. A nano-composite  $\text{Sm}_2\text{Co}_{17}$  magnet with excess Co was investigated to consider the role of Co particles as possible pinning sites. Domain wall pinning from thick inhomogeneities (defects other than excess Co) was concluded to be the determining coercivity mechanism from micro-magnetic analysis. Similar work on doped bulk  $\text{Sm}_2\text{Co}_{17}$  sintered magnets is also reported by Gutfleisch *et al.* [Gut04], [Yan05].

Analyses of coercivity mechanisms have not been performed as much for Sm-Co thin-film magnets as it has been applied to Sm-Co bulk magnets even though the quality work done on preparation of Sm-Co thin-film magnets has been very comparable to bulk Sm-Co magnets. Reports exist from Pina *et al.* [Pin04] on the applications of micro-magnetic model to thin Sm-Co films of 20 at.% Sm content. The model was applied to the Cr/Sm-Co/Cr/Si system. The films show isotropic behaviour for room-temperature prepared samples and a weakly anisotropic in-plane hysteresis in samples prepared at high temperatures. Low values of  $\alpha$  ( $< 0.1$ ) had been observed in all

directions, which are interpreted as an indication of poor crystallinity in these films (This is, however, not remotely hypothesised by the micro-magnetic model!). Moreover,  $N_{\text{eff}}$  values  $> 1.5$  are supposed to indicate columnar growth in these samples. Similar works strongly motivate several other researchers to continue improved investigations in the direction of coercivity mechanisms of Sm-Co thin films.

Interestingly, magnetic coupling between grains, which affects the overall reversal process, is also accounted for in Kronmüller's micro-magnetic model. After incorporating intergranular exchange in the case of Pr-Fe-B magnets, an almost perfect fit in the temperature-dependent coercivity analysis was observed. An  $\alpha_K \sim 0.92$  shows a dominant nucleation mode undoubtedly [Kou94].

## 2.7 Review: Remanence Measurements

Remanence measurements can be used to probe intergranular coupling between the magnetic grains. The Stoner-Wohlfarth theory for the case of non-interacting, single domain, ellipsoidal particles asserts that the dc magnetisation and equivalent ac remanence state (starting from the ac-erased state) must be equally stable. In other words,

$$J_{\text{R}}^{\text{D}}(H_{\text{m}}) = J_{\text{R}} - J_{\text{R}}^{\text{m}}(H_{\text{m}}) \quad (2.32)$$

must hold for non-interacting particles, and any deviation from this relation must come from some magnetic interactions between the particles of the system [Sto48]. In 1991, Beardsley and Zhu calculated  $\delta M$  as a measure of deviation from the above equation from pure simulations on an array of  $60 \times 60$  hexagonal grains with in-plane anisotropy [Bea91]. The sign of  $\delta M$  changes from a valley in the negative region (for the case of pure magnetostatic interactions) to a peak in the positive one with addition of a small amount of exchange interaction to the system. With increasing amount of exchange, the magnitude of the peak increases and the peak position shifts to lower applied-field values. Finally, a positive  $\delta M$  results from out-of-plane anisotropy and a negative  $\delta M$  is the result of pure in-plane anisotropy in a system without exchange coupling [Bea91].

The amount of magnetic exchange between hard magnetic Sm-Co/Cr grains was observed by Romero *et al.* for different Cr buffer thicknesses and textures [Rom00]. It has been reported that the Sm-Co grains are exchange coupled at all thicknesses of Cr buffer. However, the extent of exchange is a strong function of the buffer texture. The irreversible magnetisation  $M_{\text{irr}}$  more than doubles for buffers prepared at high temperatures compared to films on room temperature buffers. This increase is agreeable from the improved quality of Sm-Co reported on these high temperature buffers [Rom00]. Huge enhancements in coercivities (of more than two orders of magnitude) have

been seen in exchange-coupled  $\text{SmCo}_5$  films after Cu and Ni additions. Although the nature and amount of exchange coupling remains unchanged by these additives [Pra99], they are thought to be responsible for the enhancement in pinning, characteristic of the magnet.

The purpose of positive exchange coupling is best served if an enhancement in the magnetisation and, therefore, energy product can be observed. Thus, exchange coupling between soft and hard magnetic layers is popular and often attempted. Exchange coupling between Sm-Co/Fe-Co magnets yields  $(BH)_{\text{max}} \sim 6 \text{ MGOe}$  ( $\sim 48 \text{ kJ/m}^3$ ) [Alo95]. Based on similar principles of exchange coupling Sm-Co/Fe-Co but through interdiffusion between Fe and the Co-rich  $\text{SmCo}_6$  compound (along with some sprinkling of Cu, which reduced the crystallisation temperature and is well known for its segregating property at the grain boundaries), Zhang *et al.* could achieve strong exchange coupling between Fe-Co and  $\text{SmCo}_5$  layers, which showed single phase magnetisation hysteresis behaviour giving an energy product of about  $32 \text{ MGOe}$  ( $\sim 255 \text{ kJ/m}^3$ ) [Zha05]. This  $(BH)_{\text{max}}$  is higher than the available  $(BH)_{\text{max}}$  for commercial sintered magnets. Studies on (Sm-Co)-T (Co and Fe) layers by Fullerton and co-workers indicated an exchange spring behaviour of magnetisation (large  $M_{\text{irr}}$  with increasing reversal fields) in (Sm-Co)-Co multi-layers on MgO(100) single crystals [Gri98]. Energy products of  $70 \text{ MGOe}$  ( $\sim 558 \text{ kJ/m}^3$ ) were reported for the case of exchange coupled (Sm-Co)-Fe layers on MgO(110) single crystal substrates [Sow98].

## 3 Thin Film Structures

Thin films are structures that are highly extended in two dimensions, and the third dimension is greatly reduced with respect to the first two. Thin film structures begin to play an important role in deciding the properties of a material, when this third reduced dimension, normally the thickness of the film, becomes comparable to some characteristic dimension in the system, like the domain wall width, in magnetic systems. However, if the thickness can not be compared to some characteristic length scale of the system, thin films still offer possibilities to manipulate the length scales within the system (e.g. grain size) more easily than in their bulk counterparts. Hence, the properties (magnetic, optical...) in thin films are substantially different in nature and in quantities as compared to the bulk products of the same material. Some of the topics concerning thin film phenomena are briefly described here and an in-depth information may be obtained elsewhere [Cho69], [Ohr91].

### 3.1 Growth Modes – Nucleation to Continuous Films

TEM investigations on various kinds of thin films formed from different deposition processes prove that the basic mechanisms of thin film development proceeds through the initiation of a nucleation stage [Mad66]. As the substrate is exposed to a plume of evaporated material, several extremely small particles (sub critical clusters) are left on the substrate surface. Some of these particles evaporate back to the vapour and several aggregate more vapour atoms until they form stable entities or stable clusters. With increasing deposition time, these small clusters grow in size forming bigger islands, and a collective coalescence starts. The orientations are preserved inside these islands and at the interfaces between them. Further growth of islands results in a saturation of the island density on the substrate surface and thereafter in an eventual decrease in island density. The islands after this stage more or less form a continuum with voids in between. Further exposure to vapour fills these voids and ultimately a continuous film is produced. Epitaxial films would be formed if the initial orientation of the stable nucleus is maintained despite subsequent coalescence of islands and continued deposition. All thin films can be said to have one of the three general growth modes, explained below.

**(a) The Volmer-Weber Growth Mode**

The Volmer-Weber growth mode means that the initial nuclei on the substrate grow to form 3-dimensional islands resulting in non-uniform coverage of the substrate surface. Also called the *island mode* of thin film growth, it occurs when the binding forces between the particles of material to be deposited is stronger than the forces between the material and the substrate. A schematic showing island growth is presented in Fig. 3.1.

**(b) The Frank-van der Merwe Growth Mode**

As an exact opposite of the above growth mode, the Frank-van der Merwe growth mode is also commonly called the *layer growth* for thin films (Fig. 3.1). When the binding between the film and the substrate is stronger than the binding between the film particles, layer growth is observed. Here, a uniform monolayer of the material is deposited in two dimensions forming planar sheets and so long as the bonding energy decreases continuously towards the bulk crystal value, the layer growth is sustained.

**(c) The Stranski-Krastanov Growth Mode**

The Stranski-Krastanov growth mode is the one in which both the above two growth modes merge. Initially, the binding between the deposit and the substrate is strong as required for layer growth, but eventually if the monotonic decrease in binding energy between subsequently deposited layers can not be observed, layer growth transforms into an island growth.

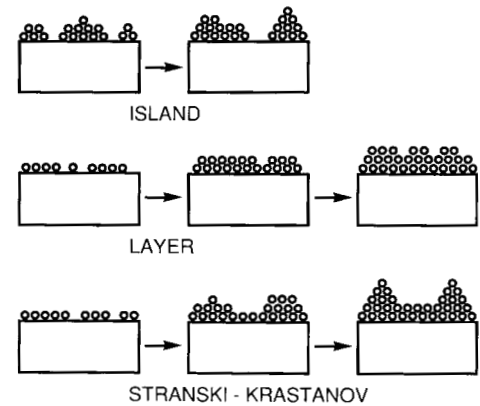


**Fig. 3.1:** The three thin film growth modes [Ohr91].

## 3.2 Epitaxial Thin films

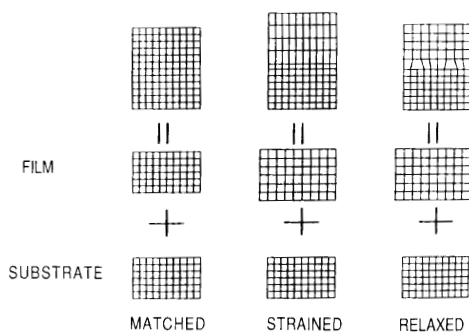


**Fig. 3.2:** Modes of epitaxy [Ohr91].

When atomic level perfection in single crystals is desired, epitaxial films are one good solution. Epitaxy means the growth of a single crystal film on a crystalline substrate surface such there is a fixed, well defined crystallographic orientation relation between the growing film and the substrate. In other words, epitaxy requires a 2-dimensional film's lattice control with respect to the substrate. Epitaxy in thin films is fully defined if there exists a parallelism between only one set of directions in the substrate and the overgrown film and only one set of

substrate planes are parallel to one set of film planes such that

$$(HKL) \parallel (hkl) \quad (3.1a)$$

$$[UVW] \parallel [uvw] \quad (3.1b)$$

where (HKL) is a film plane parallel to a substrate plane (hkl) and [UVW] is a direction in the film which is parallel to a direction [uvw] in the substrate. A most general epitaxial relation may be expressed as:  $(HKL) [UVW] \parallel (hkl) [uvw]$ . In the case when the substrate and the growing film are of the same material, there exists no *mismatch* between the film and the substrate and the atomic structure across the interface is characterised by an atom-by-atom matching between the deposit and the substrate. The atomic planes in this case are continuous across the interface. This kind of epitaxy is called *homoepitaxy* or *matched epitaxy* (Fig. 3.2). *Heteroepitaxy* refers to an epitaxial growth in which the growing film and the substrate are of different materials. And therefore, results generally in a lattice mismatch  $f$  expressed as;

$$f = (a_0(s) - a_0(f))/a_0(f) = \Delta a_0/a_0 \quad (3.2)$$

where  $a_0(s)$  is the lattice constant of the substrate, and  $a_0(f)$  that of the film. Any lattice mismatch of less than 9% may lead to pseudomorphic growth of the film on the substrate which means that the film lattice is strained to fit exactly over the substrate lattice [Fra49]. This mode of epitaxy is also called *strained epitaxy*. An increase in film thickness leads to an increase in the strain energy compared to the energy associated with the formation of dislocations and, therefore, the strain is released at a certain thickness by introducing misfit dislocations giving way to relaxed epitaxy with misfit dislocations. A schematic showing the three different types of epitaxial growth modes can be seen in Fig. 3.2.

Although perfect epitaxial films try to substitute single crystals for suitable applications, defects in epitaxial films can severely degrade the structural quality. They can be classified into five principal categories [Str82]:

1. *Defects propagating from the substrate into the film.* A substrate with dislocations can easily transfer its dislocations to the growing film. The film grows defect-free laterally, spaced with regions affected by dislocations running from the substrate into the film.
2. *Stacking faults* are produced when the regular arrangements of layers of atoms is disturbed. Three layers of atoms may have a general growth sequence of ABCABCABC, however, if an extra plane is inserted or a plane is removed, resulting in ABCCABCABC or ABCBCABC stacking sequence, the normal stacking is disturbed and stacking faults are produced.
3. *Precipitates* arise from an intentional addition of dopants in the system and are generally produced during reactions subsequent to growth.

4. *Grain boundaries and twins*: Stresses and strains during heteroepitaxial growth or the coalescence of misoriented clusters to form bigger islands results in low angle grain boundaries and twins. These are effective sources to cause strong pinning of domain walls in the system.
5. *Misfit dislocations* arise due to lattice misfit between the substrate and the film. Lattice strains can cause the substrate and the film to move opposite to each other, producing a set of lattice misfit dislocations which lie in the plane of the film.

However, these defects in epitaxial films must not always be considered “evil”, since some suitable defects have the potential to act as pinning sites and cause domain wall pinning in magnetic thin films.

## 3.3 Review: Sm-Co Thin Film Growth

The attractive properties such as the high saturation magnetisation and the very high anisotropy fields of Sm-Co make it an excellent candidate for production and observation of high-quality magnetic systems. Soon after the discovery in 1967, research on Sm-Co magnets progressed rapidly worldwide and this section shortly summarises the work done so far concerning Sm-Co thin-film magnets.

### 3.3.1 Textured Sm-Co Films

Sm-Co grown in any composition (corresponding to the phase diagram) with almost any deposition technique shows an inherent in-plane anisotropy of variable strength depending on the degree of optimisation achieved or desired. Immense early work is available in the literature on sputter-deposited Sm-Co films. Cadieu and co-workers [Cad87a] presented work on cold-deposited and post annealed SmCo<sub>5</sub> thin films (1–2 μm) from composite targets of 16 at.% Sm. Crystallisation of SmCo<sub>5</sub> particles in post annealed amorphous films and excellent columnar growth in SmCo<sub>5</sub> samples deposited on to heated substrates could be observed. Hegde *et al.* [Heg93] again reported on sputter deposited SmCo<sub>5</sub> films deposited on to moderately heated (350 °C) polycrystalline Al<sub>2</sub>O<sub>3</sub> substrates with varying thicknesses from 50 nm to several μm. The films showed maximum  $H_C$  values of about 1 T and a very weak in-plane texture. On alternative substrates (Yttrium Iron Garnet - YIG) [Cad94] and with thicker films (80–120 μm), energy products of about 16 MGOe (127 kJ/m<sup>3</sup>) could be obtained by sputtering again.

A strong dependence of magnetic in-plane texture and coercivity was observed by Neu *et al.* in sputter-deposited Sm-Co films on heated Al<sub>2</sub>O<sub>3</sub> substrates with varying Sm content [Neu99]. Both the coercivity ( $H_C \sim 1.7$  T) and the in-plane magnetic texture got stronger with increasing Sm content, which was interpreted as an effect of the increased mobility of Sm atoms and grain growth

at higher rare earth concentrations. However, similar experiments with pulsed laser deposition from elemental targets on heated SiN/Si substrates showed a reduction in magnetic in-plane texture with increasing Sm content, the films got isotropic at 20 at.% Sm [Neu02b]. Direct sputtering from compound targets directly onto moderately heated substrates has been essentially the focus till now, which yielded films with a preferential in-plane texture, weak anisotropies and coercivities of not more than 2 T [Cad87a].

With shadowed PLD [Cad98] (showing considerable decrease in droplet density) on heated polycrystalline Al<sub>2</sub>O<sub>3</sub> substrates, SmCo<sub>5</sub> films with  $H_C \sim 1$  T were achieved by Cadieu *et al.* A further grain refinement from 1  $\mu\text{m}$  to 0.2  $\mu\text{m}$  doubled their  $H_C$  [Cad99]. A weak out-of-plane anisotropy was reported by Neu *et al.* in SmCo<sub>5</sub> on pulsed laser deposited films of comparable compositions when the deposition atmosphere was changed from UHV to 0.06 mbar Ar atmosphere [Neu02a]. In 1993, Chen and co-workers reported as well on perpendicular anisotropy in cold-deposited Sm-Co samples of 23 at.% Sm on Al<sub>2</sub>O<sub>3</sub> corundum substrates [Che93]. The anisotropy in these samples changed strongly as a function of annealing atmosphere (high Ar pressures) and temperature. Deposition of these thin films in presence of an in-plane magnetic field (0.3 T) and post annealing in the presence of a magnetic field of similar magnitude (0.3 T) applied normal to the deposition field at substrate temperatures of 680 °C, and high Ar base pressures (100 mTorr) induced a convincing out-of-plane texture, however, with a very reduced anisotropy field of only 7–8 T. The origin of the out-of-plane anisotropy in these samples is thought to be a “*growth induced structure*”. Recent reports on enhancing the perpendicular c-axis component in SmCo<sub>5</sub> were presented by Sayama *et al.* in sputter-deposited SmCo<sub>5</sub> films on Cu/glass substrates [Say05a]. They exploited the layered structure of Sm and Co atoms in the Sm-Co unit cell to be the background for producing films with higher c-axis out-of-plane component and hypothesised that a film with very thin sublayers of Sm (0.31 nm) and Co (0.41 nm) on a Cu seed layer is capable of showing perpendicular anisotropy. However, very low  $H_C \sim 0.4$  T with a remanence squareness (RSQ) of only about 0.5 and only a very shallow increase in out-of-plane hysteresis compared to an in-plane hysteresis possibly requires more experimentation to support the claims. An improvement in the Cu buffer with a reduced roughness (from 26 nm on hot substrates to 4 nm on substrates at 20 °C) improve the RSQ to 0.85 and increased  $H_C$  to 0.8 T [Say05b]. A successful deposition of SmCo<sub>5</sub> with a uni-axial out-of-plane anisotropy was demonstrated by the same group on Cu/Ti underlayers with  $H_C > 1$  T and a perfect RSQ of 1 [Say05c].

In short, both sputtering and pulsed laser deposition have proven to be suitable thin film deposition techniques for producing Sm-Co films of various compositions with in-plane and out-of-plane anisotropies. The work introduced in this subsection was limited to depositions on amorphous or polycrystalline substrates. The texture in the films evolved due to post annealing or annealing in the presence of magnetic fields or due to textured growth on heated substrates with smooth

buffers. All the films had low coercivities of  $H_C < 2$  T compared to the potential of Sm-Co as a material having the highest anisotropy field  $H_A > 30$  T. The easy solution to exploit the intrinsic anisotropy of this material lies in attempting epitaxial growth with predictable textures and well oriented films. This would result in the highest coercivities, limited only by the intrinsic properties of this compound.

### 3.3.2 Epitaxial Sm-Co Films

A detailed analysis of Cr as a buffer for Sm-Co films was performed by Liu *et al.* in 1994/95 [Liu95]. They reported that sputter deposited Sm-Co films from compound targets of 21 at.% Sm (and with a stoichiometric transfer of the composition into the film), tend to grow directly onto Cr/glass crystallites and not in the voids existing in the discontinuous Cr buffer. This was achieved up to a Sm-Co layer thickness equal to the maximum buffer layer thickness (96 nm in this case). At higher thicknesses, Sm-Co diffuses through the voids down to the substrate. An informative schematic of their work is seen in Fig. 3.3.

These observations have been confirmed by Velu *et al.* who reported that thin sputter deposited Sm-Co films ( $< 20$  nm) on thin Cr buffers ( $< 35$  nm) replicate the isolated columnar Cr buffer morphology [Vel94]. The same group of Liu *et al.* suggested  $(\bar{1}100)[0001]$  Sm-Co epitaxy locally with a nominal 21 at.% Sm onto  $(\bar{1}2\bar{1})[\bar{1}01]$  Cr/a-glass substrates (amorphous-glass substrates) [Liu96]. They supported their claims for this epitaxial relation from the low lattice mismatch of only about 2% between Sm-Co  $(\bar{1}100)$  and the Cr  $(\bar{1}2\bar{1})$  planes. Moreover, TEM diffraction patterns show the predicted epitaxy locally. Zangari and co-workers [Zan99] also investigated Sm-Co grown on highly oriented epitaxial Cr/Ag templates on Si substrates of (001), (111) and (110) orientations but observed no local crystallographic order. The magnetic properties, even though anisotropic on Si (110), were however inferior to those reported on Cr/glass substrates.

One year after the work of Liu *et al.*, twofold and uniaxial c-axis growth of Sm-Co with 21 at.% Sm was shown by Fullerton *et al.* on Cr/MgO(100) [Ful97] and on Cr/MgO(110) single crystal

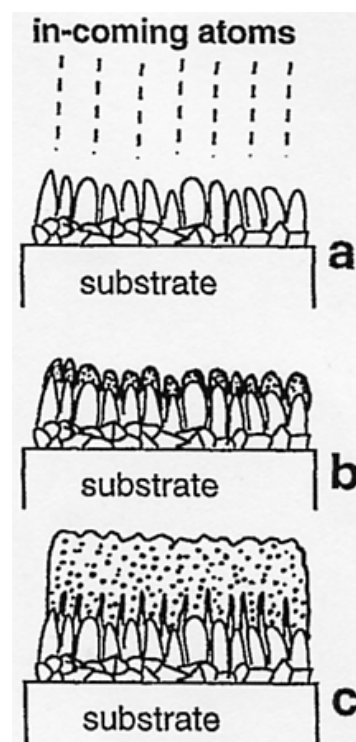


**Fig. 3.3:** (a) Morphology of Cr buffer with voids (b) 24nm Sm-Co on top (c) 96 nm Sm-Co on top [Liu95].

substrates [Reh97] respectively.  $H_C$  close to 3.5 T could be seen at a Sm-Co thickness of 50 nm on MgO(100) and MgO(110) single crystal substrates which is very similar to  $H_C$  of 3.1 T reported in this work for comparable Sm-Co thickness and composition. The group earlier reported epitaxially growing Sm-Co (11 $\bar{2}$ 0)[0001]||W(100)[011]||MgO(100)[010] with equally high  $H_C$  of 3.1 T. The high coercivities, despite large grain sizes (200 nm), were attributed to a high density of twin boundaries compared to grain boundaries which act as crucial microstructural defects governing coercivities [Ful96]. An important finding that gets apparent in these fully crystallised, well textured samples is the ambiguity related to composition. Most of the reports quote the composition as "nominal composition" due to extreme difficulty in depositing pure Sm-Co samples of one fixed and known composition. This is understandable from the phase diagram, observing the number of existing phases in a narrow composition range. To alleviate the problem is the fact that all these phases have very similar crystal structures. Therefore, XRD is an insufficient tool, especially for epitaxial films where very few reflections are available as markers for phase and structure identification. A comprehensive work is reported in the literature from M. Benaissa *et al.* who have successfully identified the existence of SmCo<sub>3</sub>, Sm<sub>2</sub>Co<sub>7</sub> and SmCo<sub>5</sub> layer stacking in one sample with a nominal composition of 20 at.% Sm [Ben98].

## 4 Film Preparation and Characterisation Techniques

### 4.1 Pulsed Laser Deposition

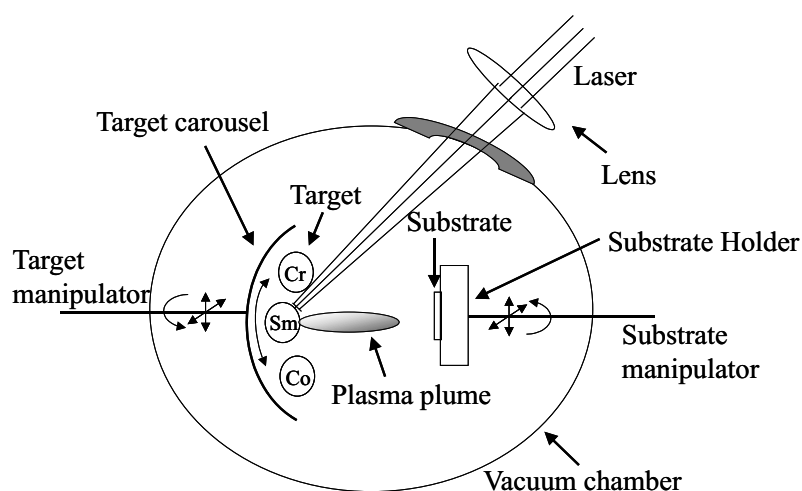


**Fig. 4.1:** Pulsed laser deposition set-up.

As a very versatile and well established technique, pulsed laser deposition (PLD) is used for deposition of materials that are difficult or impossible to deposit using other evaporation methods, due to the lack of sufficient energies for material evaporation especially at very different vapour pressures. The method of pulsed laser deposition requires a laser beam (pulsed excimer laser) to be directed on a target. A sharp temperature rise occurs in a very short time on the target surface ( $\sim 10^8$  K/min), which causes vapourisation (ablation) of target material. A plasma of neutral atoms, ions, electrons etc. is produced due to interaction of evaporated material with laser radiation, which propagates towards the substrate placed parallel to the target and condenses on the substrate surface. This mode of PLD is called the *on-axis PLD* and a general set-up can be seen in Fig. 4.1. The main advantages of this technique are the stoichiometric transfer of even rather complex, multi-elementary target material into the film and deposition of several different materials to produce multi-layered structures. Equally important is the deposition of materials in several different high pressure atmospheres, which can be carried out with relative ease. Hence, this method offers enormous flexibility in system design with respect to target materials, choice of substrates,

reactive high pressure depositions for achieving stoichiometric films, to name a few. High plasma velocities make deposition rates in the order of few nm/pulse achievable with moderate laser fluence even under ultra high vacuum (UHV) conditions.

Several variations to the original on-axis PLD technique have been introduced since its conception in 1962, by Breech and Cross [Bre62] who could demonstrate the vaporisation of atoms from solid surfaces using ruby laser. In 1965, Smith and Turner finally produced thin films with laser ablation [Smi65]. However, the technique remained dormant for nearly two decades, until it was brought back to focus successfully by Dijkkamp and Venkatesan [Dij87]. Pulsed laser deposition has ever since established itself to be a useful technique for deposition of complex materials like the superconducting oxides [Roa88]. It moreover often leads to a stoichiometric transfer of the material from the target onto the substrate. However, repeated laser pulsing causes the target surface to erode and develop cones, which break off the target and are deposited on the substrate as bulk particulate matter, the so-called *droplets*. These droplets can be as large as several microns in size and are completely undesirable. Droplets in PLD can be reduced by renewing the target surface by mechanical polishing, rotating the target continuously during deposition or using *off-axis PLD*, in which the substrate placed with the substrate normal perpendicular to the plume expansion direction and most of the droplets simply fly over the substrate surface [Hol92]. Additionally, *shadowed PLD* is also used by several researchers to avoid droplet formation [Cad98], where a shadow mask is placed close to the substrate and the droplets are blocked.

Thin films of Sm-Co were deposited using *UHV PLD* (base pressure  $\sim 10^{-9}$  mbar). The laser beam (KrF excimer laser with  $\lambda = 248$  nm, repetition rate  $f \sim 1-50$  Hz, pulse duration  $\tau \sim 10-50$  ns and power  $P \sim 10$  MW) is directed into the chamber with the help of two UV sensitive mirrors and an aperture that removes incoherent parts from the beam which lead to an inhomogeneous energy distribution at the edges of the laser spot. This projected image of the aperture produced by the laser beam, rasters the target surface sitting in an eight target

carousel (Targets are placed at the imaging position rather than the focus, since a surface ablation and not a depth profiling of the targets is needed.) A multi-target carousel housing elemental targets permits enormous flexibility in the materials to be deposited. Fast computer controlled movement of the targets (X, Y, and rotation) delays target ageing and minimises droplet density on the substrate. Homogeneous films are deposited on substrates under uniform continuous computer-aided substrate rotation. To maintain UHV conditions in the chamber for as long as possible, the deposition chamber is connected to the outside with a smaller loadlock chamber (base pressure

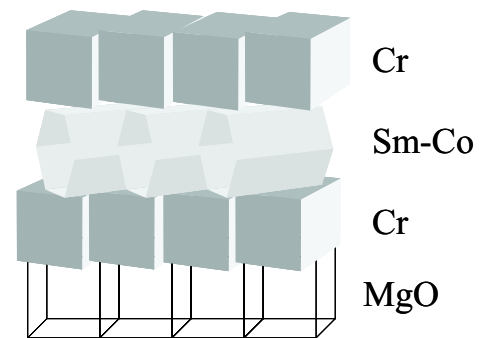


**Fig. 4.2:** Layer scheme for films prepared on single crystal MgO substrates.

$10^{-8}$  mbar). It has a capacity for 16 substrates and 10 targets at a time. Transfer between the loadlock and the deposition chamber is conveniently realised with a *transfer fork* (designed for target and substrate transfer), avoiding opening the chamber. Prior to deposition, targets are cleaned with 1000 pulses at 10 Hz, 100 mJ energy of the laser and the individual deposition rates of different targets in the chamber are recorded with an Inficon XTM 2 rate monitor positioned exactly at the substrate position (since the plume in PLD is highly directional, the deposition rate can be severely degraded just a few mm off the substrate). The Sm and Co deposition rates are typically 0.5 Å/pulse and 0.06 Å/pulse respectively. One side polished, 0.2 mm thick, preheated MgO 1 cm × 1 cm single crystals were used as substrates. A thin Cr layer (10 nm) acted as buffer for 40–50 nm of hard magnetic Sm-Co layer and the whole assembly was covered with Cr *cap layer* (10 nm) for oxidation protection. This layer schematic is presented in Fig. 4.2.

Several easily variable and controllable parameters during deposition can alter the film properties remarkably. The effect of substrate temperature and laser repetition rate were essentially investigated in this work. These variable and other constant deposition parameters have been summarised in Tab. 4.1.

**Table 4.1:** Standard PLD parameters.

Parameter	Cr (Buffer)	Sm-Co	Cr (Cover)
Substrate	MgO(100) /(110)	MgO(100) /(110)	MgO(100) /(110)
Energy (mJ)	100	100	100
Frequency (Hz)	15	2–15	15
Pressure (mbar)	$10^{-9}$	$10^{-9}$	$10^{-9}$
T-S distance (mm)	46–72	46–72	46–72
Temperature (°C)	200–700	350–800	< 200

## 4.2 Phase and Texture Analysis

The possibilities of several phases co-existing in the Sm-Co phase diagram make the need for a detailed phase analysis of the samples necessary. Information on existing phases in the system can be obtained from the reflections in x-ray diffraction patterns. For epitaxial and therefore highly textured Sm-Co films, however, this information is severely restricted due to few observable peaks in the standard Bragg-Brentano geometry, where only the planes parallel to the substrate are probed. However, several other tools like pole figure measurements and energy dispersive X-ray analysis facilitate distinction between these phases in addition to providing information on the texture of samples.

**(a) Energy Dispersive X-ray Analysis (EDX)**

Energy Dispersive x-ray analysis is a reliable method for quantitative and qualitative detection of elemental composition of samples. With normal detectors, it is capable of detecting elements (atomic number  $Z > 11$  with Si (Li) detectors and with windowless detectors down to  $Z < 6$ ) in low amounts of  $\sim 0.1$  wt.% to an accuracy of 0.1–1% with spatial resolution of few micrometers.

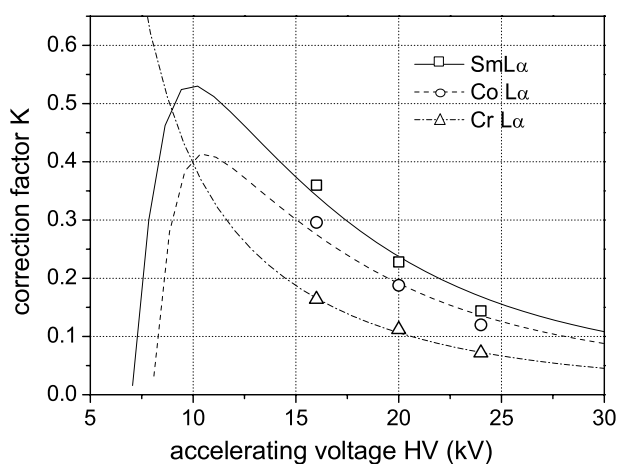


**Fig. 4.3:** Application of STRATagem software on EDX measurements. Experimental  $K$ -ratios (see text) measured at three different accelerating voltages of 16 kV, 20 kV and 24 kV for  $\text{CoK}_\alpha$ ,  $\text{SmL}_\alpha$  and  $\text{CrK}_\alpha$  and theoretical curves (lines) obtained in a fit procedure resulting in individual layer thickness and composition.

Compositional characterisation was performed in a Philips XL20 SEM with an EDAX system having a thin window detector. EDX spectra for  $\text{SmL}_\alpha$ ,  $\text{CoK}_\alpha$  and  $\text{CrK}_\alpha$  radiation were recorded from the sample and analysed with *Genesis* software. Simultaneous measurements were made from  $\text{SmCo}_5$  and Cr bulk standards under necessarily constant working distance and electron beam parameters, for comparison with measured Sm and Co intensities from the sample. A simulative software [Car31] correlates the characteristic x-ray intensity emitted at different accelerating voltages from elements with thickness and composition of these elements present in the sample. It defines a  $K$ -ratio which is the ratio of intensity emitted from the sample to the standard, normalised to the atomic composition of the standard to the sample and depends on the thickness of the film exciting the radiation (hence  $K \propto I_{\text{sample}} / I_{\text{standard}}$ ). Measurement of  $K$  determines thickness and composition of the sample. To add statistics for reliable results, measurement of  $K$  is done at several (3–4) electron-beam accelerating voltages. The plot of  $K$  vs accelerating voltage  $V$  is shown in Fig. 4.3. The experimental data points ( $\circ$ ,  $\triangle$ ,  $\square$ ) are fitted with a calculated curve for intensity variation with accelerating voltage. For well fitted data, thickness and compositional values are reliably known to within 1% accuracy.

**(b) X-ray Diffraction**

X-Ray diffraction (XRD) from a set of sample atomic planes parallel to the substrate satisfying Bragg's diffraction condition ( $n\lambda = 2d \sin \theta$ ), confirms crystallinity in samples. Moreover, textured samples show preferential reflections only from a certain family of atomic planes denoted as  $\{hkl\}$ . Knowledge of d-spacing of these planes (seen in XRD spectrum), can be used for phase identification by comparison with the powder diffraction file (pdf) database.

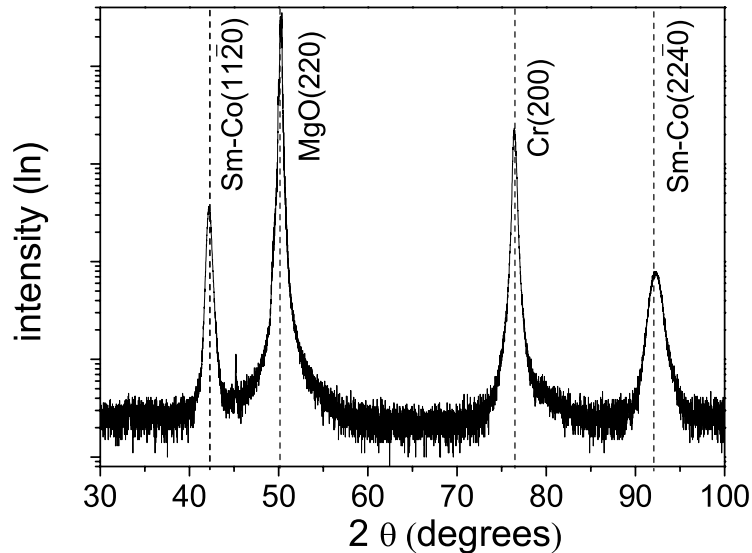


**Fig. 4.4:** XRD of a Sm-Co/Cr sample deposited on heated MgO(100) single crystal substrate. Besides the substrate (100) reflections, clearly identifiable is the (200) buffer reflection and  $\text{Sm}_2\text{Co}_7$  ( $11\bar{2}0$ ) and ( $22\bar{4}0$ ) reflections.

Thin film Sm-Co samples were X-ray analysed using  $\text{CoK}\alpha$  in the standard Bragg-Brentano Geometry in a SIEMENS D 5000 X-ray diffractometer. Measured XRD from a  $\text{Sm}_2\text{Co}_7$  sample is shown in Fig. 4.4. Noticeable are the sharp and well defined diffraction peaks from the substrate, buffer and Sm-Co film. The positions of each of the reflections can be identified with a certain set of planes from the pdf (powder diffraction database). Therefore, on a (100) single crystal MgO substrate, Cr buffer is (100) oriented (the information must come from the buffer, because the Cr cover layer is cold deposited) and Sm-Co shows (110) growth. Since only one family of planes  $\{hkl\}$  from the different layers is seen, the sample is textured with the Sm-Co c-axis lying in-plane. These are the planes parallel to the substrate surface and, hence, provide only half the information, viz about the *out-of-plane* orientation of the sample.

Although XRD is a powerful tool in checking the degree of crystallinity and texture in samples, it does not provide any information on in-plane orientation of the samples. Phase identification also gets tricky with XRD for highly textured or epitaxial films because of the limited number of reflections to compare from the sample with pdf database.

**(c) Pole Figure Measurements**

A more powerful texture and phase analysis tool for textured samples is the measurement of pole figures. Although mainly used for texture analysis, it can also be successfully employed to identify phases in the samples. Rotation and tilting of a sample at constant  $2\theta$ , corresponding to a particular set of "non-parallel" planes (set of parallel planes not parallel to the substrate surface) in the sample, produce a map of the concerned plane in spherical 3-D space. A 2-D stereographic projection of this mapping from one hemisphere produces *pole figures* where each pole is a reflection from a set of parallel planes belonging to the  $\{hkl\}$  family of planes. The appearance of distinct poles indicates in-plane texture (distinct epitaxy) in the sample and the pole width is the criterion for texture quality.

Sm-Co samples were measured with a Philips X'Pert texture goniometer with a secondary monochromator and  $\text{CuK}\alpha$  radiation up to a tilt ( $\psi$ ) of  $70^\circ$ . Due to the fourfold symmetry of MgO(100) single crystal substrate, quarter pole figures were sufficient to analyse complete sample textures. Similarly for MgO(110) substrates half pole figures were required to get the full epitaxial information. As an example a measured  $(11\bar{2}6)$  quarter pole figure of  $\text{Sm}_2\text{Co}_7$  is shown in Fig. 4.5.

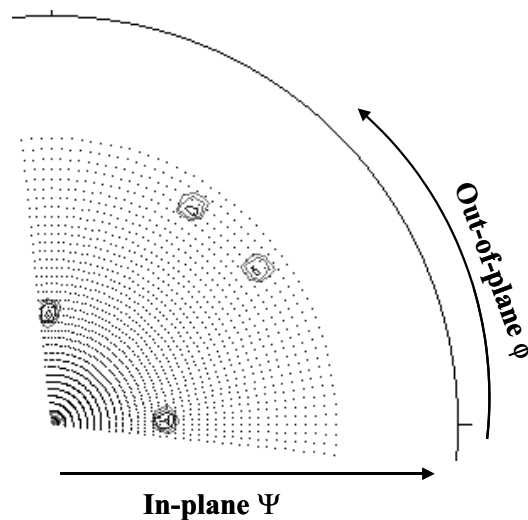


**Fig. 4.5:**  $(11\bar{2}6)$  quarter pole figure of  $\text{Sm}_2\text{Co}_7$  on MgO(100) single crystal substrate. Four sharp and distinct poles are in agreement with predicted  $(11\bar{2}6)$  pole figure. Courtesy: R. Tamm – TU Dresden.

Prior to starting a pole figure measurement for a certain reflection, the  $2\theta$  value was optimised on an expected pole for maximum intensity. Then the samples were measured at fixed  $2\theta$  values. Comparison between the experimentally measured and theoretically predicted  $2\theta$  values with one or the other phases enabled phase identification. Several pole figures were measured in each sample to strengthen phase identification results. Additionally noticeable is the fact that although TEM provides local information on epitaxy and texture in the sample, for global confirmation of these results from complete depth of the sample, pole figure measurements are completely indispensable. Pole figure measurements shown in this work were performed by R. Tamm from TU Dresden.

### 4.3 Microscopical Investigations

Microstructural analysis of Sm-Co thin films were performed in a scanning electron microscope (SEM) and an atomic force microscope (AFM). For details of atomic arrangement, epitaxy and texture, transmission electron microscopic (TEM) investigations were useful.

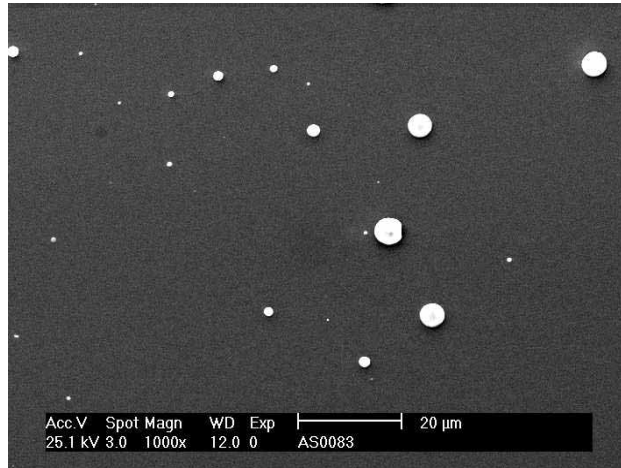


**Fig. 4.6:** SEM image of a Cr/Sm-Co/Cr/MgO sample. Big white chunks on the film surface are droplets present in the sample, which are almost unavoidable in PLD.

SEM uses an electron beam to magnify and image a sample surface. The electron beam is focussed to a very fine spot on the sample using condenser lenses. Scanning coils raster the electron beam on the sample, and from each spot, a detector collects the secondary electrons (SE) emitted from the sample and reconstructs the sample surface. Hence, this imaging mode essentially provides topographic information. The Sm-Co film microstructure was analysed with a Philips XL20 SEM, in the SE mode. Even at low magnification, Cr and Co droplets (which are a by-product of PLD) could be identified and an estimate on the droplet density was possible. So, although Cr is relatively harmless, soft magnetic Co droplets can severely degrade the hard magnetic hysteresis of Sm-Co samples. With an estimated droplet density and size, a correlation with the soft magnetic shoulder in the magnetic measurements was possible. Due to a very fine grain structure (grain sizes  $\sim 40\text{--}50$  nm), the grain boundaries were not easily tractable under limited, practically achievable spatial resolution of the microscope. A typical SEM micrograph is presented in Fig. 4.6.

Additional information on surface morphology and roughness was obtained from a Digital Instruments 3100 AFM equipped with Nanoscope IIIa. The AFM was used in a tapping mode, where a non-magnetic tip mounted on Si cantilever oscillates with a constant frequency over the sample surface and is sensitive to a force gradient between the tip and the sample. The distance between the tip and the sample is kept constant and the tip-sample interaction (or the force gradient) is tuned by measuring the z-shift of the cantilever through a feedback loop. The sample surface is reconstructed from the z variation experienced by the tip at each point of the scanned sample surface.

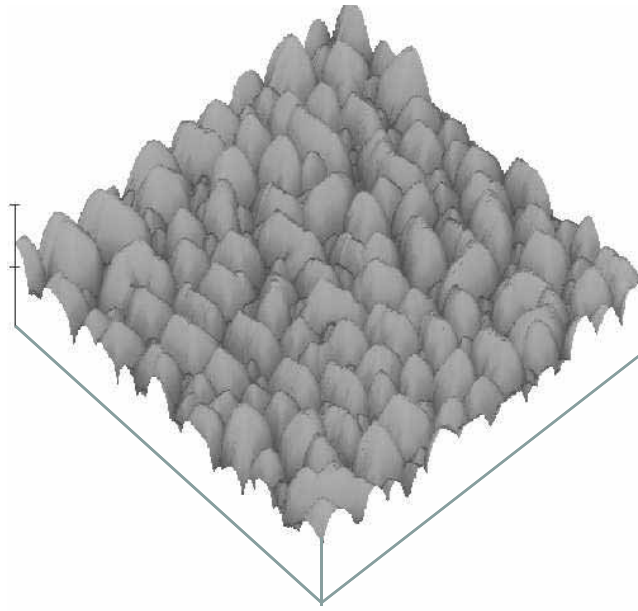


**Fig. 4.7:** 3D AFM micrograph ( $2 \times 2 \mu\text{m}$ ) of a rough Cr film showing surface topography. The z-range is 100 nm.

This is sensed by a laser which redirects this force gradient or tip-sample interaction into a position sensitive detector. An AFM micrograph of a Sm-Co sample surface is shown in Fig. 4.7. The software permits a useful 3-D topological view of the sample surface and calculation of surface roughness,  $R_{\text{rms}}$  (root mean square)

$$R_{\text{rms}} = \sqrt{\frac{1}{N} \sum_{i=0}^N (Z_i - \bar{Z})^2} \quad (4.1)$$

averaged over N measurement points, each with individual heights  $Z_i$  and  $\bar{Z}$  as the mean height. For detailed microstructural analysis, samples were analysed in cross-sectional TEM. Unlike in SEM, image formation in TEM occurs from electrons in the transmitted beam. Transmitted electrons from the sample are focussed by the objective lens and enlarged by projector lenses to form an image on a phosphorus plate. As is shown in Fig. 4.8 the attempted layer architecture for Sm-Co films on MgO single crystal substrates becomes clearly visible, and clean interfaces between different layers are observed. Epitaxial relationships between different layers are locally established by Fast Fourier Transform (FFT) on high resolution TEM images. Besides grain sizes, information on grain boundaries and phase purity can be provided by imaging individual atomic layer stacking in high resolution TEM. TEM presented in this work was performed by K. Subba Rao of TU Dresden.

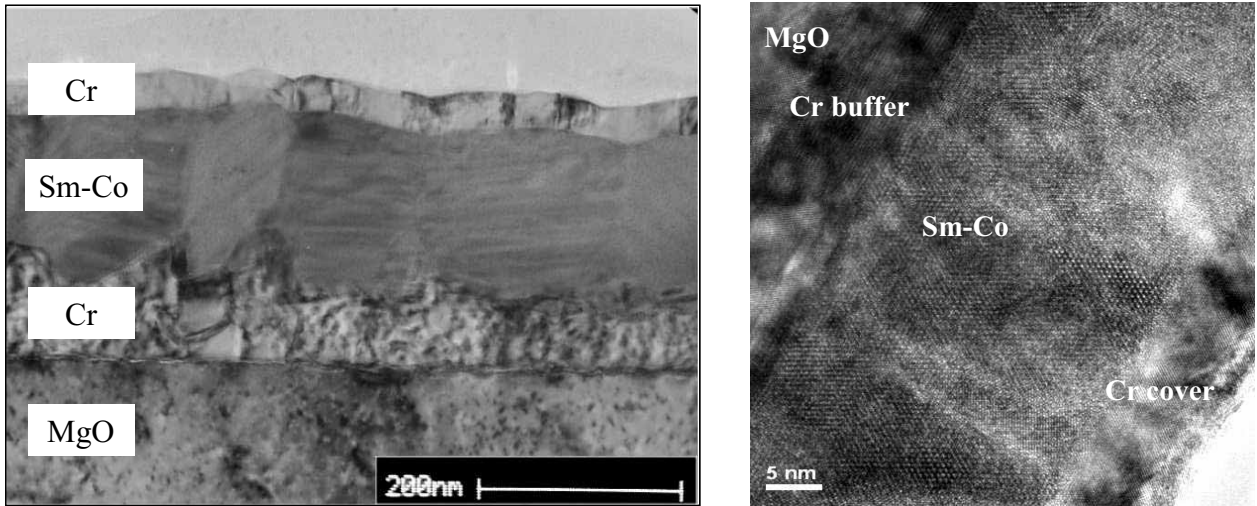


**Fig. 4.8:** (a) Columnar Sm-Co grain structure can be recognised in a TEM overview image. (b) High resolution TEM image showing fine atomic planes of various layers. Courtesy: K. Subba Rao – TU Dresden.

## 4.4 Magnetic Measurements

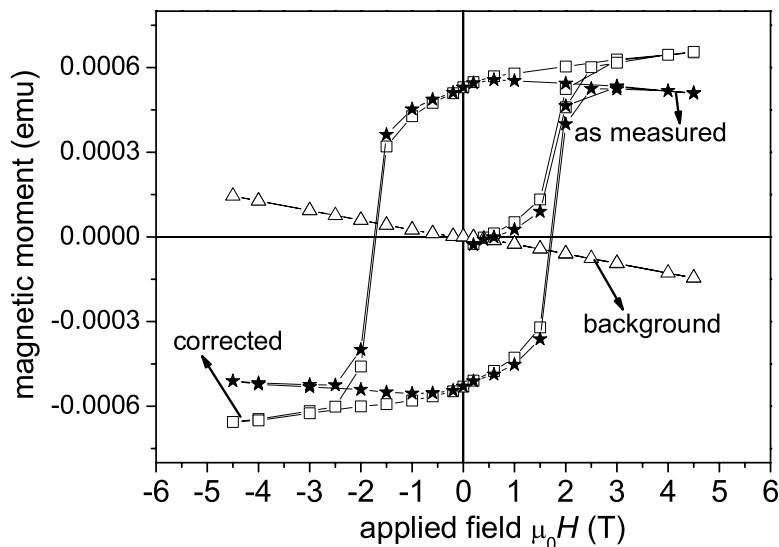


**Fig. 4.9:** Sm-Co hysteresis measurement with a 5 T SQUID. The background measurement is essentially a straight line and the step at zero field is negligible.

The magnetic properties of the samples were characterised with a 5 and a 7 T Quantum Design MPMS SQUID magnetometer and a 9 T Quantum Design PPMS vibrating sample magnetometer (VSM). SQUID magnetometers possess to-date the highest resolution for magnetisation measurements ( $\sim 10^{-7}$  emu). Due to very sensitive measurements of the magnetisation contribution from the sample holder and the bare substrate, trustable corrections for sample magnetisation can be obtained. The measurable range for samples, however, was limited by the 4.8 T of maximum ap-

plicable field and, therefore, detailed temperature dependent hysteresis measurements (where the coercivities approximately double at low temperatures) or several specialised measurements on thin samples of high coercivity were not possible with the SQUID. Hysteresis measurements of an epitaxial Sm-Co sample measured in a 5 T SQUID magnetometer is shown in Fig. 4.9. Three different hystereses correspond to the as-measured sample (contribution from Sm-Co film, MgO substrate and the SQUID holder), a measurement of the pure MgO substrate of nearly the same mass on the same SQUID holder (which makes the background measurement) and a corrected hysteresis, showing only the contribution of the film after subtraction of the background curve. Noteworthy is the very small and neat background contribution from the holder and bare MgO substrate. The sample response, in all cases, is presented as magnetic moment in emu (electromagnetic units).

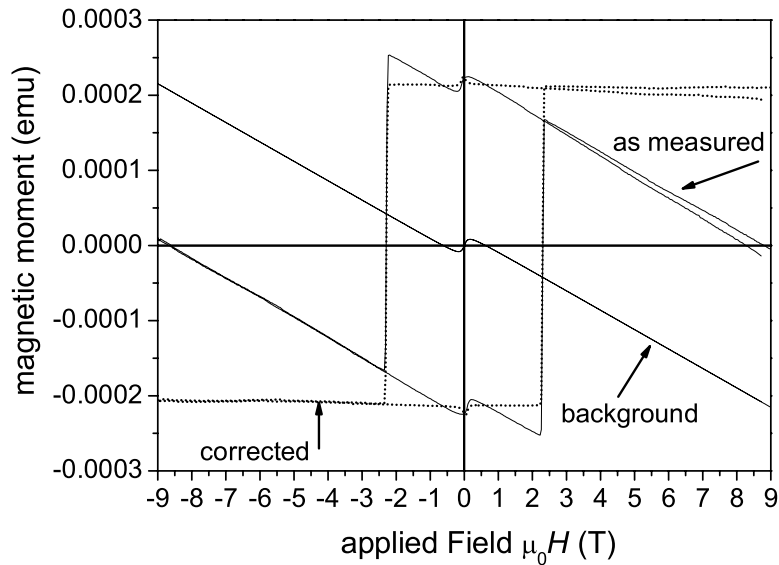


**Fig. 4.10:** Magnetic hysteresis of a Sm-Co sample measured with a 9 T PPMS VSM.

The 9 T PPMS VSM is an attractive alternative to the SQUID magnetometer. High fields, sufficient to saturate almost all thin film samples, in addition to very high sweep rates, of the order of 1.2 T/min, which enabled fast measurements, were achievable with a VSM set-up. VSM holders are easier to construct, to mount and dismount and the whole set-up offers greater flexibility. Detailed temperature dependent measurements up to 400 K are additionally possible. Figure 4.10 shows a typical as-measured sample hysteresis measured in a PPMS VSM, a measurement of a bare MgO substrate and the resultant hysteresis after subtracting the substrate contribution. For known sample volume  $V$  the as-measured magnetic moment  $m$  (in emu), both from the SQUID and the VSM, can be presented as polarisation  $J$  (in Tesla in SI units):

$$J = \frac{4\pi}{10^4} \left( \frac{m}{V} \right) \quad (4.2)$$

# 5 Growth and Epitaxial Relation of Sm-Co Films on Different Substrates

To investigate the magnetic and structural properties of various Sm-Co phases, epitaxial growth of Sm-Co as thin films was attempted. The knowledge of substrate symmetry and crystal structure was used to control the easy axis texture in Sm-Co films. One side polished 0.2 mm thick MgO single crystals of two different orientations, viz MgO(100) and MgO(110), were used as substrates. On MgO(110), due to reduced crystal symmetry, uni-axial growth of Sm-Co is achieved (section 5.2) as compared to the more symmetric MgO(100) single crystal substrates, on top of which Sm-Co grows with two symmetric c-axis orientations (section 5.1). Moreover, not only substrate-orientation effects but also the role of substrate-texture (section 5.3) on the c-axis growth of Sm-Co has been investigated in the case of Sm-Co films grown on textured MgO(100) buffered SiN/Si substrates.

## 5.1 Sm-Co Films on MgO (100) Single Crystal Substrates

On MgO (100) single crystal substrates, process parameters were optimised to obtain high coercivities and strongly textured Sm-Co thin films. Magnetic texture was characterised with the percentage of remanent polarisation lying along one specific substrate direction (by convention, out-of-plane in this work) or precisely, as the ratio of the remanent polarisation lying out-of-plane (along MgO [001]) to the remanent polarisation lying in-plane (along MgO [100]).

$$M_{\text{texture}} = \frac{J_{\text{R}}^{\text{OP}}}{J_{\text{R}}^{\text{IP}}} \quad (5.1)$$

where  $M_{\text{texture}}$  is the magnetic texture,  $J_{\text{R}}^{\text{IP}}$  the remanent polarisation parallel to MgO[100]  $\Rightarrow$  in-plane remanent polarisation, and  $J_{\text{R}}^{\text{OP}}$  the remanent polarisation parallel to MgO[001]  $\Rightarrow$  out-of-plane remanent polarisation. Naturally, if  $M_{\text{texture}} \sim 0$ , the film is perfectly "in-plane textured", vice-versa, in case,  $M_{\text{texture}} > 1$ , the film is "out-of-plane" textured.  $M_{\text{texture}} = 1$  corresponds to an isotropic film.

### 5.1.1 Growth of $\text{Sm}_2\text{Co}_7$ Phase

The growth of the hard-magnetic  $\text{Sm}_2\text{Co}_7$  phase was attempted on  $\text{MgO}(100)$  single crystal substrates. A Cr buffer layer was deposited with a laser repetition rate of 15 Hz and a laser energy of 100 mJ at a heater temperature of  $700^\circ\text{C}$  to an estimated thickness of 40 nm. X-Ray diffraction shows one sharp (200) buffer reflection and hence bcc Cr grows (100) oriented out of the film plane. Two distinct poles are seen in the (110) Cr half pole figure in Fig. 5.1a indicating that Cr grows  $45^\circ$  rotated in-plane on  $\text{MgO}(100)$  as per the epitaxial relation  $\text{Cr}[110](001) \parallel \text{MgO}[100](001)$ . FWHM (Full Width at Half Maximum) of less than  $2^\circ$  along  $\phi$  and  $\psi$  suggest good in-plane and out-of-plane texture in Cr. The easy epitaxy of Cr on MgO presumably arises from a tolerable lattice mismatch of only about 3.8% between the Cr(110) planes and MgO(100) planes. The morphology of the Cr buffer at  $700^\circ\text{C}$  was imaged with an AFM and can be seen as a 3-D image in Fig. 5.1. The buffer surface looks crack-free and smooth with a calculated rms roughness of 0.3 nm on a  $2\ \mu\text{m} \times 2\ \mu\text{m}$  imaged area from the Nanoscope IIIa software.

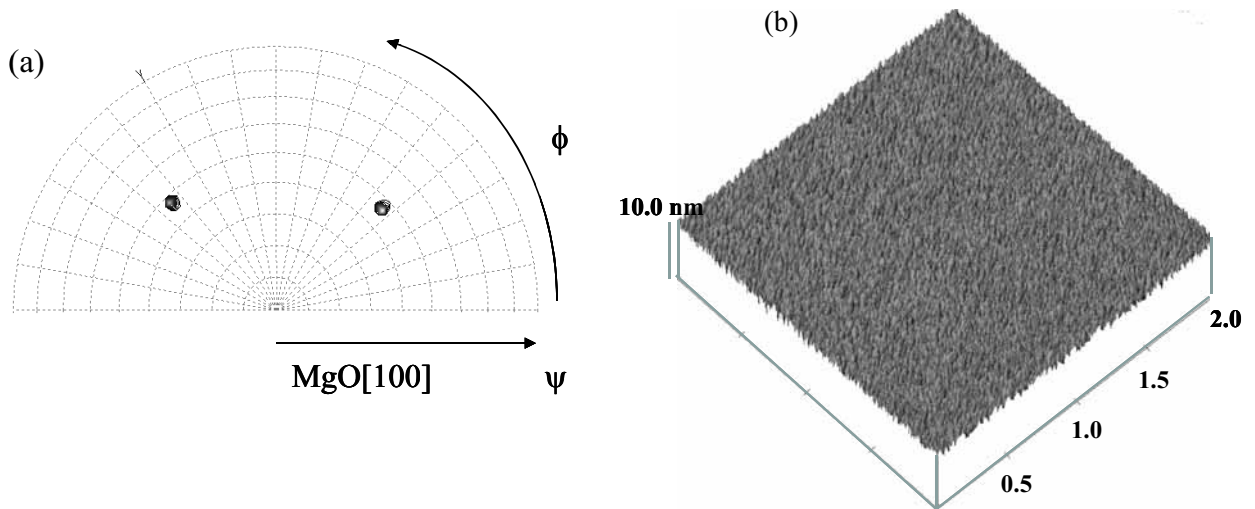


**Fig. 5.1:** (a): (110) Cr pole figure with two sharp poles indicating an in-plane textured Cr buffer layer, rotated by  $45^\circ$  with respect to  $\text{MgO}[100]$ . (b):  $2\ \mu\text{m} \times 2\ \mu\text{m}$  AFM micrograph of Cr buffer layer deposited at  $700^\circ\text{C}$  showing smooth buffer morphology.

#### (a) $\text{Sm}_2\text{Co}_7$ films with varying deposition temperature ( $750\text{--}450^\circ\text{C}$ )

An estimated 150 nm layer of Sm-Co was deposited at a temperature of  $750^\circ\text{C}$  on top of the Cr buffer. The number of pulses on Sm and Co targets were adjusted to obtain 20 at.% Sm in the films and the composition was reconfirmed from EDX measurements to be close to 22 at.% corresponding to the  $\text{Sm}_2\text{Co}_7$  phase. Besides the (100) substrate reflections, (200) buffer reflection as well as  $(11\bar{2}0)$  and  $(22\bar{4}0)$   $\text{Sm}_2\text{Co}_7$  reflections were recognised, however much weaker compared to the Cr buffer reflection (Fig. 5.2). Other theoretically strong  $\text{Sm}_2\text{Co}_7$  reflections are indicated (as dotted lines) in the XRD pattern in Fig. 5.2. The absence of these reflections hints a single

(110) out-of-plane growth of  $\text{Sm}_2\text{Co}_7$  phase with  $\text{Sm}_2\text{Co}_7$  c-axis lying in-plane. Additionally, a small reflection-cluster (marked with a circle) at  $35^\circ$  could be identified as  $\text{SmO}_2$  and  $\text{Sm}_2\text{O}_3$ . The magnetic hysteresis of this film seen in Fig. 5.2b shows hard magnetic properties with a coercivity of  $\sim 2$  T along  $\text{MgO}[100]$ . The out-of-plane hysteresis along  $\text{MgO}[001]$  is also large with comparable coercivity and the film shows weak out-of-plane magnetic texture. Hence, in conclusion, Sm-Co films at high deposition temperatures of the order of  $750^\circ\text{C}$  show weak Sm-Co reflections in the XRD, indicate the presence of oxides and have the undesired out-of-plane texture. These high deposition temperatures for  $\text{Sm}_2\text{Co}_7$  films can therefore be rendered unsuitable for deposition.

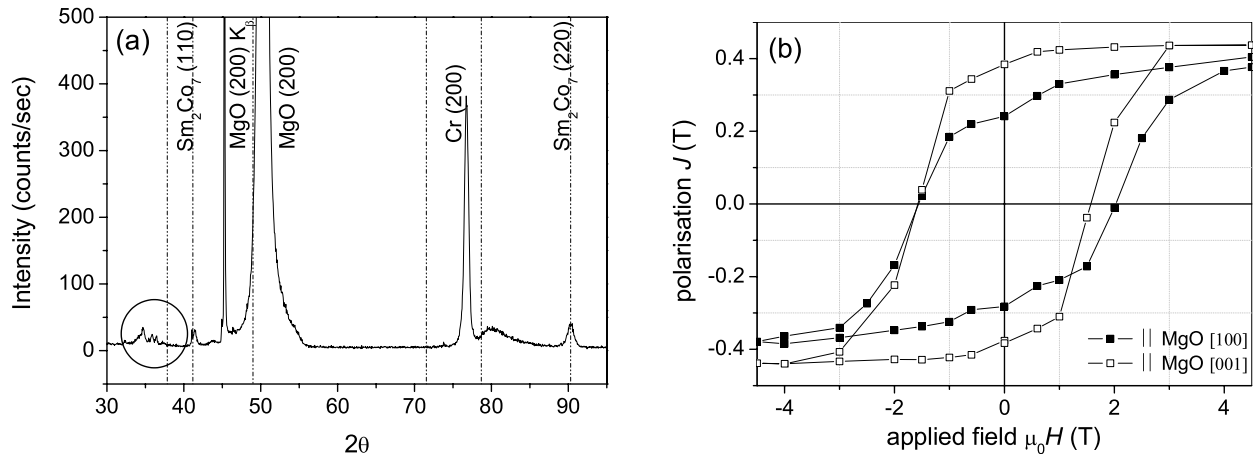


**Fig. 5.2:** (a): XRD of a  $\text{Sm}_2\text{Co}_7$  film deposited at  $750^\circ\text{C}$ .  $(11\bar{2}0)$  out-of-plane textured  $\text{Sm}_2\text{Co}_7$  film on  $(100)$  textured Cr buffer, shows an oxide cluster at  $35^\circ$  corresponding to  $\text{Sm}_2\text{O}_3$ . (b) In-plane hysteresis parallel to  $\text{MgO}[100]$  and out-of-plane magnetic hysteresis parallel to  $\text{MgO}[001]$  of this film indicate nearly isotropic hard magnetic behaviour with  $H_C \sim 2\text{T}$ .

This motivated growth attempts for  $\text{Sm}_2\text{Co}_7$  at lower deposition temperatures. XRD results of a series of  $\text{Sm}_2\text{Co}_7$  films at deposition temperatures of  $650^\circ\text{C}$ ,  $550^\circ\text{C}$  and  $450^\circ\text{C}$  are summarised in Fig. 5.3. Qualitatively, the XRD measurements are similar, showing  $(200)$  Cr reflection,  $(11\bar{2}0)$  and  $(22\bar{4}0)$   $\text{Sm}_2\text{Co}_7$  reflection and  $(200)$  reflections from MgO substrate which are visible up to  $550^\circ\text{C}$ . The increasing intensity of both  $(11\bar{2}0)$  and  $(22\bar{4}0)$   $\text{Sm}_2\text{Co}_7$  reflections with lowering deposition temperature suggests an improving  $\text{Sm}_2\text{Co}_7$  texture, however, at temperatures  $\leq 450^\circ\text{C}$ , only substrate and buffer reflections are seen, and no visible  $\text{Sm}_2\text{Co}_7$  reflections exist, which indicates the absence of sufficient kinetics required for  $\text{Sm}_2\text{Co}_7$  phase formation.

For information on in-plane film orientation, several pole figures were measured on the samples deposited at  $500^\circ\text{C}$ ,  $550^\circ\text{C}$  and  $650^\circ\text{C}$ .  $\text{Sm}_2\text{Co}_7$   $(11\bar{2}6)$  quarter pole figure and calculated pattern are seen in Fig. 5.4 for the sample deposited at  $500^\circ\text{C}$ . Four sharp poles besides some minor reflections of weak intensities are clearly identified in the measured pole figure (Fig. 5.4a). On comparison to calculated pole figure (Fig. 5.4b), the four reflections are branched into two sets of A

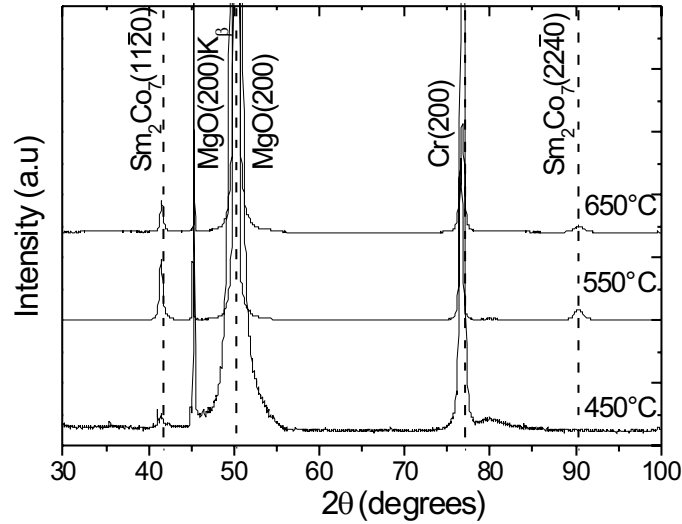


**Fig. 5.3:** XRD of a series of Sm<sub>2</sub>Co<sub>7</sub> films deposited at varying deposition temperatures of 650°C, 550°C, 450°C. On (100) textured Cr, (110) Sm<sub>2</sub>Co<sub>7</sub> reflections are visible, however at 450°C no clear Sm<sub>2</sub>Co<sub>7</sub> phase formation is evident.

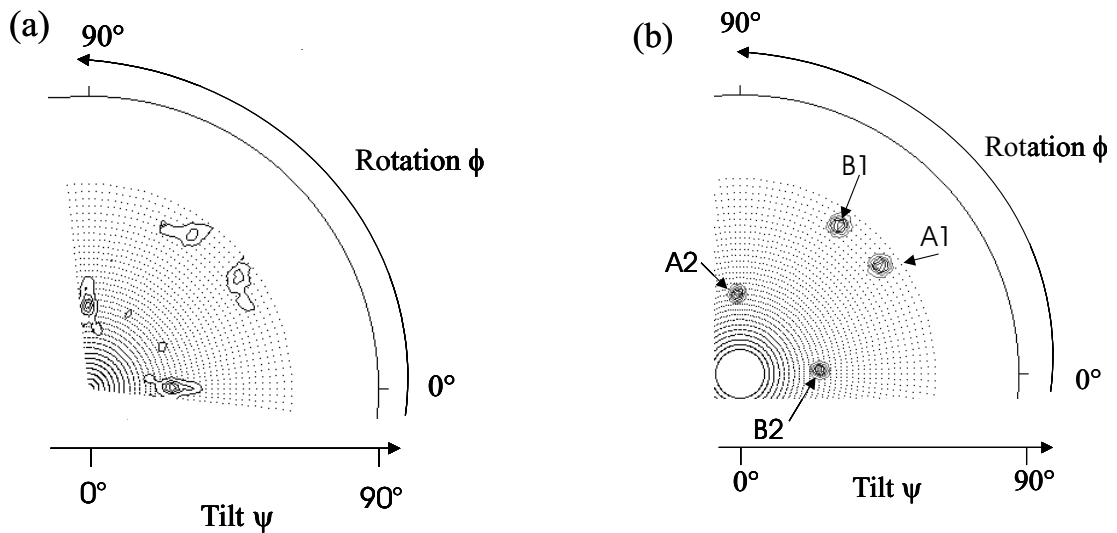


**Fig. 5.4:** (a) Measured (1126) Sm<sub>2</sub>Co<sub>7</sub> pole figure at Sm-Co deposition temperature of 500°C showing four distinct poles. (b). Calculated (1126) pole figures of Sm<sub>2</sub>Co<sub>7</sub> on MgO(100) considering two orientations of Sm<sub>2</sub>Co<sub>7</sub> c-axis, parallel to MgO[100] and the second parallel to MgO[010]. Four distinctly calculated poles match exactly the measured patterns. Courtesy : R. Tamm – TU Dresden.

(A1, A2) and B (B1, B2) reflections. Reflection set A corresponds to Sm<sub>2</sub>Co<sub>7</sub>[0001] || MgO[100] and B indicates Sm<sub>2</sub>Co<sub>7</sub>[0001] || MgO[010] which are ascribed to two equivalent orientations of the Sm<sub>2</sub>Co<sub>7</sub> c-axis lying along two equivalent MgO[100] and MgO[010] directions. Hence, at low deposition temperatures Sm<sub>2</sub>Co<sub>7</sub> grows epitaxially on (100) Cr buffered MgO(100), with complete epitaxial relationships; Sm<sub>2</sub>Co<sub>7</sub>[0001] (1120) || Cr[110] (001) || MgO[100] (001) and its equivalent

$\text{Sm}_2\text{Co}_7[0001] (11\bar{2}0) \parallel \text{Cr}[1\bar{1}0] (001) \parallel \text{MgO}[010] (001)$  due to the twofold symmetry of the Cr buffer. This epitaxial relation was first observed locally by Liu *et al.* in sputter deposited polycrystalline Sm-Co films by means of TEM investigations [Liu96]. The  $\text{Sm}_2\text{Co}_7/\text{Cr}$  epitaxy is understandable due to low lattice mismatch of about 3% between  $\text{Sm}_2\text{Co}_7(0001)$  planes and  $\text{Cr}(011)$  planes. Good lattice matching is achieved when one long  $\text{Sm}_2\text{Co}_7$  unit cell sits on top of six in-plane rotated Cr unit cells such that the c-axis of  $\text{Sm}_2\text{Co}_7$  is parallel to Cr face diagonal.

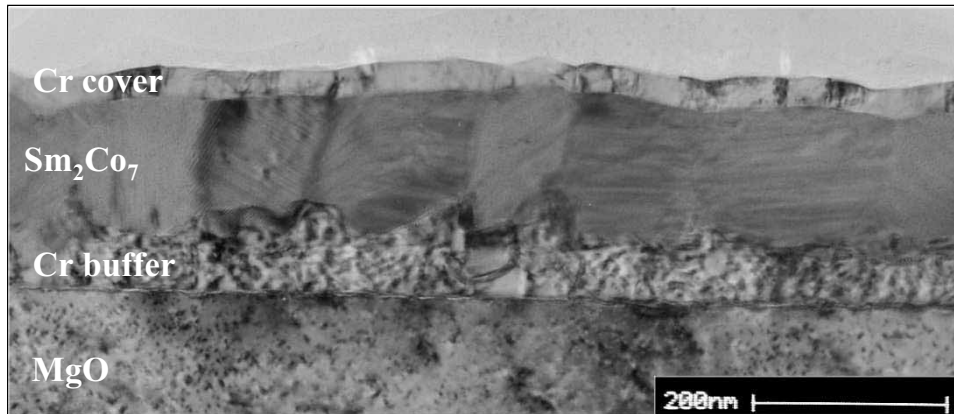


**Fig. 5.5:** TEM overview of  $\text{Sm}_2\text{Co}_7$  sample on Cr buffered  $\text{MgO}(100)$  substrate. Clear interfaces and columnar structure of  $\text{Sm}_2\text{Co}_7$  layer are clearly seen.

Cross-sectional TEM investigations show the overall layer architecture which is well replicated from the attempted layer sequence Cr/SmCo/Cr/MgO (Fig. 5.5). Clean interfaces are seen between MgO substrate, Cr buffer,  $\text{Sm}_2\text{Co}_7$  layer and Cr cover.  $\text{Sm}_2\text{Co}_7$  grows columnar with grains stretching through the entire film thickness of 140 nm and replicating these dimensions laterally in width. Individual layer thicknesses observed in TEM images are very well in agreement with the evaluated thicknesses from EDX-SEM measurements ( $136 \pm 10$  nm for  $\text{Sm}_2\text{Co}_7$  layer and  $53 \pm 5$  nm for Cr).<sup>1</sup>

At higher temperatures ( $\geq 550^\circ\text{C}$ ), besides A and B reflection-pairs in the  $(11\bar{2}6)$  Sm-Co pole figure, two additional sets of reflection C and D are identified (refer Fig. 5.6a). The reflections arise from some of the crystallites in the sample, that have instead of the  $(11\bar{2}0)$  planes,  $(11\bar{2}16)$  planes parallel to the MgO surface. The  $\text{Sm}_2\text{Co}_7 (11\bar{2}0)$  planes are identified in the Bragg-Brentano geometry, but the  $(11\bar{2}16)$  planes have negligible intensity and hence can not be seen in the standard XRD.  $(11\bar{2}16)$  planes parallel to  $\text{MgO}(100)$  correspond to  $60^\circ$  tilt of  $\text{Sm}_2\text{Co}_7$  c-axis. Thus, at these high deposition temperatures, the  $\text{Sm}_2\text{Co}_7$  lattice grows perfectly in-plane and has an additional  $60^\circ$  component tilted out of the film plane, as per pole figure measurements. The additional epitaxial relations at high temperatures are  $\text{Sm}_2\text{Co}_7(11\bar{2}16) \parallel \text{MgO}(001)[100]$  and  $\text{Sm}_2\text{Co}_7(11\bar{2}16) \parallel \text{MgO}(001)[010]$ . These findings stress the importance of pole figure measurements in determining

<sup>1</sup>A big portion of the Cr cover layer seems to be ion milled during sample preparation for cross-sectional TEM.

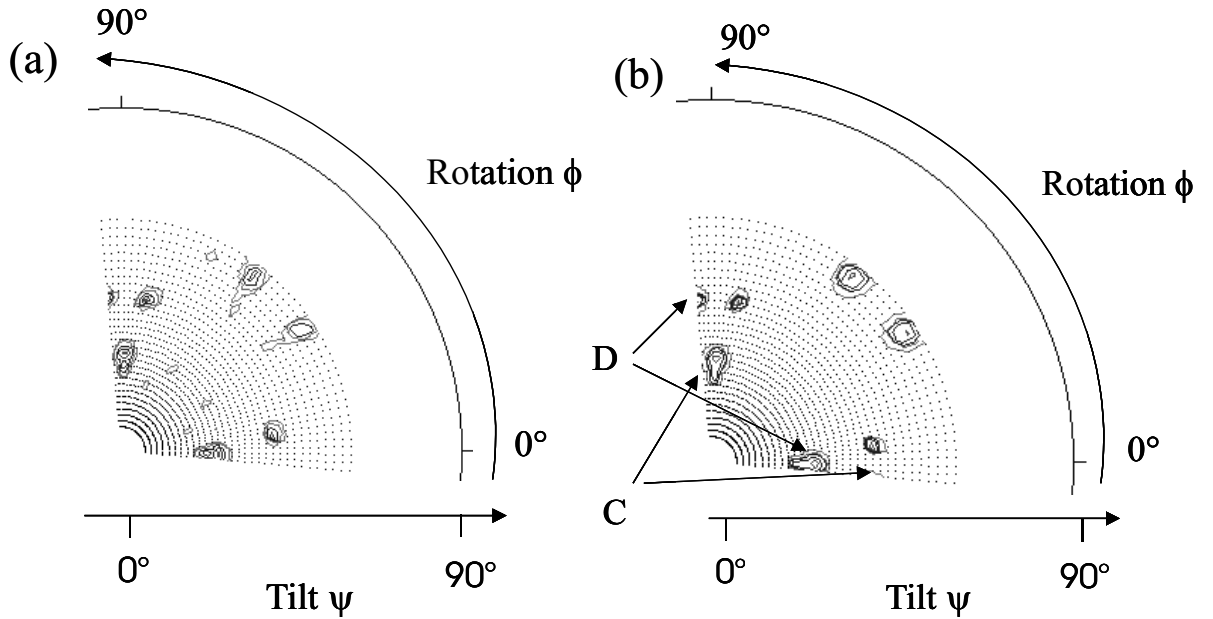


**Fig. 5.6:** (a) Measured  $(11\bar{2}6)$  pole figure of  $\text{Sm}_2\text{Co}_7$  deposited at  $550^\circ\text{C}$ . (b) Calculated  $(11\bar{2}6)$   $\text{Sm}_2\text{Co}_7$  pole figure considering two in-plane  $c$ -axes and two  $60^\circ$  tilted  $c$ -axes components. A group of C and D poles are seen in addition to the already existing A and B poles (Fig. 5.4), which explain the measured pole figure pattern completely. Courtesy: R. Tamm – TU Dresden.

accurate epitaxial relations in samples. Moreover, the tilted  $c$ -axis component has been reported for the first time qualitatively in epitaxial  $\text{Sm}_2\text{Co}_7$  films [Tam05].

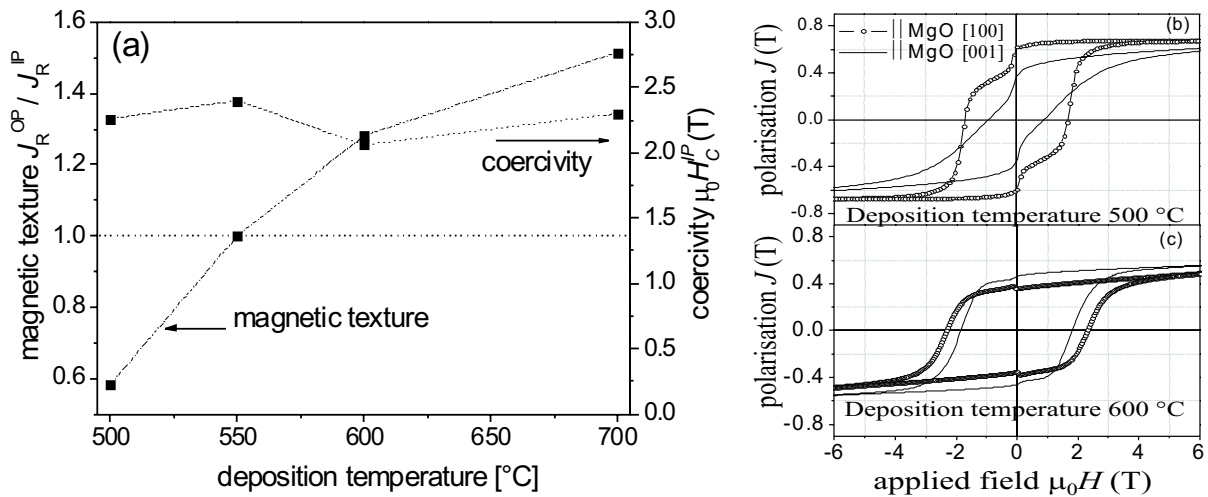


**Fig. 5.7:** (a) Summary of magnetic texture  $J_R^{\text{OP}}/J_R^{\text{IP}}$ , and coercivity  $H_C$ , for film series with 15 Hz repetition rate and varying deposition temperature. (b) & (c) Two exemplary hysteresis loops from the temperature series for films deposited at  $500^\circ\text{C}$  and  $600^\circ\text{C}$  respectively. The magnetic hysteresis is in-plane textured at  $500^\circ\text{C}$  but changes to out-of-plane textured at  $600^\circ\text{C}$ .

Magnetic texture ( $M_{\text{texture}}$ ) and in-plane coercivity ( $\mu_0 H_C$ ) of the samples deposited at varying

deposition temperatures is summarised in Fig. 5.7a. Excellent crystallographic texture with the c-axis lying fully in the film plane results in anisotropic hard magnetic properties in the film plane. Therefore, it is sufficient to consider the variation of only in-plane coercivities parallel to the easy axis, with the deposition temperature. The  $H_C$  stays more-or-less stable at values  $> 2$  T. Variation of  $M_{\text{texture}}$  is more interesting and it changes from  $M_{\text{texture}} > 1$  (from preferred out-of-plane texture) to  $M_{\text{texture}} < 1$  (preferred in-plane texture) as the deposition temperature is lowered. The transition occurs around  $550^\circ\text{C}$ . With decreasing deposition temperature, the out-of-plane hysteresis gets more and more narrow indicating that  $\text{Sm}_2\text{Co}_7$  c-axis is confined more and more in-plane as seen in Fig. 5.7b. This is supported by pole figure measurements, where at high temperatures, a dominant  $60^\circ$  tilted component is identified which disappears in films at lower deposition temperatures (reference Fig. 5.4 and 5.6). The projection of the tilted c-axis is larger in the out-of-plane direction and therefore it enhances the out-of-plane hysteresis. A transition in the crystallographic texture from tilted c-axis to an in-plane texture at temperatures around  $550^\circ\text{C}$  as observed in pole figures is in good agreement with the magnetic findings.

**(b) Repetition rate variation at constant deposition temperature of  $550^\circ\text{C}$**

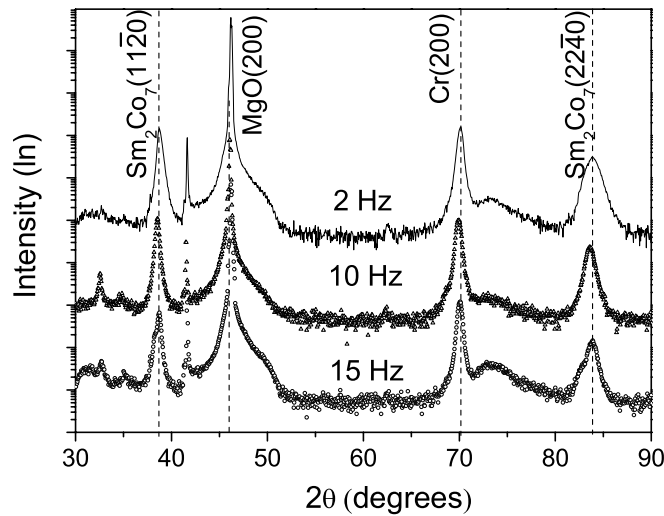


**Fig. 5.8:** XRD of a series of  $\text{Sm}_2\text{Co}_7$  films deposited with different repetition rates of 2 Hz, 10 Hz and 15 Hz on Cr-buffered  $\text{MgO}(100)$ .  $\text{Sm}_2\text{Co}_7$  grows  $(11\bar{2}0)$  textured out-of-plane and the intensity of both  $(11\bar{2}0)$  and  $(22\bar{4}0)$  reflections increases with lowering the repetition rate.

Lowering the deposition temperature improves both crystallographic and magnetic texture, but the best value for magnetic texture obtained so far was 0.6 at  $500^\circ\text{C}$ , which could still improve at further lower deposition temperatures. The growth of  $\text{Sm}_2\text{Co}_7$  phase at deposition temperatures below  $450^\circ\text{C}$  was difficult due to insufficient energy available at these low temperatures for complete  $\text{Sm}_2\text{Co}_7$  phase formation (as seen before in Fig. 5.3). The  $\text{Sm}_2\text{Co}_7$  phase formation at low deposition temperatures can be achieved by reducing the laser repetition rate, since this results in

increased film deposition time. With increased deposition time, the film has longer time available for phase formation and reorientation of its crystallites. A series of samples was deposited with varying laser repetition rates from 15 Hz down to 2 Hz at constant deposition temperature of 550 °C. Conclusive XRD graphs are seen in Fig. 5.8. A clear increase in intensity and peak broadening of both the (11 $\bar{2}$ 0) and (22 $\bar{4}$ 0) Sm<sub>2</sub>Co<sub>7</sub> peaks was observed for visibly constant buffer peak intensity, with lowering of repetition rate from 15 Hz to 10 and up to 2 Hz. The supportive evidence strengthens the belief that phase formation improves along with an increased Sm<sub>2</sub>Co<sub>7</sub> crystallite size with increased time available (or reduced repetition rate) during deposition.

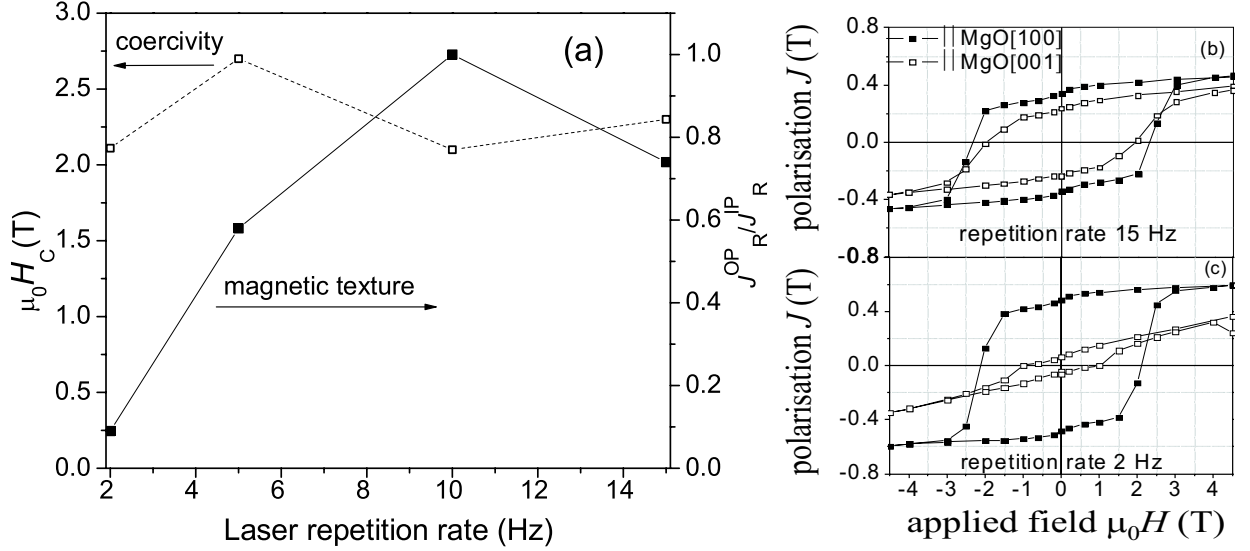


**Fig. 5.9:** (a) Variation of magnetic texture and coercivity for Sm<sub>2</sub>Co<sub>7</sub> films with repetition rate at constant deposition temperature of 550 °C. (b) & (c) Two hystereses from the same series at 15 Hz repetition rate and 2 Hz repetition rate respectively. The out-of-plane loop is significantly narrower at 2 Hz.

The magnetic hysteresis for these films shows a significant improvement in texture with lowering repetition rates. The hysteresis of the film at high repetition rate (15 Hz) shows a remanence of about 0.34 T along the easy axis (Fig. 5.9 b), which is in accordance with the Stoner-Wohlfarth calculations for an isotropic texture ( $J_R = 0.5 J_S$  and  $J_S = 0.8$  T). An isotropic distribution of the easy axis along the in-plane and out-of-plane directions also imparts high coercivity to the film ( $\mu_0 H_C \sim 2.3$  T). On the other hand, the film deposited at low repetition rate (2 Hz), displays a higher remanence of  $J_R = 0.49$  T and a much superior  $M_{\text{texture}}$  of 0.1 (compared to the  $M_{\text{texture}}$  of 0.74 at 15 Hz). The in-plane coercivity  $> 2$  T is maintained. A summary of coercivity and magnetic texture for films with varying repetition rate is shown in Fig. 5.9a. Coercivity is well above 2 T all through the investigated frequency range, clearly indicating that the only property affected by the varying repetition rate is the magnetic texture and the texture changes from predominantly isotropic to perfectly in-plane aligned c-axis, undergoing gradual improvement in between.

## (c) Growth of films at lower deposition temperatures and constant repetition rate of 5 Hz

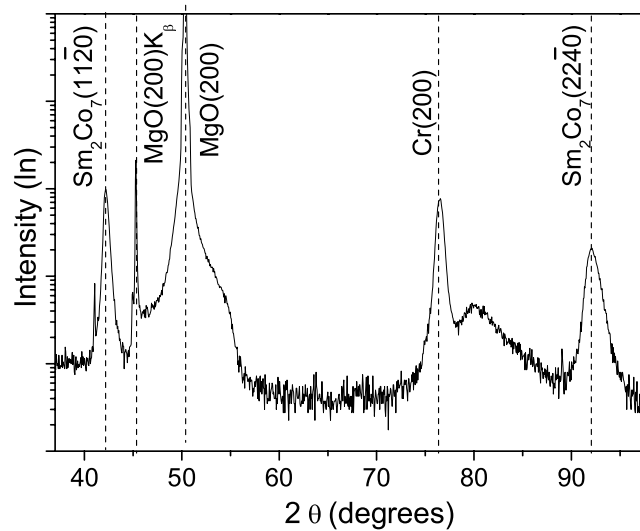


**Fig. 5.10:** XRD on a  $\text{Sm}_2\text{Co}_7$  film prepared at 400 °C with 5 Hz repetition rate. Sharp  $(11\bar{2}0)$  and  $(22\bar{4}0)$   $\text{Sm}_2\text{Co}_7$  peaks indicate that phase formation is possible at temperatures < 450 °C with lowered repetition rate.

To investigate the effect of low repetition rate on the growth and phase formation of  $\text{Sm}_2\text{Co}_7$  films prepared at lower film deposition temperatures and on the magnetic properties of these films, a series of films at lower deposition temperatures (from 600 °C to 350 °C) was prepared at a constant repetition rate of 5 Hz. As expected, phase formation was found to be successful with 5 Hz repetition rate even at 400 °C, which was previously not achievable with 15 Hz repetition rate. This phase formation can be seen directly in XRD in Fig. 5.10 where intense  $(11\bar{2}0)$  and  $(22\bar{4}0)$  peaks of  $\text{Sm}_2\text{Co}_7$  phase are observed on (200) oriented Cr buffer.

Magnetic hysteresis measurements on this series of samples at 5 Hz and varying temperatures from 600 °C to 350 °C have been summarised in Fig. 5.11. The nature of magnetic texture changes from strong out-of-plane at 600 °C to a perfect in-plane texture at 350 °C as seen in figure 5.11a. The film deposited at 350 °C has magnetic texture of 0.02, which suggests an exclusive in-plane texture with magnetic easy axis (c-axis of  $\text{Sm}_2\text{Co}_7$ ) lying only along two equivalent in-plane directions. The coercivity of the samples decreases from more than 2.5 T at 600 °C to less than 1 T at 350 °C. An incomplete phase formation at low temperatures despite lowering the repetition rate causes the weakening of good hard magnetic properties and results in low coercivities in  $\text{Sm}_2\text{Co}_7$  films. Temperatures around 350 °C are on the edge of complete phase formation and even with lowered repetition rate, contain considerable volume fractions of amorphous, non-fully crystallised Sm-Co, which result in low coercivity and a big soft magnetic shoulder in the samples (Fig. 5.11b). This amorphisation of samples at low temperatures was cross checked through FFT (Fast Fourier Transform) on high resolution TEM images. A cross sectional TEM overview image

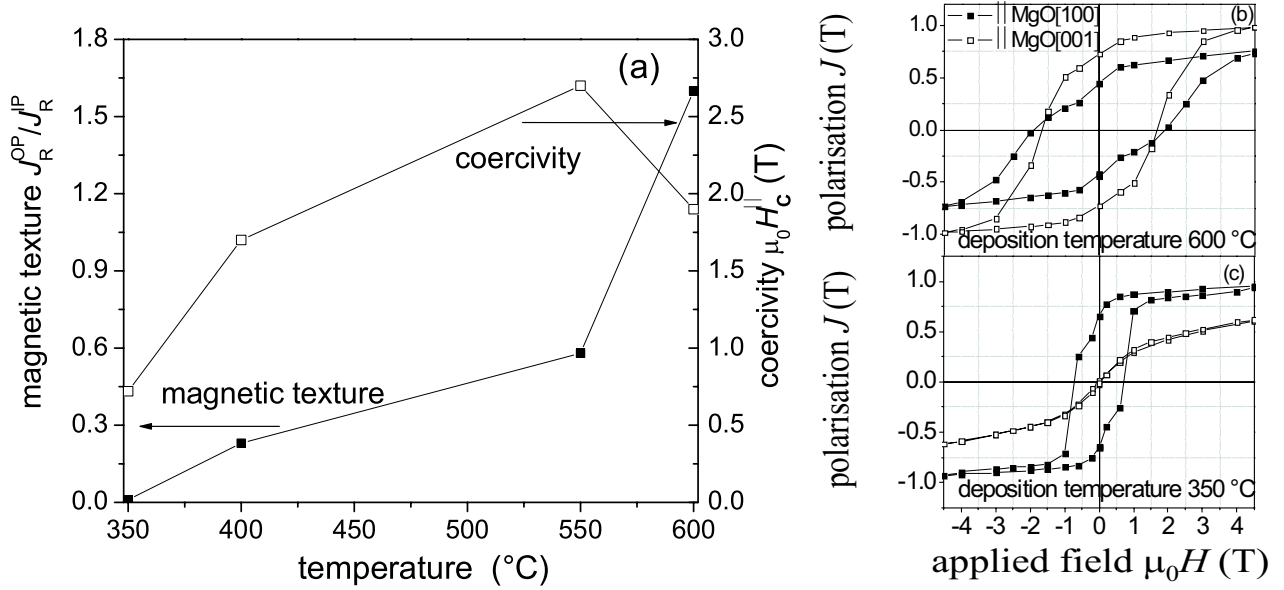


**Fig. 5.11:** (a) Coercivity and magnetic texture are summarised for  $Sm_2Co_7$  extended temperature series deposited with lowered repetition rate of 5 Hz. Magnetic texture improves, at the same time coercivity drops largely with decreasing deposition temperature due to difficulties with phase formation at 350 °C. (b) & (c) Two exemplary hystereses showing improving magnetic texture at lower temperatures, as hypothesised.

seen in Fig. 5.12a separates Sm-Co layer into areas A and B. A high resolution zoom into a region comprising both film areas A and B seen in Fig. 5.12b shows atomic stacking of Sm-Co from area B and fast Fourier transform on this high resolution image shows a hexagonal symmetry implying Sm-Co c-axis lying in the film plane. No long range atomic order is visible in area A and hence no FFT was possible on this area. This confirms that the region A is amorphous and identifies the inverted triangular growth region to be crystalline  $Sm_2Co_7$ .

The epitaxy predicted from pole figure measurements for the  $Sm_2Co_7$  easy-axis lying along two orthogonal MgO in-plane directions is cross-verified with magnetic hysteresis measurements. The measured hysteresis along two non-equivalent in-plane directions, parallel to MgO[100] and parallel to MgO[110] and measured along MgO[001] out-of-plane have been shown in Fig. 5.13a along with the calculated Stoner-Wohlfarth hysteresis in Fig. 5.13b for a similar easy axis distribution and along comparable directions. Stoner-Wohlfarth calculations for this sample where the two easy-axes lie along two equivalent in-plane MgO<100> directions predict a maximum increase in remanent polarisation along MgO[110] in-plane direction (i.e. at 45° to both the easy axes). Since this direction receives magnetisation contributions from both the in-plane easy axes, it has a higher remanent magnetisation (about 70% of the total saturation magnetisation) as compared to either of the easy axes (which only display 50% of the total saturation magnetisation). The increased remanence along 45° in-plane direction is actually observed and is well in accordance with Stoner-Wohlfarth calculations. The Stoner-Wohlfarth model is valid for single domain, non-

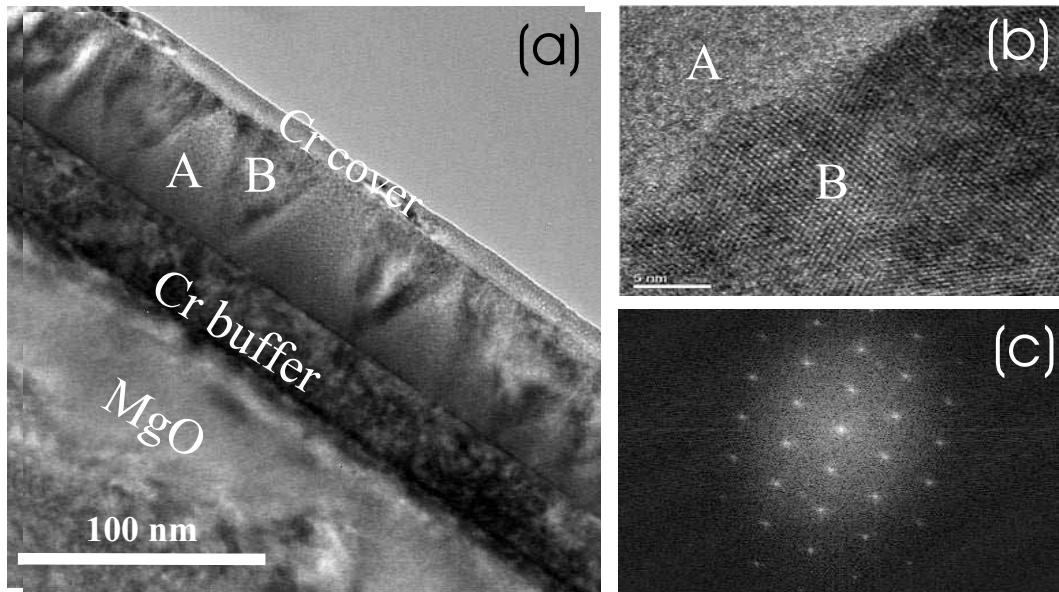


**Fig. 5.12:** (a) TEM overview image of a film deposited at 350 °C and 5 Hz showing layered structure of Sm-Co on Cr on MgO(100). Two clearly different regions A and B are identified. (b) A high resolution zoom into the interface separating region A and B. (c) FFT on high resolution TEM image from region B shows the familiar hexagonal symmetry of Sm-Co confirming that region B is crystalline Sm-Co. No such FFT was obtained from region A indicating its amorphous structure. Courtesy: K. Subba Rao – TU Dresden.

interacting particles and since in the remanent state all the magnetisation lies along the easy axis, the use of this model for predicting remanences is justified. However, magnetisation reversal in real magnet systems is affected by defects, inter-grain interactions etc. and, therefore, this simple model is unable to accurately predict coercivities. A detailed analysis of factors determining the coercivity in hard magnets will be discussed in Chapter 6.

#### (d) Summary and discussion of Sm<sub>2</sub>Co<sub>7</sub> films on MgO(100) substrates

Sm<sub>2</sub>Co<sub>7</sub> films were deposited on Cr buffered MgO(100) single crystal substrates. The XRD measurements confirm that the Cr buffer is (200) oriented out-of-plane and the Sm<sub>2</sub>Co<sub>7</sub> layer is (11 $\bar{2}$ 0) oriented. However, pole figure measurements indicate the c-axis of Sm<sub>2</sub>Co<sub>7</sub> to have a fourfold in-plane symmetry in addition to a second fourfold c-axis texture where the c-axis is tilted 60° out-of-plane. The tilted c-axis texture makes a large contribution to the out-of-plane hysteresis, resulting in an out-of-plane to in-plane remanence ratio (measure of magnetic texture) larger than 1 at high deposition temperatures. The unwanted tilted c-axis texture was found to decrease with decreasing deposition temperature. However, Sm<sub>2</sub>Co<sub>7</sub> phase formation could not be achieved at deposition temperatures below 550 °C at which point the magnetic texture ratio of 0.5 was still not perfect.

The laser repetition rate (pulse frequency) was lowered from 15 Hz to 5 Hz with the aim of pro-

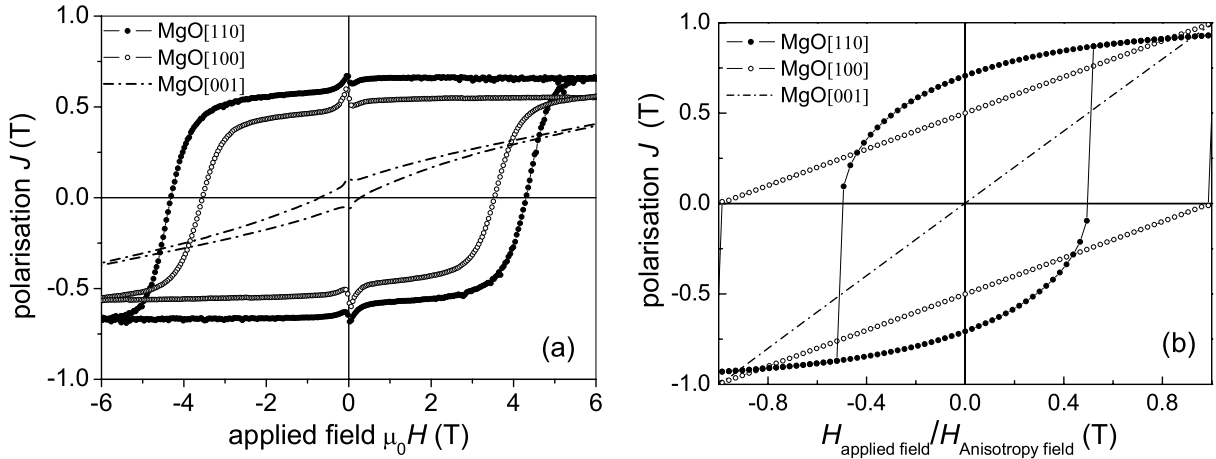


**Fig. 5.13:** (a) Hysteresis loops for an epitaxial  $\text{Sm}_2\text{Co}_7$  film prepared at 400 °C and 5 Hz measured along three independent substrate directions. (b) Stoner-Wohlfarth hysteresis calculations along three similar directions considering two orthogonal in-plane easy axes lying parallel to  $\text{MgO}[100]$  and  $\text{MgO}[010]$ .

viding more time to the Sm-Co layer to form the phase at low deposition temperatures ( $< 550$  °C). The phase formation of the  $\text{Sm}_2\text{Co}_7$  layer was found to improve with reduced repetition rate from pole figure measurements. The same was also observed in a reduced out-of-plane hysteresis and therefore an improved magnetic texture. Excellent  $\text{Sm}_2\text{Co}_7$  films were deposited at a temperature of 400 °C (which were accessible with reduced laser repetition rate) with very narrow out-of-plane hysteresis, a magnetic texture of 0.02 and in-plane coercivities of more than 2 T.

### 5.1.2 Growth of $\text{SmCo}_5$ Phase

The  $\text{SmCo}_5$  phase is more interesting for scientific investigations due to its high saturation polarisation of 1.14 T [Bus98] and high  $T_C$  of 720 K. However, in spite of its superior hard magnetic properties, epitaxial growth of this phase had not been reported so far. Epitaxial growth of the pure  $\text{SmCo}_5$  phase on Cr-buffered  $\text{MgO}(100)$  single crystal substrates was attempted in this work. The deposition parameters used for the  $\text{SmCo}_5$  layer were 400 °C deposition temperature and 5 Hz laser repetition rate to promote good crystallographic and magnetic texture. Phase purity was verified by XRD, pole figure and TEM investigations.

#### (a) XRD results on $\text{SmCo}_5$ films

As was shown in the section before, Cr grows epitaxially on  $\text{MgO}(100)$  with two equivalent orientations as per  $\text{Cr}(001)[110] \parallel \text{MgO}(001)[100]$  and  $\text{Cr}(001)[1\bar{1}0] \parallel \text{MgO}(001)[010]$ . Sm-Co with  $16 \pm 0.5$  at.% Sm corresponding to the  $\text{SmCo}_5$  phase (refer section 4.2 for composition and thickness determination) was deposited on epitaxial Cr buffer. X-ray diffraction pattern for the

film is shown in 5.14 along with dashed lines indicating the theoretical peak positions of the strong  $\text{SmCo}_5$  reflections. Only two clear peaks, the  $(11\bar{2}0)$  and the  $(22\bar{4}0)$  of the  $\text{SmCo}_5$  phase are observed on  $\text{Cr}(100) \parallel \text{MgO}(100)$ . That suggests only one distinct out-of-plane orientation of the  $\text{SmCo}_5$  phase in the sample at these low deposition temperatures and low laser repetition rates.

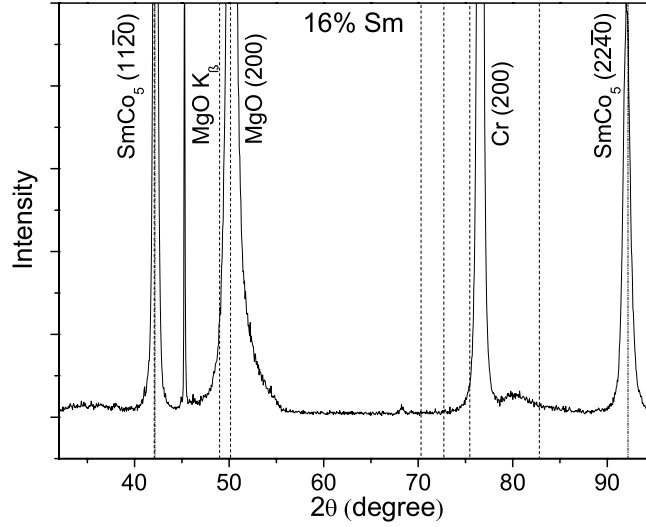


**Fig. 5.14:** Measured XRD pattern for a  $\text{SmCo}_5$  film with dotted lines indicating high intensity reflections of the  $\text{SmCo}_5$  phase from an X-ray powder diffraction database. Only  $(11\bar{2}0)$  and  $(22\bar{4}0)$  reflections of the  $\text{SmCo}_5$  phase are visible, besides the  $(200)$  Cr reflection and the  $(200)$  reflection of the MgO substrate.

### (b) Pole Figure Measurements

Experimentally measured  $(11\bar{2}0)$  and  $(11\bar{2}1)$  pole figures are seen in Fig. 5.15. Sharp and distinct Sm-Co poles were measured. The measured pole figures match the calculated pole figures pattern (not shown here) for  $\text{SmCo}_5$  phase assuming two definite c-axes orientations aligned with  $\text{Cr}[110] \parallel \text{MgO}[100]$  and  $\text{Cr}[1\bar{1}0] \parallel \text{MgO}[010]$ . This confirms clear twofold epitaxy in the sample as per the epitaxial relation;  $\text{SmCo}_5[0001](11\bar{2}0) \parallel \text{Cr}[110](001) \parallel \text{MgO}[100](001)$  and  $\text{SmCo}_5[0001](11\bar{2}0) \parallel \text{Cr}[1\bar{1}0](001) \parallel \text{MgO}[010](001)$ . The  $3^\circ$  FWHM (Full Width at Half Maxima) of the  $(11\bar{2}0)$  poles in  $\psi$  and  $4.8^\circ$  in  $\phi$  additionally prove sharp  $\text{SmCo}_5$  texture. Moreover, as was observed before in the case of  $\text{Sm}_2\text{Co}_7$  thin films no indication of  $60^\circ$  tilted c-axis component is observed from the pole figures at these low Sm-Co deposition temperatures.

Measured Sm-Co pole figures were also used to identify the exact phase.  $(10\bar{1}7)$ ,  $(11\bar{2}0)$ ,  $(11\bar{2}1)$  and  $(0002)$  pole figures were measured at experimentally optimised  $2\theta$  positions in the sample. Comparison between the measured  $2\theta$  values in the sample and theoretically predicted  $2\theta$  values for  $\text{SmCo}_5$  and  $\text{Sm}_2\text{Co}_7$  phase (which is the most likely phase mixture) is seen in Tab. 5.1. The optimised sample  $2\theta$  positions for three of the four different poles were closer to the theoretical  $2\theta$  pole positions for the  $\text{SmCo}_5$  phase compared to the  $\text{Sm}_2\text{Co}_7$  phase. The strongest indication

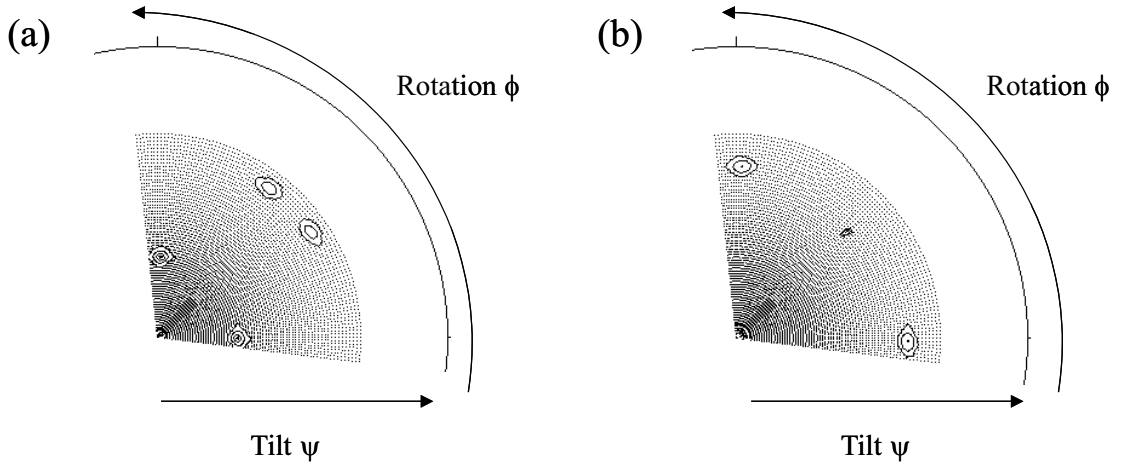


**Fig. 5.15:** (a)  $(11\bar{2}1)$   $\text{SmCo}_5$  pole figure measured at experimentally determined  $2\theta$  pole positions. (b)  $(11\bar{2}0)$   $\text{SmCo}_5$  measured pole figure. Pole figures, besides clarifying the texture, are used for  $\text{SmCo}_5$  phase identification. Courtesy: R. Tamm – TU Dresden.

**Table 5.1:** Experimentally measured  $2\theta$  values of some poles in the sample and theoretical  $2\theta$  values of the same poles in  $\text{SmCo}_5$  and  $\text{Sm}_2\text{Co}_7$ .

$\text{SmCo}_5$ reflections	$\text{Sm}_2\text{Co}_7$ reflections	$2\theta_{\text{exp}}$	$2\theta_{\text{theo}}(\text{SmCo}_5)$	$2\theta_{\text{theo}}(\text{Sm}_2\text{Co}_7)$
$(10\bar{1}1)$	$(10\bar{1}6)$	$30.5^\circ$	$30.4^\circ$	$30.06^\circ$
$(11\bar{2}0)$	$(11\bar{2}0)$	$36.2^\circ$	$35.9^\circ$	$35.5^\circ$
$(11\bar{2}1)$	$(11\bar{2}6)$	$42.1^\circ$	$42.1^\circ$	$42.6^\circ$
Absent	$(10\bar{1}7)$	Absent	Absent	$33.1^\circ$

comes from the absence of the  $(10\bar{1}7)$  reflection in the sample, which is forbidden for the  $\text{SmCo}_5$  phase, but exists in the  $\text{Sm}_2\text{Co}_7$  phase and, therefore, must appear if the sample were a phase mixture containing  $\text{SmCo}_5$  and  $\text{Sm}_2\text{Co}_7$  phases.

**(c) TEM investigations** TEM investigations performed on this sample show the layered architecture of Cr/Sm-Co/Cr/ MgO (not shown here). In high resolution images, the distinct atomic stacking of the Sm-Co layer becomes visible. Figure 5.16 shows a high resolution TEM image of this  $\text{SmCo}_5$  film where atomic rows in two distinct grains, well separated by a grain boundary, can be identified.

Fast Fourier Transform (FFT) on these high resolution electron images of the two individual

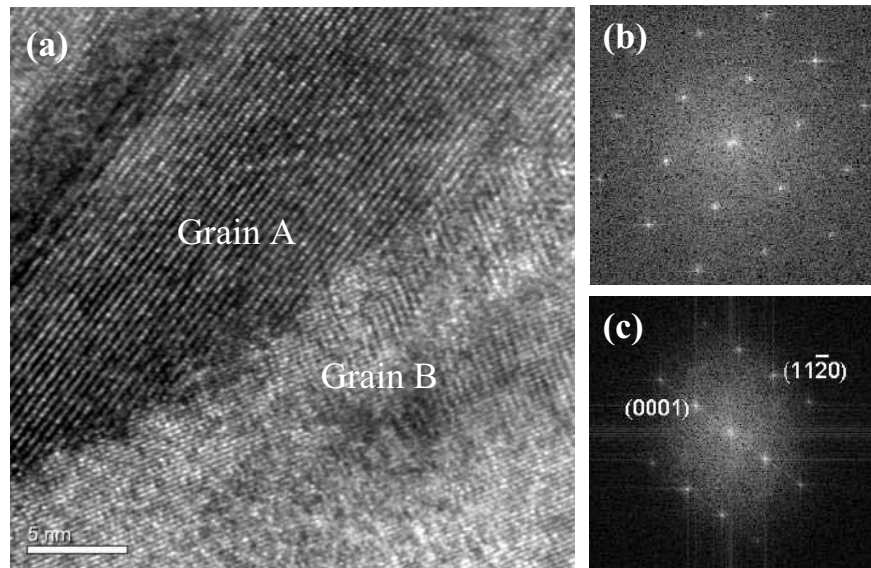


**Fig. 5.16:** (a) High resolution TEM images of two grains separated by a grain boundary. (b) FFT on grain A showing the typical, expected hexagon of Sm-Co lying in-plane. (c) FFT from the second grain B. Sm-Co directions are indexed and this indicates the second Sm-Co orientation in-plane. Both the FFTs together confirm the two orthogonal in-plane orientations of SmCo<sub>5</sub> c-axis.

grains can be seen in Fig. 5.16b and c. In Fig. 5.16b, the hexagonal symmetry of Sm-Co can be identified and indicates a Sm-Co grain that lies with its c-axis pointing in the plane of this paper. The FFT on the second grain can be seen in Fig. 5.16c and the orientation of the c-axis of this grain is again indexed in the FFT pattern. Hence, two orthogonal c-axis orientations are seen in the electron diffraction patterns that lie in the film plane and the well known epitaxial relation between the substrate, Cr buffer and SmCo<sub>5</sub> phase is seen again. Moreover, only one set of lattice constants calculated for the Sm-Co layer from several grains supports the fact that only the pure SmCo<sub>5</sub> phase exists in the film area investigated by TEM.

#### (d) Magnetic Investigations

Magnetic hystereses of the SmCo<sub>5</sub> film measured along three substrate directions are shown in Fig. 5.17a. The very narrow and flat out-of-plane hysteresis is in agreement with a good in-plane texture of the SmCo<sub>5</sub> film where the c-axis is confined mainly in-plane. The in-plane hystereses were measured along two in-plane directions, along MgO[100] which is parallel to one of the easy axes and second in-plane along MgO[110], which is the direction 45° to both the in-plane c-axes. The hystereses along both the directions are rectangular and broad, additionally a high coercivity of 2.4 T along MgO[110] was recorded. A remanent polarisation of 0.73 along MgO[110] correlates well with the polarisation calculations from the Stoner-Wohlfarth model along MgO[110] ( $J_R = 0.71 J_S$ , as explained earlier) in a system where the easy axis lies along two equivalent MgO directions namely MgO[100] and MgO[010] in the film plane. This remanence value is 38% higher for the SmCo<sub>5</sub> phase compared to the Sm<sub>2</sub>Co<sub>7</sub> phase.

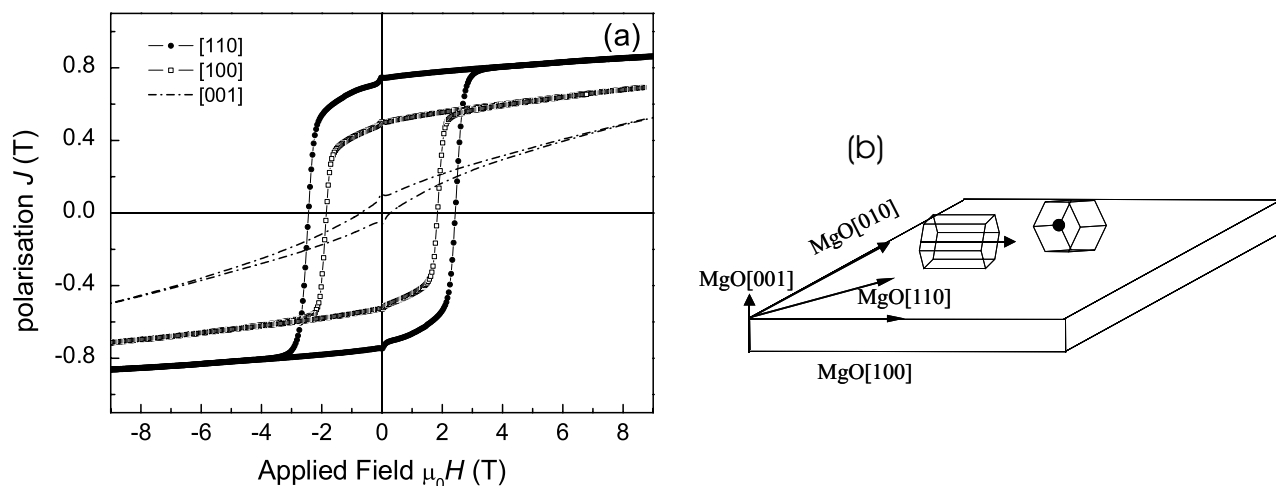


**Fig. 5.17:** (a) Magnetic hysteresis of a  $\text{SmCo}_5$  film measured along three non-equivalent  $\text{MgO}$  directions. Remanent polarisation of 0.73 T along  $\text{MgO}[110]$  shows an increment of almost 40% over achievable remanence in  $\text{Sm}_2\text{Co}_7$  phase. (b) Schematic of  $\text{MgO}(100)$  substrate showing the main directions along which magnetic hystereses have been measured.

### (e) Summary and Discussion of $\text{SmCo}_5$ films on $\text{MgO}(100)$ substrates

The  $\text{SmCo}_5$  films of 16 at.% Sm were deposited on  $\text{MgO}(100)$  single crystal substrates under optimised deposition conditions of low laser repetition rate (5 Hz) and low deposition temperature ( $400^\circ\text{C}$ ). The phase purity was checked with XRD and several pole figure measurements. The measured  $2\theta$  positions for different poles were closer to the  $\text{SmCo}_5$  phase than the  $\text{Sm}_2\text{Co}_7$  phase. Moreover, the complete absence of the  $(10\bar{1}7)$  reflection clearly suggests the dominant phase in the film to be  $\text{SmCo}_5$ . The magnetic hysteresis measurements along  $\text{MgO}[100]$  and along  $\text{MgO}[110]$  in-plane directions show the twin c-axis texture in the film plane. The higher remanence of 0.71 T measured along  $\text{MgO}[110]$  substrate direction is very well in accordance with the maximum expected remanence ( $= 0.7 J_S$ ) for the given texture. The high coercivity of more than 2 T was reproducibly achieved.

### 5.1.3 Stoichiometric Variation of Co Content

Just as the high anisotropy of  $R-T$  compounds is provided by the rare-earth element, the transition metal is responsible for the high magnetisation in the system. Increasing the transition metal content is therefore often correlated with an increased magnetisation and is desirable until the hard magnetic properties deteriorate due to the diminished rare-earth contribution. The variation of film stoichiometry was investigated from 14–23 at.% Sm in epitaxial Sm-Co films.

X-ray diffraction on a series of samples, each prepared with different Co amount, can be seen in Fig. 5.18a. All samples show the characteristic  $(11\bar{2}0)$  Sm-Co reflections on Cr buffered  $\text{MgO}(100)$

substrates. Noticeable is the increase in the  $2\theta$  value of the Sm-Co ( $11\bar{2}0$ ) peak from  $41.5^\circ$  to  $42.22^\circ$  along with a similar shift in the ( $22\bar{4}0$ ) peak position with increasing Sm content. The shift

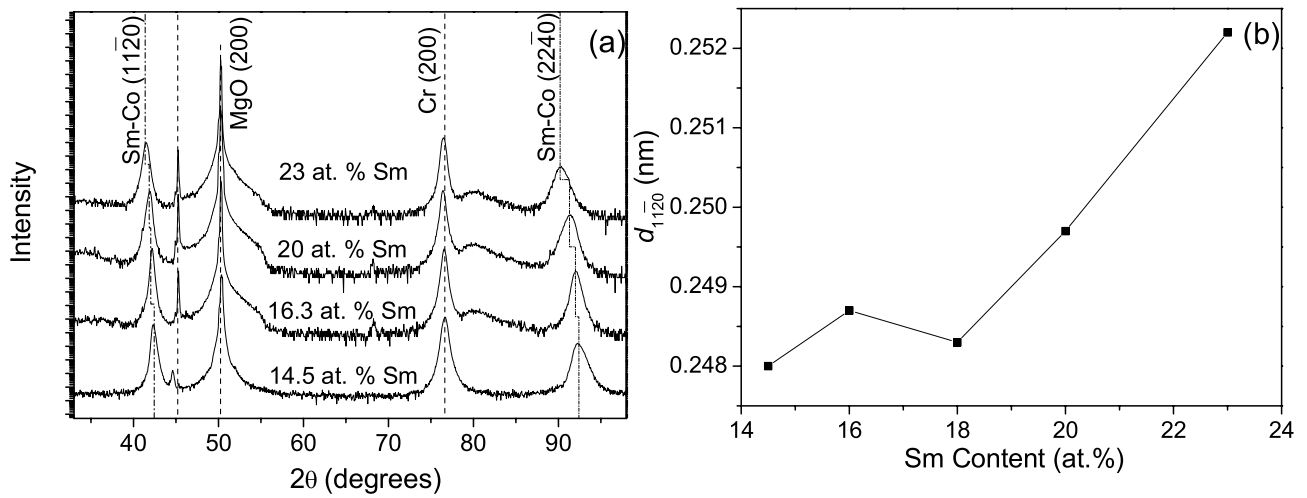


**Fig. 5.18:** (a). XRD patterns for Sm-Co film on MgO(100) substrates. ( $11\bar{2}0$ ) and ( $22\bar{4}0$ ) reflections of SmCo shift to higher  $2\theta$  values with decreasing Sm content in the samples. (b). Summary of  $d$  spacing of the ( $11\bar{2}0$ ) Sm-Co reflection indicating a clear increase in Sm-Co unit cell dimension with increasing Sm content in accordance with results from crystal diffraction database.

in peak position to lower  $2\theta$  values with increasing Sm content indicates an increasing Sm-Co lattice, which is also in qualitative agreement with the known unit cell structures and dimensions. A summary of variation in ( $11\bar{2}0$ )  $d$ -spacing with Sm content is presented in Fig. 5.18b. The ( $11\bar{2}0$ )  $d$ -spacing for the film with 23 at.% Sm compares well with the theoretical value for  $\text{Sm}_2\text{Co}_7$  phase as does the value for the 16 at.% Sm film with  $\text{SmCo}_5$  phase. Films with lower Sm at.% come close to resembling the  $\text{SmCo}_7$  phase. Since most of these phases are crystallographically related, the distinction between formation of distorted crystal cells or an intimate phase mixture resulting in an averaged  $d$ -spacing, is not possible without extensive TEM work.

The magnetic properties of these films are summarised in Fig. 5.19. The polarisation values measured at a maximum applied field of 4.5 T ("saturation polarisation") change from a value close to 0.8 T to 0.27 T upon increasing the Sm content by almost 10 at.% (Fig. 5.19a). Following the same trend, the remanent polarisation drops from 0.7 T to 0.2 T as expected. However, the samples considered are not saturated at applied fields of the order of 4.5 T, due to the high anisotropy of the Sm-Co phases and, therefore, when measured in higher fields the so-called saturation polarisation should increase as well. The decreasing trend, however, justifies that the main contribution to magnetic moment of the Sm-Co system is from the transition metal element. High coercivities in the range of 1.5-2 T were consistently obtained on all films independent of the Sm content (Fig. 5.19b). At the same time, the magnetic texture lies low at around 0.1 throughout the series, suggesting good crystallographic in-plane texture. Two exemplary hystereses are shown in

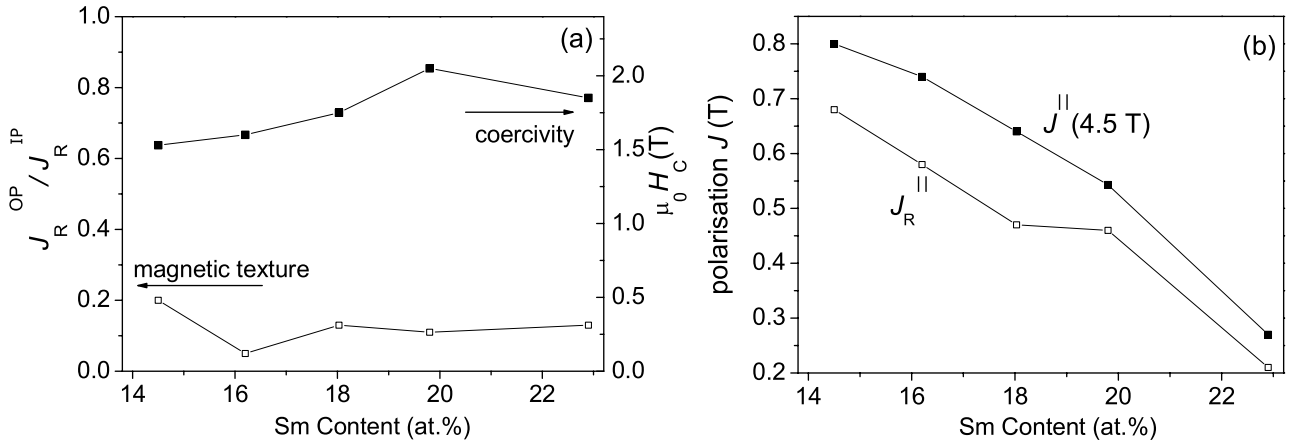


**Fig. 5.19:** (a). Variation of magnetic texture and coercivity of Sm-Co films on MgO(100) with varying Sm content. (b). Decreasing trends of polarisation at 4.5 T ("saturation polarisation") and remanent polarisation of Sm-Co samples with increasing Sm content.

Fig. 5.20. A strong increase in polarisation for a film with reduced Sm content (16 at.%) compared to the film with higher Sm content (23 at.%) is observed. Well maintained crystallographic texture, which directly reflects in strong magnetic texture, is also clearly visible.

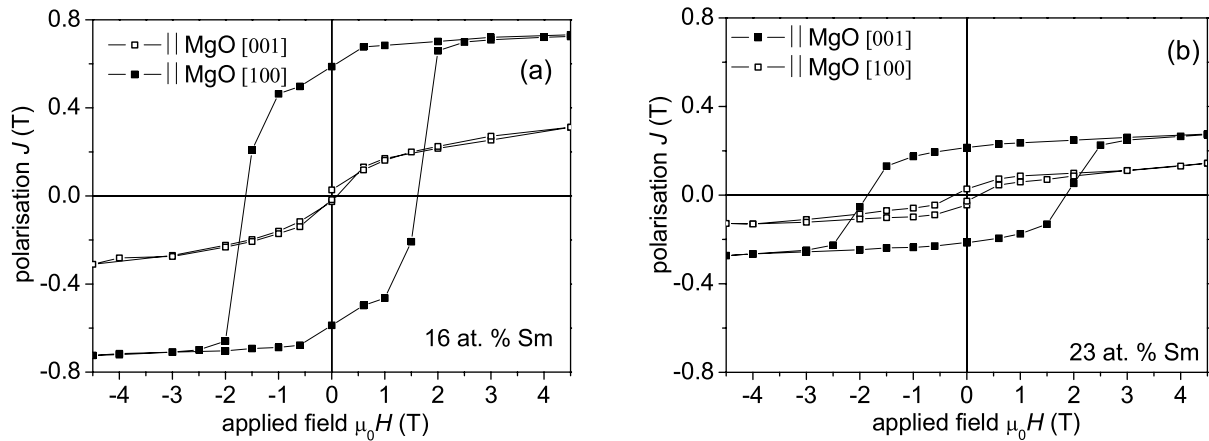


**Fig. 5.20:** Two exemplary hystereses of Sm-Co films from the composition series with 16 at.% Sm and 23 at.% Sm. A higher remanent polarisation is observed for the film with 16 at.% Sm (image a) compared to film with 23 at.% Sm (image b) along with perfect in-plane magnetic texture.

## 5.2 SmCo<sub>5</sub> Films on MgO(110) Single Crystal Substrates

MgO(110) single crystal substrates with lower surface symmetry compared to MgO(100) single crystal substrates offer a possibility for uni-axial growth of Sm-Co. The two orthogonal in-plane directions in MgO(110), viz [110] and [001], are non-equivalent directions. The layer architecture

of Cr/SmCo<sub>5</sub>/Cr/MgO(110) similar to the one on MgO(100) single crystal substrates was maintained. The results and brief explanations follow up in the next two subsections.

### 5.2.1 Analysis and Optimisation of Cr Buffer

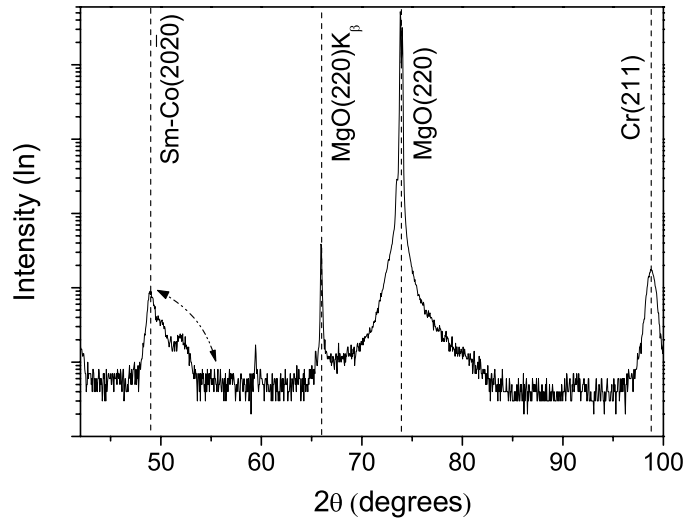


**Fig. 5.21:** Measured XRD patterns of SmCo<sub>5</sub> film on MgO(110) single crystal substrate. (211) Cr and (20 $\bar{2}$ 0) SmCo<sub>5</sub> reflections are seen along with an unidentified set of reflections marked with an arrow.

X-ray diffraction of a SmCo<sub>5</sub> film on Cr buffered MgO(110) substrate is seen in Fig. 5.21. The film was prepared with the previously optimised deposition conditions for the Cr buffer and Sm-Co on MgO(100) single crystal substrates, namely 700 °C deposition temperature and 15 Hz laser repetition rate for the Cr buffer and 400 °C deposition temperature and 5 Hz laser repetition rate for the SmCo<sub>5</sub> layer. The details of the optimised deposition conditions may also be cross-referred from Tab. 4.1. The (220) substrate peak and (211) Cr buffer reflection are clearly visible in the XRD pattern. Thus, the Cr buffer is (211) oriented out-of-plane. Furthermore, the (20 $\bar{2}$ 0) SmCo<sub>5</sub> reflection is also present, which implies that the Sm-Co c-axis lies in the film plane and, hence, corresponds to the desired texture component. However, along with the (20 $\bar{2}$ 0) SmCo<sub>5</sub> reflection, a group of other reflections that appears as a broad shoulder to the (20 $\bar{2}$ 0) reflection is also visible (marked with an arrow). These additional reflections can be attributed to a number of Sm-Co phases or even to another orientation of the SmCo<sub>5</sub> phase. Varying the deposition temperature or the laser repetition rate for the Sm-Co layer did not lead to an improvement or vanishing of the unidentified reflections. A (110) Cr pole figure is shown in Fig. 5.22a. Two equivalent (211) orientations of Cr produce two sets of (110) poles in pole figure measurements marked as A and B. A1, A2, A3 set of (110) poles corresponds to the orientation Cr(211)[0 $\bar{1}$ 1] || MgO(110)[001] and the set B1, B2, B3 corresponds to Cr(211)[ $\bar{1}$ 11] || MgO(1 $\bar{1}$ 0)[001]. FWHM of less than 3° in

$\phi$  confirms good in-plane texture for the buffer deposited at 700 °C. However,  $(11\bar{2}0)$  pole figure measurements for  $\text{SmCo}_5$  seen in Fig. 5.22b contain several stray peaks B and weak intensities for the desired identifiable poles A. All measurements only confirm that a perfect epitaxy leading to uniaxial c-axis textured  $\text{SmCo}_5$  is not yet achieved.

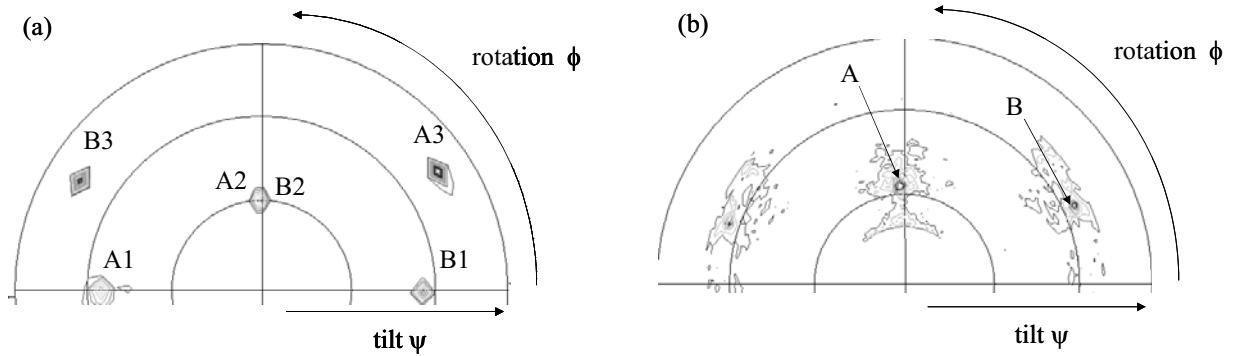


**Fig. 5.22:** (a)  $(110)$  Cr pole figure for  $\text{Cr}(211)/\text{MgO}(110)$ . Two sets of poles A1, A2, A3 and B1, B2, B3 are seen in the  $(110)$  Cr pole figure, which refer to two Cr (211) orientations. Poles A2 and B2 from the two orientations overlap. (b) Measured  $(11\bar{2}0)$   $\text{SmCo}_5$  pole figure. Besides the  $(11\bar{2}0)$  pole marked as A, unidentified pole sets B are also seen.

A series of Cr buffers with 15 Hz laser repetition rate prepared at varying deposition temperatures was investigated extensively with AFM, pole figure measurements and TEM. AFM micrographs of Cr buffer prepared at deposition temperatures of 700 °C and 300 °C are seen in Fig. 5.23. Along with surface images, lateral line scans across the buffer surface are seen. The Cr buffer prepared at low deposition temperature (Fig. 5.23a) is very smooth and the buffer morphology is similar to a high temperature Cr buffer on  $\text{MgO}(100)$  substrate (seen in Fig. 5.1). Line scan measured across the scanned area, gives a peak-to-valley height of 3–5 nm, which is much smaller compared to the buffer thickness of 40–50 nm. Thus, the buffer can be assumed to be continuous. Low rms roughness of around 0.2 nm measured for the scanned area of  $2\ \mu\text{m} \times 2\ \mu\text{m}$  testifies the buffer smoothness. On the contrary, a high-temperature Cr buffer is rather rough and shows a granular growth, with deposited areas well separated by deep trenches as seen in Fig. 5.23b. The buffer surface is intolerably rough with rms roughness values up to 5 nm. Similar line scan across the scanned surface gives peak-to-valley height differences of 40–50 nm, which is the same as the buffer thickness. Variation of rms roughness values with deposition temperature for this set of Cr buffers is summarised in Fig. 5.24a.

FWHM values of the  $(110)$  Cr pole are presented in Fig. 5.24b. A high degree of out-of-plane texture with a  $\text{FWHM} < 2^\circ$  and sharp in-plane texture having  $\text{FWHM} \sim 4^\circ$  is maintained by Cr all through the investigated temperature range. Only for deposition at 200 °C does the FWHM in the out-of-plane direction increase largely. The two equivalent (211) Cr orientations at these low temperatures split to give non-overlapping A2-B2 poles in  $(110)$  Cr pole figure (Fig. 5.22).

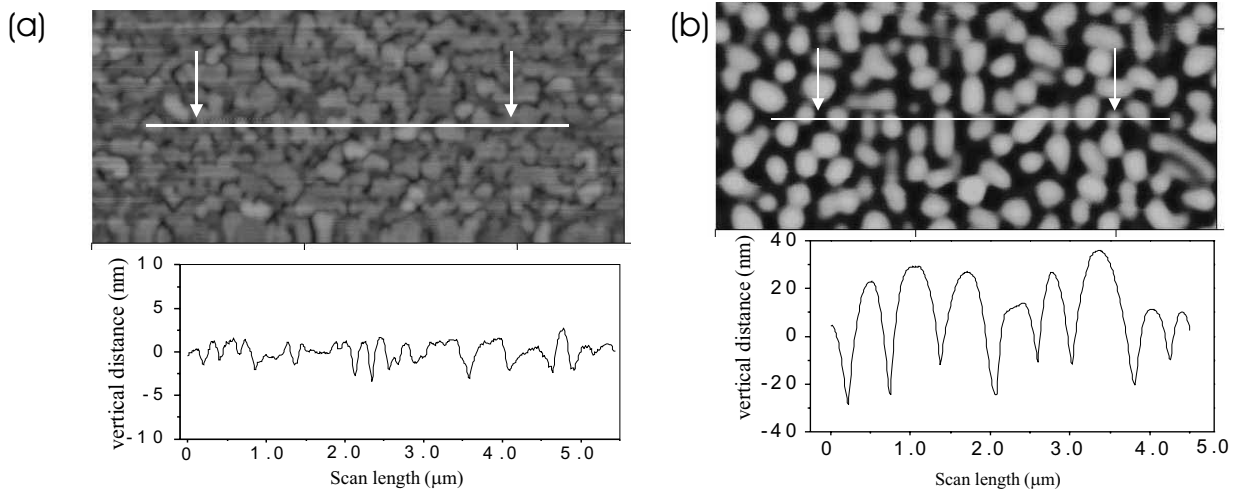


**Fig. 5.23:** (a) AFM micrograph of a Cr film deposited at 300 °C showing smooth and continuous buffer morphology. (b) AFM micrograph of Cr film deposited at 700 °C indicating island growth in Cr at high deposition temperature. Surface line scans performed on these AFM images laterally, for the two samples are seen under the micrographs respectively.

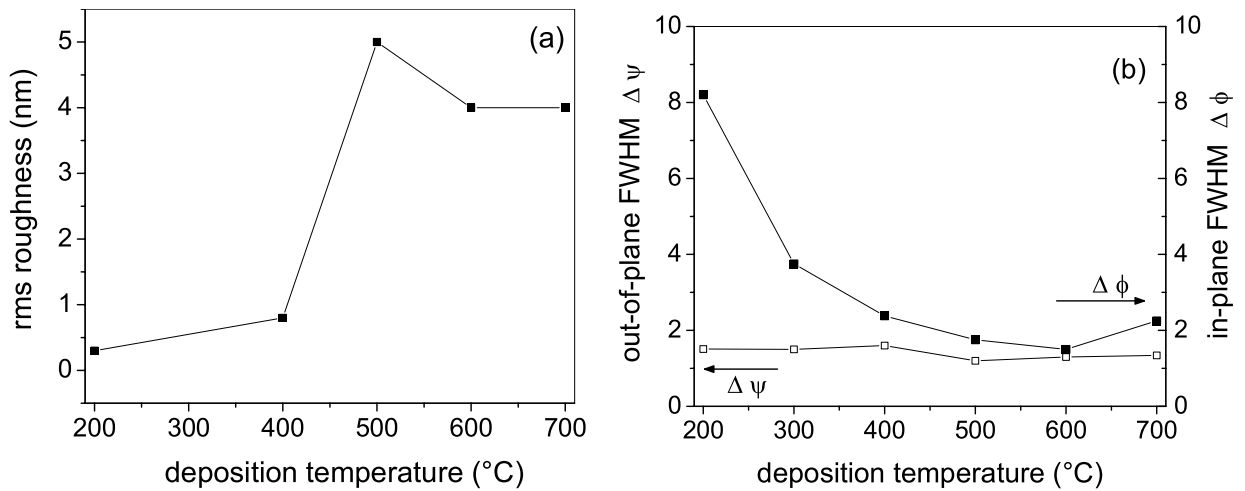


**Fig. 5.24:** (a) RMS roughness of a Cr films prepared at different deposition temperatures, calculated from AFM. (b) In-plane and out-of-plane texture spread quantified by the FWHM ( $\Delta\phi$  and  $\Delta\psi$ ) of the (110) Cr poles from the (110) Cr pole figure.

Therefore, although the two independent textures are sharp, the overall pole-width increases. Both, texture and roughness of the Cr buffer were found to be appropriate at an intermediate range of deposition temperatures (around 500 °C) and, therefore, in the following SmCo<sub>5</sub> films were deposited on Cr buffers prepared at 500 °C.

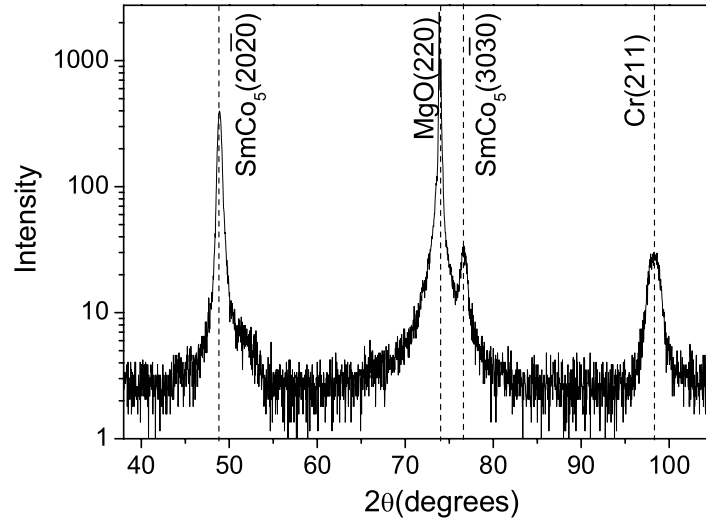


**Fig. 5.25:** (20 $\bar{2}$ 0) and (30 $\bar{3}$ 0) XRD reflections of a SmCo<sub>5</sub> film on Cr(211)/MgO(110). The Cr buffer is deposited at 500°C.

### 5.2.2 Epitaxial SmCo<sub>5</sub> Films on Improved Cr Buffer

SmCo<sub>5</sub> films on smooth, continuous Cr buffers were deposited at low deposition temperature of 500°C. As seen from x-ray diffraction of a SmCo<sub>5</sub> film on a low-temperature Cr buffer in Fig. 5.25, two identifiable SmCo<sub>5</sub> reflections, (20 $\bar{2}$ 0) and (30 $\bar{3}$ 0), besides the (220) substrate reflection and (211) buffer peak are seen. No additional unknown peaks from the SmCo<sub>5</sub> phase were observed. The SmCo<sub>5</sub> (20 $\bar{2}$ 0) reflection pointing out-of-plane suggests that the SmCo<sub>5</sub> c-axis lies in the film plane.

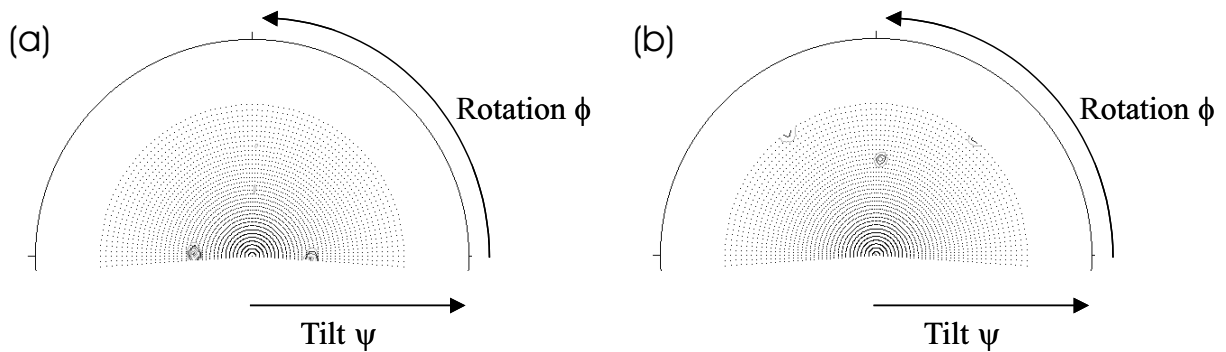


**Fig. 5.26:** Measured (10 $\bar{1}$ 1) and (11 $\bar{2}$ 0) SmCo<sub>5</sub> pole figures (image a and b respectively). Distinct poles propose epitaxy in the system.

Pole figure measurements were necessary to confirm epitaxy in the system. (10 $\bar{1}$ 1), (11 $\bar{2}$ 0), (11 $\bar{2}$ 1) and (20 $\bar{2}$ 0) SmCo<sub>5</sub> pole figures were measured and are seen in Fig. 5.26, in comparison with the calculated patterns in Fig. 5.27. Half pole figures were sufficient for measurement because of the twofold symmetry of the substrate. Good agreement is seen between the measured and the

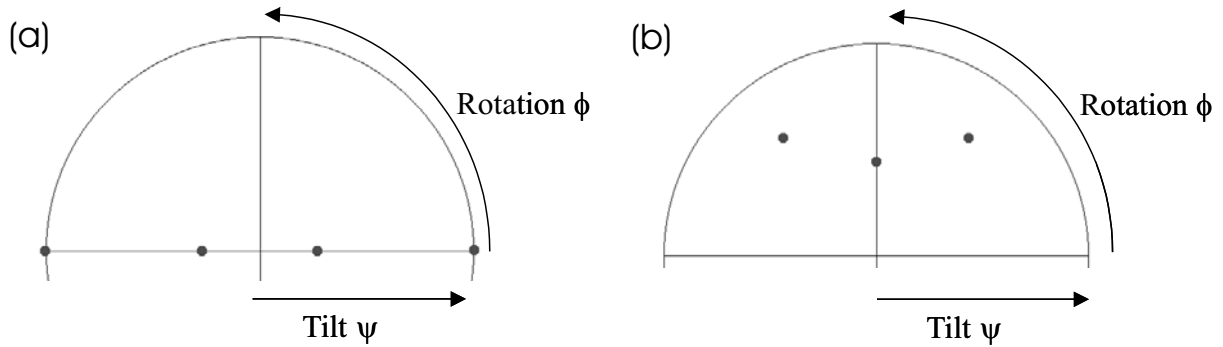


**Fig. 5.27:** Calculated  $(10\bar{1}1)$  and  $(11\bar{2}0)$   $\text{SmCo}_5$  pole figures (a and b respectively) for a uniaxial  $\text{SmCo}_5$  texture on  $\text{MgO}(110)$  substrates. The calculated patterns match with the measured pole figures perfectly as seen in Fig. 5.26. Courtesy: R. Tamm – TU Dresden.

calculated pole positions, directly indicating sharp  $\text{SmCo}_5/\text{Cr}$  epitaxy. This means that the  $\text{SmCo}_5$  c-axis  $[0001]$  lies in-plane parallel to  $\text{Cr}[0\bar{1}1]$  and  $\text{MgO}[001]$  as before in the case of  $\text{MgO}(100)$  single crystal substrates. The complete epitaxial relation valid for these  $\text{SmCo}_5$  films on  $\text{MgO}(110)$  substrates is  $\text{SmCo}_5 (10\bar{1}0)[0001] \parallel \text{Cr} (211)[0\bar{1}1] \parallel \text{MgO}(110)[001]$ , which defines a unique direction for the  $\text{SmCo}_5$  c-axis to fall parallel to  $\text{MgO}[001]$ , see Fig. 5.28b.

Magnetic measurements on these epitaxial  $\text{SmCo}_5$  films on  $\text{MgO}(110)$  substrates were performed along three orthogonal directions of the substrate, viz parallel to  $\text{MgO}[001]$  and parallel to  $\text{MgO}[110]$  in-plane and parallel to  $\text{MgO}[\bar{1}10]$  out of plane. Large, square shaped hysteresis was obtained only along  $\text{MgO}[001]$  in-plane (Fig. 5.28a). Coercivities of 3.1 T were achieved along the easy axis with remanence as high as 0.94 T. Negligible hystereses were measured out of the film plane and parallel to  $\text{MgO}[110]$  in-plane. The magnetic texture nicely compliments the good crystallographic texture.  $M_{\text{texture}} = 0.08$  suggests a very strong uni-axial magnetic in-plane texture in these films and makes them very attractive for further detailed investigations on magnetic microstructure in  $\text{SmCo}_5$  thin films (To follow up in the next chapter).

### 5.3 $\text{Sm}_2\text{Co}_7$ Films on IBAD $\text{MgO}(100)$ Buffered a-Si Substrates

The growth of  $\text{Sm}_2\text{Co}_7$  was also investigated in detail on  $\text{MgO}(100)$  buffered amorphous SiN / Si (a-Si) substrates. A 15 nm thick  $\text{MgO}$  layer was deposited with Ion-Beam Assisted PLD (IBAD-PLD)<sup>2</sup>. A 400-eV Ar ion beam is directed towards the substrate at an incidence angle of  $55^\circ$  to the substrate normal. The direction of the ion beam hampers the growth of all unwanted orientations of  $\text{MgO}$  during PLD and only one required orientation survives  $[\text{Hüh}01]$ . The  $\text{MgO}$  layer is oriented

<sup>2</sup>All IBAD- $\text{MgO}$  samples for this work were provided by Dr. R. Hühne.

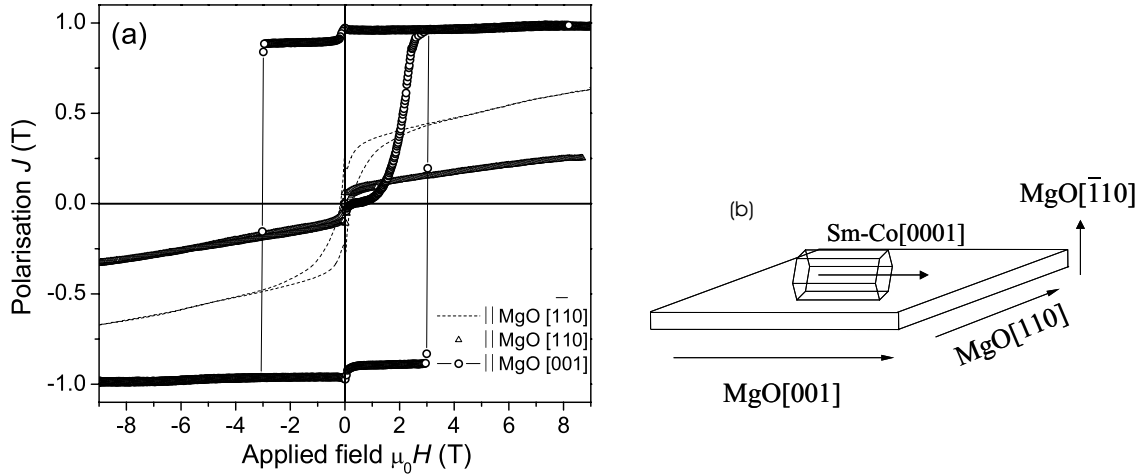


**Fig. 5.28:** (a) Magnetic hystereses of a  $\text{SmCo}_5$  sample on  $\text{MgO}(110)$  single crystal substrate measured along three orthogonal substrate directions. (b) Sketch of the main measurement directions.

with the [100] direction parallel to the ion beam. These technical IBAD-MgO(100) buffered a-Si substrates were used in comparison to single crystal MgO(100) substrates for investigating Sm-Co texture. the further layer architecture of Cr/Sm-Co/Cr was maintained.

The XRD pattern of a  $\text{Sm}_2\text{Co}_7$  film on IBAD-MgO(100) substrate seen in Fig. 5.29 is qualitatively similar to the XRD pattern of Sm-Co films on MgO(100) single crystal substrates (refer to XRD in Fig. 5.10). Strong Si substrate (100) peaks are seen along with (200) MgO reflection, (200) Cr buffer reflection and a weaker (110) Cr reflection, identified to be arising from the Cr cover layer, which is cold deposited. The  $\text{Sm}_2\text{Co}_7$  layer shows clear  $(11\bar{2}0)$  and  $(22\bar{4}0)$  reflection peaks. The estimated crystallite size using the Scherrer formula<sup>3</sup> for IBAD-MgO(100) is found to be 11 nm, which is very close to 15 nm of intended film thickness. This suggests that the MgO(100) crystallites are spanning the entire layer thickness and grow columnar.

The (220) MgO pole figure in Fig. 5.30a indicates a cube texture in IBAD-MgO, with a FWHM of approx.  $12^\circ$ . The biaxially growing MgO is rotated by approx.  $35^\circ$  with respect to the Si[100] edge. The  $(11\bar{2}6)$   $\text{Sm}_2\text{Co}_7$  pole figure shows four poles as expected for two orthogonal in-plane c-axes texture of  $\text{Sm}_2\text{Co}_7$  on MgO(100) (compare with  $(11\bar{2}6)$   $\text{Sm}_2\text{Co}_7$  pole figure in Fig. 5.4). The pole patterns are as expected but the whole pole figure is rotated by  $35^\circ$  in  $\phi$ , suggesting an in-plane rotation of  $35^\circ$  of  $\text{Sm}_2\text{Co}_7[0001]$  with respect to Si[100]. Since MgO grows  $35^\circ$  rotated in-plane due to the  $55^\circ$  Ar ion beam incidence, the c-axis of  $\text{Sm}_2\text{Co}_7$  easily adopts this  $35^\circ$  in-

<sup>3</sup>

$$\text{Crystallite size} = \frac{0.9\lambda}{B \cos \theta} \quad (5.2)$$

The equation is called the Scherrer Formula and can be used to evaluate the size of coherently scattering regions in materials based on FWHM of the peaks (B). However, since stresses in thin films can cause peak broadening in addition to varying crystallite sizes, the results for crystallite sizes may not always be accurate.

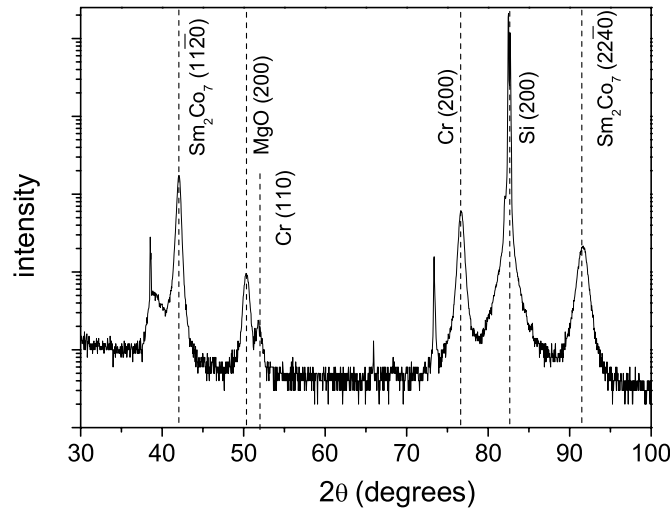


**Fig. 5.29:** XRD pattern of a  $\text{Sm}_2\text{Co}_7$  film on MgO-buffered Si(100) substrate. The MgO(200) peak along with Cr(200) and  $(11\bar{2}0)$  and  $(22\bar{4}0)$   $\text{Sm}_2\text{Co}_7$  reflections are observed.

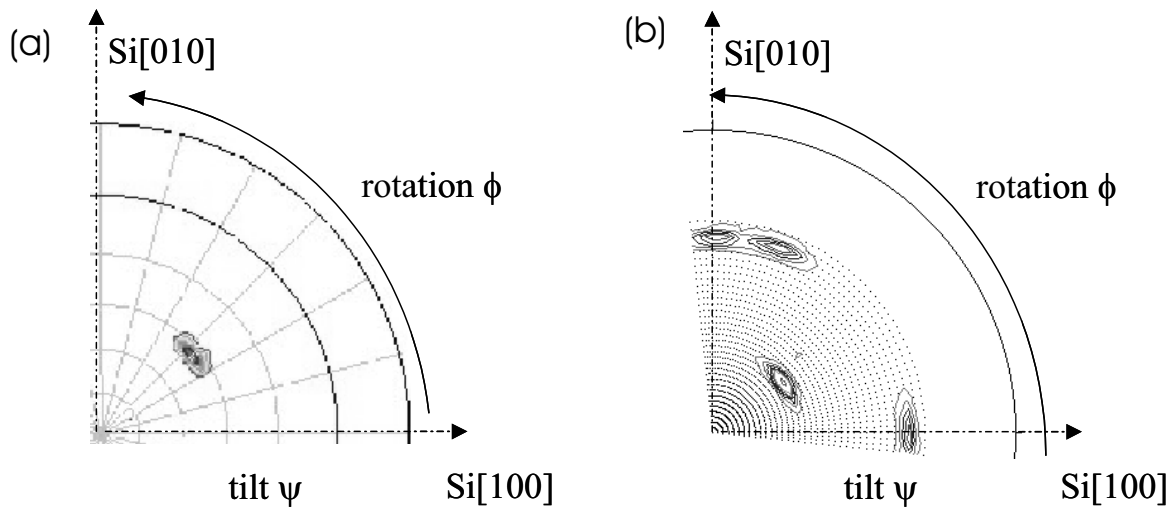


**Fig. 5.30:** (a) MgO(110) quarter pole figure showing one pole that is rotated  $36^\circ$  with respect to the Si[100] direction. This shows that MgO grows with a rotated cube texture on Si(100). (b)  $(11\bar{2}6)$   $\text{Sm}_2\text{Co}_7$  pole figure indicating an epitaxially growing  $\text{Sm}_2\text{Co}_7$  on (100)MgO-buffered Si(100).

plane rotation and continues to grow epitaxially on this rotated MgO. Thus, the epitaxial relation of  $\text{Sm}_2\text{Co}_7$  on Cr/MgO(100)/a-Si remains qualitatively the same as on MgO(100) single crystals, with two orthogonal  $\text{Sm}_2\text{Co}_7$  c-axes in the film plane. The poles are distinctly visible and the FWHM of the  $(11\bar{2}6)$  poles is more than  $12^\circ$  in the in-plane direction (Fig. 5.30a). This texture is understandably inferior to the  $\text{Sm}_2\text{Co}_7$  texture on single crystal substrates but comparable to the IBAD-MgO texture on a-Si substrates.

Microstructural studies were made on fractured cross-sectional samples with HR-SEM. Individual interfaces between buffer and  $\text{Sm}_2\text{Co}_7$  and between  $\text{Sm}_2\text{Co}_7$  and the Cr cover layer (marked as

interface 1 and interface 2) are observable in Fig. 5.31. However, due to the very small thickness of the IBAD MgO layer (15 nm) and limited resolution of SEM, this layer can not be seen clearly. Still, the observations suggest a columnar structure for the  $\text{Sm}_2\text{Co}_7$  layer as was seen on single crystal MgO(100) substrates in TEM. Moreover, the estimated film thickness of individual layers from HR-SEM images are again very well in agreement with thickness results determined from EDX-SEM investigations. Although very informative, HR-SEM is still unable to resolve the fine grain sizes of the  $\text{Sm}_2\text{Co}_7$  and Cr layers (which are obtainable from TEM).

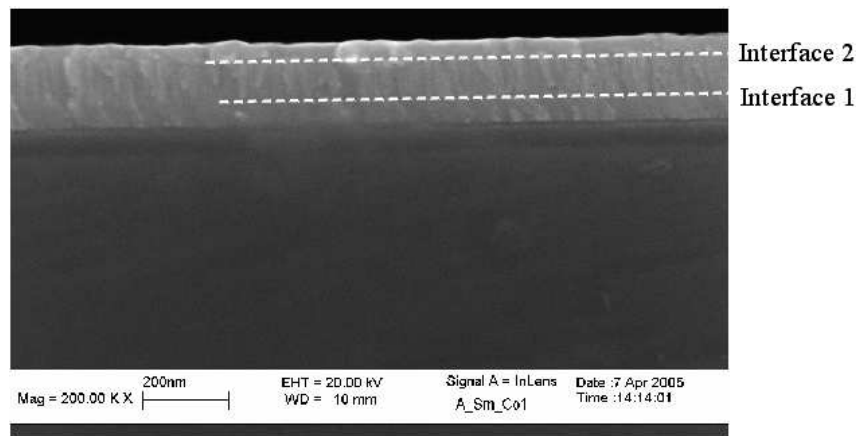


**Fig. 5.31:** HRSEM on IBAD MgO(100), weakly showing the layer architecture and individual layer thicknesses.

Magnetic properties of  $\text{Sm}_2\text{Co}_7$  are directly influenced by the crystallographic texture. Measurement of magnetic hysteresis along Si[100] and [001] shows good magnetic texture quality as seen in Fig. 5.32. Very high coercivities of about 3.6 T are measured parallel to Si[100]. The measured coercivities along this direction are approx. 30% higher than along comparable directions on single crystal substrates. The square-shaped hysteresis with sharp switching behaviour further supports a fully in-plane aligned c-axis. The higher coercivities can be understood in terms of smaller grain sizes of the  $\text{Sm}_2\text{Co}_7$  phase. In the following chapter, it will be shown that the basic magnetisation reversal is dominated by a pinning process. In this context, the increased number of grain boundaries and, hence, the increased density of pinning sites will cause magnetisation reversal to occur at higher fields. A high remanent polarisation ( $J_R$ ) of 0.8 T is measured along the Si[100], which is higher than the expected value of 0.7 T for the given c-axis distribution. An analysis of this increased remanence will be presented in the next chapter, along with other detailed magnetic measurements. Out-of-plane hystereses that are perfectly flat, resembling ideal hard-axis loops, are measured along the Si[001] direction and can be seen in Fig. 5.32.

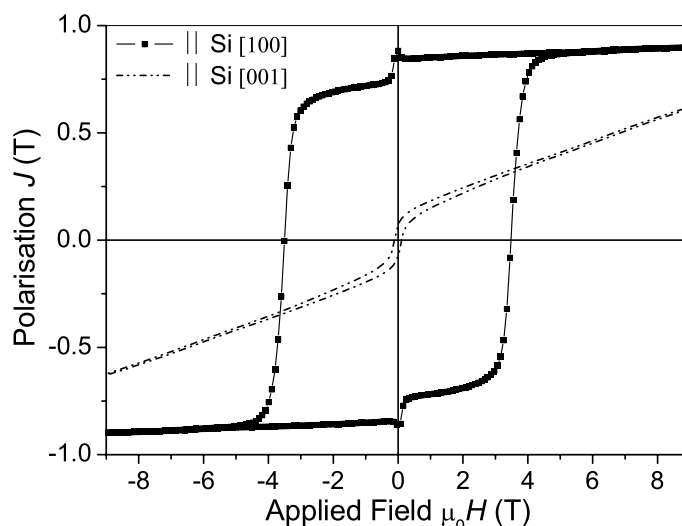


**Fig. 5.32:** Magnetic hystereses of  $\text{Sm}_2\text{Co}_7$  film measured up to 9 T along in-plane direction parallel to  $\text{Si}[100]$  and out-of-plane parallel to  $\text{Si}[001]$ . Very high coercivity of 3.6 T along in-plane direction and excellent magnetic texture are obtained.

## 5.4 Summary and Discussion of Epitaxially Prepared Sm-Co Films

Thin Sm-Co films were prepared epitaxially on Cr buffered MgO single crystal substrates and on MgO buffered amorphous SiN/Si substrates (a-Si). The role of substrate orientation and substrate texture in deciding the epitaxial growth and, therefore, the crystallographic and magnetic texture of Sm-Co films has been investigated.

On MgO(100) single crystal substrates at low deposition temperatures ( $\sim 400^\circ\text{C}$ ) and with low pulse repetition rate (5 Hz), perfectly epitaxial Sm-Co thin films can be prepared. Pole figure measurements prove the epitaxial relation;  $\text{Sm}_2\text{Co}_7[0001] (11\bar{2}0) \parallel \text{Cr}[110] (001) \parallel \text{MgO}[100] (001)$  and  $\text{Sm}_2\text{Co}_7[0001] (11\bar{2}0) \parallel \text{Cr}[1\bar{1}0] (001) \parallel \text{MgO}[010] (001)$  (refer Fig. 5.4). From this epitaxial relation it is clear that the Cr buffer grows  $45^\circ$  rotated in the film plane and has a fourfold surface symmetry on top of the MgO substrate. The Sm-Co layer adopts this symmetry of the buffer and, therefore, also grows with the same fourfold symmetry. This means that Sm-Co films prepared on MgO(100) single crystal substrates have two equivalent orientations of the magnetic easy axis (c-axis), which lie parallel to the substrate edges namely, parallel to MgO[100] and the second easy axis parallel to MgO[010]. This epitaxial relation is verified by magnetic measurements along three independent substrate directions. The magnetic hysteresis parallel to MgO[100] results in a large square-shaped hysteresis with a coercivity of more than 2 T. Hysteresis measurements parallel to MgO[110] in-plane direction (at  $45^\circ$  to the two easy axes) results in an increased hysteresis with a

higher remanence which is in accordance with the calculations of the Stoner-Wohlfarth model as is seen in Fig. 5.13.

The effect of changing the Sm content in the films on the epitaxial growth and magnetic properties was investigated in a composition range from 14.5 at.% Sm to 23 at.% Sm on MgO(100) single crystal substrates. Over the entire composition range, epitaxial growth of Sm-Co was observed. Furthermore, a steady shift in the d-spacing of the (11 $\bar{2}$ 0) Sm-Co reflection, which was well in accordance with the powder diffraction data, suggested a likewise change in Sm-Co lattice and structure with composition (refer Fig. 5.18). From the magnetic measurements, the ratio of out-of-plane remanence to in-plane remanence remained low around 0.1. This suggests a good magnetic texture all through the investigated composition range. Moreover, the remanent and the saturation magnetisation of the films showed a monotonic increase with increasing Co content or decreasing Sm content, as expected. However, the absolute values of saturation magnetisation were lower than the expected values for these phases, which was because these high anisotropic Sm-Co films could not be fully saturated in low applied fields of about 4.5 T (refer Fig. 5.19)

Sm-Co films were also deposited on MgO(100) buffered a-Si substrates. Thin MgO(100) (20 nm thick) layer was deposited with ion beam assisted deposition on a-Si substrates (courtesy - Dr. R. Hühne). MgO(100) grows cube textured and 35° rotated with respect to the Si(100) edge (refer Fig. 5.30). The texture spread as calculated from FWHM is found to be 12° and so these buffered substrates possess an inferior texture compared to MgO(100) single crystal substrates. Sm-Co films on top of these substrates grow with the same crystallographic texture qualitatively and, therefore, the Sm-Co c-axis has two orthogonal in-plane orientations parallel to MgO[100] and parallel to MgO[010] directions and hence, 35° rotated with respect to the Si[100] and Si[010] directions (which are along the orthogonal edges of Si substrate). Magnetic hysteresis of the sample results in a very low remanence ratio of about 0.05 (refer Fig. 5.32). The coercivity and remanence is, moreover, higher for Sm-Co films on the MgO buffered substrate compared to Sm-Co films of comparable thickness and composition on single crystal MgO(100) substrate. A detailed analysis of these results will be taken up in chapter 6.

The growth of Sm-Co films on Cr buffered MgO(110) single crystal substrates was found to be strongly dependent on buffer texture and microstructure. Cr buffers deposited at high temperatures of 700 °C possess a discontinuous and rough surface and islands of deposited material are well separated from each other as established from AFM and TEM studies (refer Fig. 5.23). Sm-Co films deposited on these high temperature buffers show unidentified poles in pole figure measurements and do not grow epitaxially. On lowering the deposition temperature of the Cr buffers, the buffer surface is found to be continuous and smoother with an rms roughness of 0.2 nm as detected with AFM. Sm-Co deposited on these smooth buffers grows epitaxially with the epitaxial relation  $\text{SmCo}_5 (10\bar{1}0)[0001] \parallel \text{Cr} (211)[0\bar{1}1] \parallel \text{MgO}(110)[001]$ , which defines only one direction of Sm-

Co c-axis parallel to Cr[011] in-plane and parallel to MgO[001] (refer Fig. 5.26). Hence, uni-axial growth of SmCo<sub>5</sub> was achieved on MgO(110) single crystal substrates with Cr buffers deposited at low deposition temperatures.

## 6 Magnetisation and Demagnetisation Mechanism

High coercivities and good magnetic texture of epitaxial  $\text{Sm}_2\text{Co}_7$  and  $\text{SmCo}_5$  thin films on different substrates make these films very suitable for detailed magnetisation analysis. Magnetisation reversal in real magnet systems can proceed through the following well understood reversal processes, namely, the coherent rotation, the nucleation and free expansion of reverse domains (nucleation-type magnet), nucleation and expansion of reverse domains, which is further hindered by defects that pin the domain wall and prohibit its free expansion (pinning-type magnet) [Cul72]. A large distinction between these processes can be made by observing the magnetic susceptibility in the initial magnetisation loop, along with investigating temperature and angular dependence of hysteresis processes.

The first section of this chapter deals with these fundamental magnetisation reversal processes in epitaxial Sm-Co thin films and concludes that reversal proceeds mainly through nucleation and growth of reverse domains which is affected by pinning and depinning of freely expanding domain walls (Hence, a pinning dominated magnetisation reversal). However, all these distinction methods have been developed and therefore are valid only for classical Stoner-Wohlfarth type single domain grains which are non-interacting. The thin Sm-Co films under investigation in this work are, however, strongly exchange coupled depending on film thickness and texture, as will be presented in section 2 of this chapter. Therefore, several of these strongly interacting small grains (nm sized) can be treated as one single big grain over which the system properties are homogeneous. Domains spanning over these bigger grains, which are ultimately composed of several smaller grains, are interaction grains and magnetisation reversal must be considered from the view point of these interaction domains.

### 6.1 Magnetisation Reversal - Coherent Rotation, Nucleation or Pinning Dominated?

The low susceptibility of the initial magnetisation loop in all the investigated Sm-Co films points towards pinning as the mechanism ruling magnetisation reversal, considering the fact that the epitaxial  $\text{SmCo}_5$  thin films are homogeneous and continuous films as seen from TEM analysis. Moreover, coercivities  $\mu_0 H_C \sim 3$  T, which are high on a comparative scale with other epitaxial Sm-Co

thin films [Ful97], are still low compared to the very high anisotropy of  $\text{Sm}_2\text{Co}_7$  (20 T) or  $\text{SmCo}_5$  ( $\sim 30$  T). A low coercivity  $\mu_0 H_C$  compared to the anisotropy field  $\mu_0 H_A$  rules out magnetisation reversal by coherent rotation in these uniaxially textured films [Kon40]. However, the observed coercivities of approx. 3 T in these films are still too high to be explained by a simple nucleation and unhindered growth of reverse domains. Therefore, to be completely exclusive in these reports, the following two analyses were performed. Together, the angular coercivity variations and the micro-magnetic model possess the potential to distinguish between coherent rotation or nucleation and growth of reverse domains and explain the reasons for high coercivities observed in these epitaxial films.

### 6.1.1 Angular Dependence of Coercivity

Magnetisation measurements with varying angle between the easy axis and the applied field is a significant tool to distinguish between the two main coercivity mechanisms of Stoner-Wohlfarth type of coherent rotation or nucleation and growth of reverse domains. The measurements were performed on  $\text{SmCo}_5$  films on  $\text{MgO}(110)$  substrates up to maximum applied fields of 7 T. The measurement angle ( $\theta$ ) was varied between zero (parallel to the easy axis) and  $90^\circ$  (parallel to the hard axis), in the film plane and out of the film plane. Hysteresis loops of this film are summarised in Fig. 6.1a, for the measurements between "in-plane easy" to "in-plane hard" measurement direction. The hysteresis loop along the easy axis is square-shaped and shows a sharp transition at the coercive field. The strong in-plane texture of the film is known from the high remanence to saturation ratio of more than 0.9. Moreover noticeable is the slope of the demagnetising loop, which is very low up to the coercive field and rises sharply at the coercive field, indicating the absence of any visible rotational processes occurring in the sample at low measurement angles in low reverse fields (to a first approximation, neglecting any intergranular coupling which can further affect the shape of the hysteresis). This also shows that the field at which the whole sample reverses its magnetisation (the maximum of the derivative of change in magnetisation) is the same as the coercive field (zero field magnetisation value). With increasing angle  $\theta$ , the shape of the hysteresis changes and the slope of the demagnetising hysteresis branch increases before a clear step in magnetisation is observed. This indicates that with increasing angle between the easy axis and the applied field, the sample magnetisation begins to rotate with the field along the field direction before it finally reverses at the critical field, called the switching field. At this point, the coercive field and the switching field no longer coincide and the switching field is a more appropriate quantity to investigate magnetisation reversal at these higher angles. As seen in Fig. 6.1a, the coercivity of the sample does not increase any more, however, the switching field continues to get higher for larger measurement angles. This variation of switching field vs. measurement angles is summarised in Fig. 6.1b. Along with the measured data points, the theoretical inverse  $\cos \theta$  curve is also shown

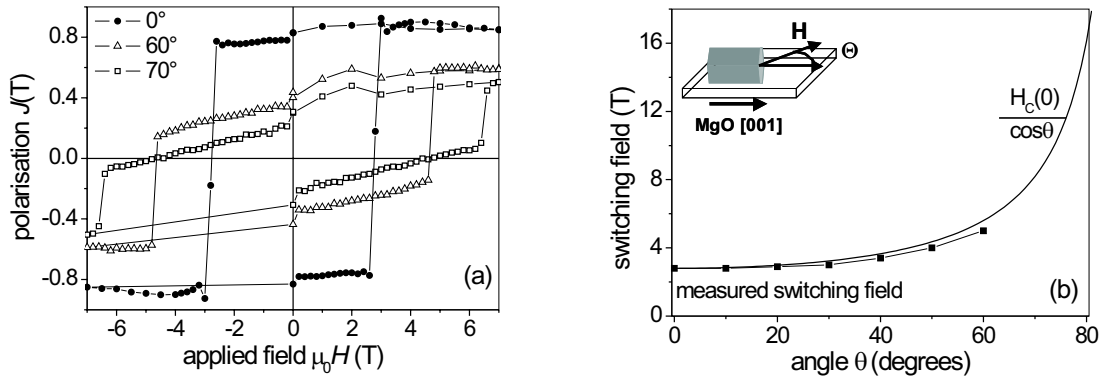


**Fig. 6.1:** Three exemplary hystereses measured at  $0^\circ$ ,  $60^\circ$  and  $70^\circ$  angle between in-plane easy axis and external field also applied in the film plane. The  $\mu_0 H_C$  does not increase any further but switching fields continue to increase at higher measurement angles. (right) Summary of switching fields with varying measurement angles along with a calculated  $1/\cos\theta$  plot, which is valid for magnetisation reversal proceeding through domain wall movement.

as a continuous line and a very close agreement is observed between the measured data points and theoretical predictions [Kon40].

Measurements were also performed along the second hard-axis direction, following the route from in-plane easy axis to out-of-plane hard axis. The hystereses have been summarised in Fig. 6.2a. The hysteresis properties remain essentially the same. Large square-shaped hysteresis along MgO[001] changes to flatter hysteresis with higher slopes at higher angles that require higher fields for saturation. At the same time, the switching field increases at these larger measurement angles. The summarised switching field distribution with increasing angles of applied field are seen in Fig. 6.2b. A close matching between the calculated  $1/\cos\theta$  dependence and measured data points proves that both the in-plane and out-of-plane hard axis are equally hard. The small deviation between measured data points and theoretical  $\cos\theta$  curve comes from an extremely insufficient available field of 7 T for sample saturation. Measurements of switching fields at angles higher than  $60^\circ$  were not possible due to the insufficient external field available to cause magnetisation reversal.

For a textured material with uni-axial anisotropy (such that the demagnetised state is characterised with parallel and anti-parallel domains), the origin of  $1/\cos\theta$  dependence of the switching field in the presence of obliquely applied fields, lies in the nucleation of a  $180^\circ$  domain wall in the textured material. If the external field is applied at an angle  $\theta$  with respect to the  $c$ -axis of a uniaxially textured magnet, then the applied field component  $H_{app}\sin\theta$  acts perpendicular to the magnetisation vectors and is responsible for causing rotation of moments. However, if the anisotropy of the material is very high, no appreciable moment rotation can occur up to the anisotropy field

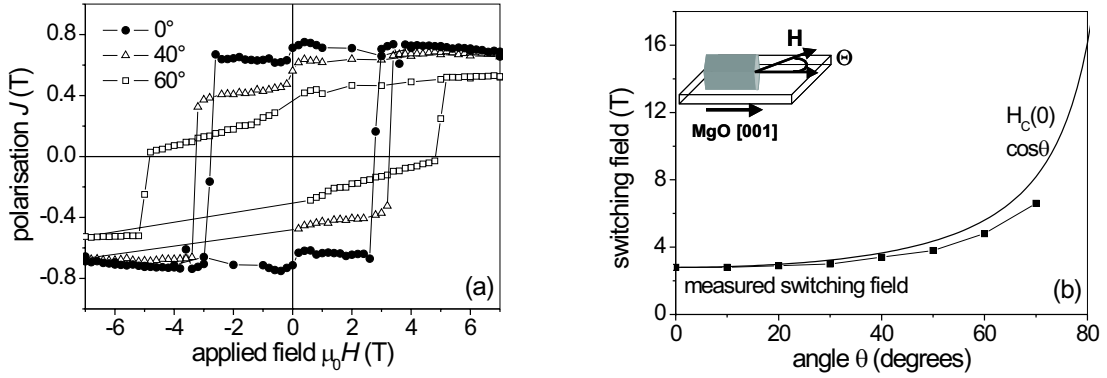


**Fig. 6.2:** Hystereses measured at varying angle between the in-plane easy axis and applied field out-of-plane (left). Summarised switching field resembling  $1/\cos \theta$  dependence for switching field applicable for pinning systems.

and the effect of this component remains negligible in high anisotropy materials. Therefore, the second field component  $H_{\text{applied}} \cos \theta$ , which acts anti-parallel to the domain magnetisation, is alone effective in causing magnetisation reversal to occur at an effective field such that  $H_{\text{eff}} \cos \theta = H_{\text{switch}}(0)$ . This very good agreement of the measured angular dependence with  $1/\cos \theta$ , observed in epitaxial hard magnetic Sm-Co films, vouches for the high quality of crystallographic texture in these films in addition to clearly identifying the magnetisation reversal in these films to proceed through nucleation of  $180^\circ$  domain walls and the growth of these reversed domains [Giv91]. This reversal mechanism has indeed been observed in orthoferrite single crystals of the type  $\text{M-Fe-O}_3$  where M stands for Y or other rare-earth metals. The crystal sizes were kept very small ( $< 30$  mg in weight) in order to avoid any disturbance in measured angular dependence because of defects or deteriorated crystal quality [Rei65]. The  $1/\cos \theta$  dependence was also observed in  $\text{SmCo}_5$  and  $\text{GdCo}_5$  single crystals [Men74] [Bec72]. A weak  $1/\cos \theta$  dependence was also observed in Nd-Fe-B bulk magnets [Elb91]. Although Wang *et al.* and Yang *et al.* also observed similar dependence in half-metallic ferromagnetic thin films having very low coercivities of about 17 Oe [Yan00], [Wan03], in real hard magnetic thin films there have been no reports so far for such a close observation of  $1/\cos \theta$  law, which asserts that the texture and quality of these epitaxial films is comparable to their single crystal counterparts.

This  $1/\cos \theta$  variation is unlike the switching field variation in systems reversing their magnetisation by coherent rotation, where after an initial decrease in switching field with increasing angle up to  $45^\circ$  between the applied field and magnetisation a symmetric increase is observed again up to an angle of  $90^\circ$  (It has been calculated by Kou *et al.* [Kou94] for Pr-Fe-B magnets). This distribution, which is known as the Stoner-Wohlfarth angular behaviour, is therefore symmetric around  $45^\circ$  and increases on either side of this central angle value. This angular dependence has also been

observed for Nd-Fe-B bulk magnets by including the non-negligible second anisotropy constant for Nd-Fe-B ( $K_2$ ) and a small grain misalignment [Kro87]. The observed angular dependence is clearly different to the  $1/\cos \theta$  dependence of the switching field observed in epitaxial Sm-Co films.

### 6.1.2 Micro-Magnetic Model

The angular dependent hysteresis measurements rule out any possibility of magnetisation reversal occurring through coherent rotation of magnetisation in these films and identify the magnetisation reversal to be initiated by formation of reverse domains with  $180^\circ$  domain wall and the propagation of domain wall through the material. A domain wall propagating through the material may pass unhindered (free expansion) or it may be pinned at defect sites. However, a free expansion of the domain walls would lead to low coercivities in these textured and largely defect free thin films. The micro-magnetic model describes the role of these defects in the magnetisation reversal process of nucleation or pinning. Therefore, magnetisation reversal investigations were furthered by applying this model to  $\text{SmCo}_5$  thin films prepared on different substrates (refer section 2.3). The model describes the coercivity (at zero magnetisation) of the system as a reduced anisotropy field and incorporates the effect of defects and inhomogeneities as the entities responsible for this reduction [Kro87], [Kro88]. The model introduces temperature independent parameters like  $\alpha_{\text{eff}}$  and  $N_{\text{eff}}$  to express the reduction in the anisotropy field  $H_A = (2 \mu_0 K_1) / J_S^2$  and is a modification of the Stoner-Wohlfarth model. It is based on the solution of the following equation to describe coercivities:

$$\frac{\mu_0 H_C}{J_S} = \frac{2\mu_0 K_1}{J_S^2} \alpha_{\text{eff}} - N_{\text{eff}} \quad (6.1)$$

where  $\alpha_{\text{eff}}$  and  $N_{\text{eff}}$  are temperature independent parameters introduced as a modification of the Stoner-Wohlfarth model and  $\alpha_{\text{eff}}$  incorporates the effect of microstructural defects, texture effects [Kro87] and the effect of grain interactions [Kou94]

$$\alpha_{\text{eff}} = \alpha_\phi \cdot \alpha_K \quad (6.2)$$

Here,  $\alpha_\phi$  is the angular dependent component of  $\alpha_{\text{eff}}$  and  $\alpha_K$  is the isotropic microstructural parameter (and is independent of measurement direction). The temperature dependence of  $\mu_0 H_C$  and  $J_S$  of the samples were measured and the same for first anisotropy constant  $K_1$  was taken from the literature for single crystal measurements [Bar76].  $N_{\text{eff}}$  and  $\alpha_{\text{eff}}$  were evaluated for all three different kinds of Sm-Co textures and the results, as plots of equation 6.1, are summarised in the three subsections below.

**(a) SmCo<sub>5</sub> Films on Single Crystal MgO(100) Substrates**

Hysteresis loops were measured for a 50 nm thick SmCo<sub>5</sub> film on a MgO(100) substrates at several temperatures varying from 300 K down to 50 K in PPMS VSM along the MgO[100] direction (Fig. 6.3a). The individual hystereses get broader at lower temperatures. The slope of the hystereses loops (in the first quadrant) is still quite steep, indicating that the samples are difficult to saturate even when measured in fields up to 9 T. The difficulty in saturating these samples comes from the twofold orientation of the easy axis in the film plane. While the magnetisation along one of the easy axes begins to switch at high field, the complimentary magnetisation from the second easy axis continues to rotate and results in a non-zero slope up to large external fields.

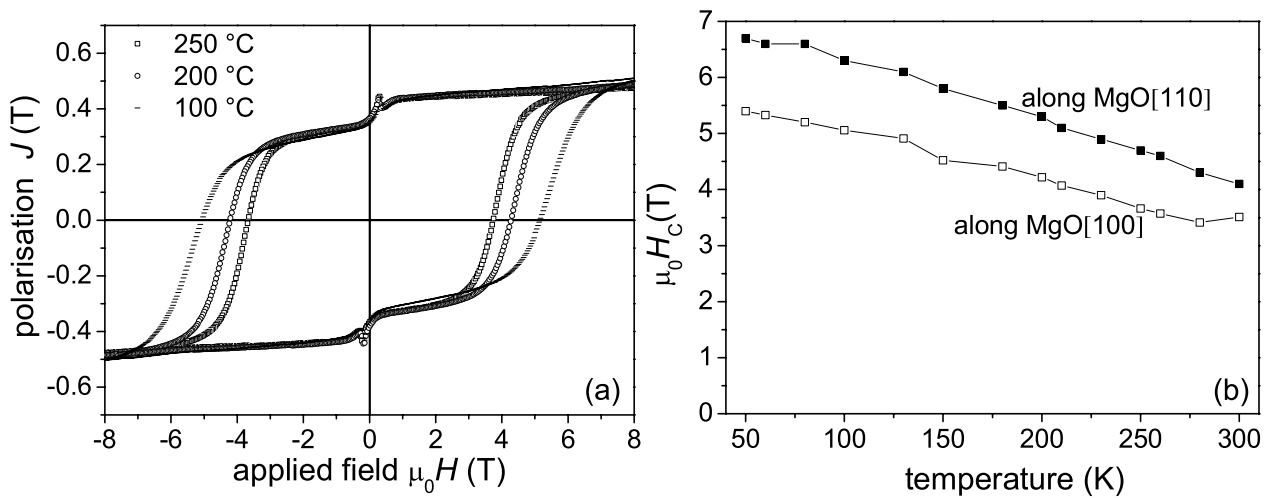


**Fig. 6.3:** (Left) Hysteresis loops of SmCo<sub>5</sub> measured at three different temperatures in a 9 T PPMS VSM. The hysteresis gets broader with lowering measurement temperature. (Right) Coercivity vs. measurement temperature along MgO[100] and MgO[110] directions. Coercivity is higher along MgO[110] direction at each measurement point and it increases with lowering temperature for both the directions.

The coercivity of these samples increases monotonically with decreasing measurement temperature along the easy axis attaining high values of about 5.5 T at 50 K (Fig. 6.3b). Similar measurements performed along MgO[110] result in coercivities approaching 7 T at 50 K. The coercivity along MgO[110] was found to be higher at every measurement point as compared to that along MgO[100]. The variation of coercivity along both the directions is seen in Fig. 6.3b. Similarly, the saturation polarisation  $J_S$  of the samples was calculated from the measured remanence  $J_R$  using Stoner-Wohlfarth calculations. The saturation polarisation  $J_S$  is twice the remanent polarisation  $J_R$  value for the given easy-axis distribution in SmCo<sub>5</sub> thin films on MgO(100) and these  $J_S$  values are plotted in Fig. 6.4. In Fig. 6.4, the known temperature dependence of saturation polarisation  $J_S$  of the SmCo<sub>5</sub> phase [Men74] is additionally plotted based on its room temperature saturation polarisation value of 1.14 T [Bus98]. The measured values are about 30% smaller than the expected

$J_S$  values. The difference is understandable, due to an approx. 10% error introduced in an accurate thickness determination with EDX measurements and the additional uncertainty of remanent polarisation  $J_R$  due to incomplete saturation of the sample. It is thus assumed, that measurements underestimate the saturation magnetisation and, therefore, the expected saturation magnetisation has been used for evaluating the micro-magnetic model.

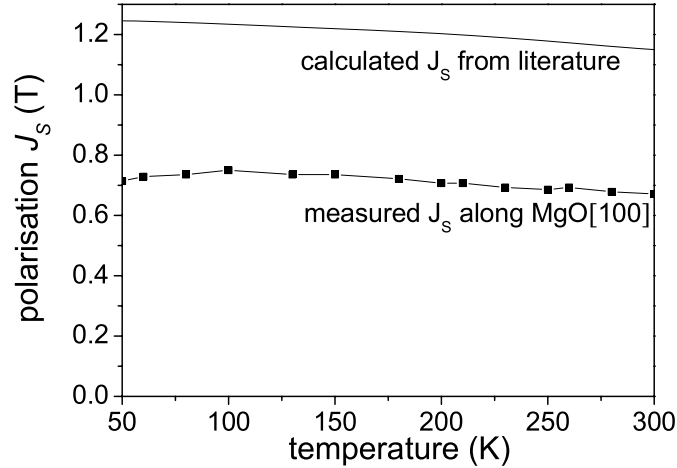


**Fig. 6.4:** Temperature dependence of the saturation polarisation of a single crystal of  $\text{SmCo}_5$  [Men74], [Bus98] and as measured in  $\text{SmCo}_5$  thin films along the easy axis.

The temperature dependence of the first anisotropy constant  $K_1$  of  $\text{SmCo}_5$  was also taken from the measurements reported by Barbara *et al.* [Bar76] on  $\text{SmCo}_5$  single crystals. The  $H_A$  values calculated from this data set were closest to the often quoted anisotropy field of  $\text{SmCo}_5$  and gave reasonable results for the temperature dependence of  $H_A$ . Both, the temperature dependence for  $K_1$  as given by Barbara *et al.* [Bar76] and the temperature dependence of calculated  $H_A$  using this  $K_1$  and the expected  $J_S$  from Fig. 6.4 are presented in Fig. 6.5.

Using the temperature dependence of measured and calculated variables in Eq. 6.1, the plot of normalised coercivity  $\mu_0 H_C / J_S$  vs. normalised anisotropy field  $\mu_0 H_A / J_S$  is shown in Fig. 6.6a as scattered data points for several temperatures between 400 K and 50 K. The data points show a linear dependence with a slope of  $0.17 \pm 0.01$ , which can be directly related to the  $\alpha_{\text{eff}}$  value and the small error shows a high accuracy of the performed regression.

Similar plots for determination of  $\alpha_{\text{eff}}$  parallel to the  $\text{MgO}[110]$  in the film plane are seen in Fig. 6.6b. An increased  $\alpha_{\text{eff}}$  of 0.21 was observed from linear fitting of  $\mu_0 H_C / J_S$  vs.  $2\mu_0 K_1 / J_S^2$  using equation 6.1 along  $\text{MgO}[110]$ . The coercivity  $\mu_0 H_C$  changes from 3.6 T along the  $\text{MgO}[100]$  direction to 4.7 T along the  $\text{MgO}[110]$  direction, and correspondingly  $\alpha_{\text{eff}}$  increases from a normalised value of 1 along  $\text{MgO}[100]$  to 1.2 along  $\text{MgO}[110]$ .

The effect of  $\text{SmCo}_5$  film thickness on magnetisation reversal was also investigated by performing the micro-magnetic analysis on a 150 nm thick  $\text{SmCo}_5$  film along similar  $\text{MgO}$  substrate

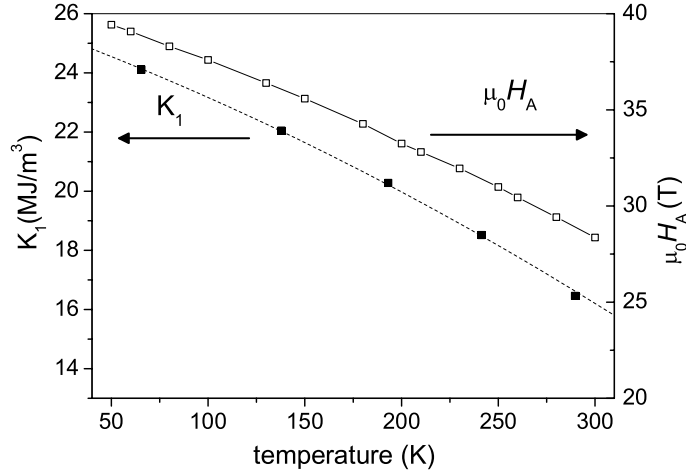


**Fig. 6.5:** Decreasing trend of  $K_1$  with temperature (left). Calculated  $H_A$  fields using these  $K_1$  values (Scaled to the right) which give reasonable results for  $\text{SmCo}_5$ .

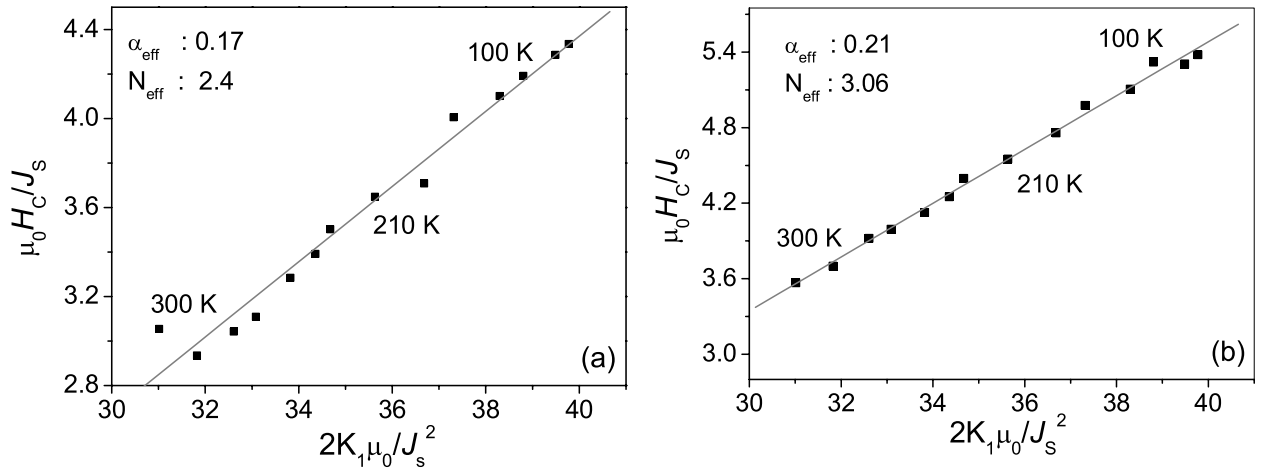


**Fig. 6.6:** Micro-magnetic model calculations for evaluating  $\alpha_{\text{eff}}$  and  $N_{\text{eff}}$  from the temperature dependence of  $\mu_0 H_C$ ,  $J_S$  and  $K_1$  along  $\text{MgO}[100]$  (left) and  $\text{MgO}[111]$  (right) for  $\text{SmCo}_5$  films on  $\text{MgO}(100)$  substrates.  $\alpha_{\text{eff}} < 0.3$  indicates dominating pinning.

directions, viz  $\text{MgO}[100]$  and  $\text{MgO}[111]$ . Lower coercivities were observed along both the directions compared to analyses on thinner films (50 nm). The important results on these two different samples are summarised in Tab. 6.1. The  $\alpha_{\text{eff}}$  values show similar trends as on thinner films and an increase from 0.08 along  $\text{MgO}[100]$  for thick  $\text{SmCo}_5$  film to 0.1 along  $\text{MgO}[111]$  direction is observed. A higher  $\alpha_{\text{eff}}$  along the  $45^\circ$  direction in both the cases (100 nm thick  $\text{SmCo}_5$  and 50 nm thick  $\text{SmCo}_5$ ) is attributed to a contribution of angular dependent  $\alpha_\phi$  variable to the total  $\alpha_{\text{eff}}$  (refer Eq. 6.2) since the microstructural contribution  $\alpha_K$  has to remain unchanged within the sample along different measurement directions and inter-grain interactions are neglected for simplicity.

**Table 6.1:** Comparison between  $\mu_0 H_C$ ,  $\alpha_{\text{eff}}$  and  $N_{\text{eff}}$  along  $\text{MgO}[100]$  and  $\text{MgO}[110]$  for two  $\text{SmCo}_5$  films – 50 nm thick (thin film) and 150 nm thick (thick film).

	$\mu_0 H_C^{\text{MgO}[100]}$	$\alpha_{\text{eff}}^{\text{MgO}[100]}$	$N_{\text{eff}}$	$\mu_0 H_C^{\text{MgO}[110]}$	$\alpha_{\text{eff}}^{\text{MgO}[110]}$	$N_{\text{eff}}$
Thin Sm-Co	3.6 T	0.17	2.4	4.7 T	0.21	3.06
Thick Sm-Co	1.7 T	0.08	1.1	2.25 T	0.1	1.4

The observed increments in  $\alpha_{\text{eff}}$  for both the thick and the thin  $\text{SmCo}_5$  samples along the  $45^\circ$  direction are well explained by considering a  $1/\cos \theta$  dependence of the  $\alpha_\phi$  parameter. Moreover, the larger grain sizes in thicker samples as evident from TEM images (where grain sizes are found to be proportional to film thickness) lead to weaker inter-grain coupling (as will be seen in the following section) and, hence, lower the  $\alpha_{\text{eff}}$  value along with lowering the coercivities in thicker samples.

Based on the defect sizes, the  $\alpha_{\text{eff}}$  value performs the distinction between nucleation dominated and pinning dominated magnetisation reversal mechanisms (section 2.8). A high value of  $\alpha_{\text{eff}}$  that is greater than 0.35 is unambiguously related to magnetisation reversal by coherent rotation or nucleation dominated reversal [Kro88] (section 2.3 - 2.8). Hannemann *et al.* reported high  $\alpha_{\text{eff}}$  values of about 1 in epitaxial NdFeB films [Han03] and, likewise,  $\alpha_{\text{eff}}$  values greater than 0.35 have repeatedly been associated with a nucleation model for coherent rotation [Cad87b], [Kou94]. Similarly, a lower value of  $\alpha_{\text{eff}}$  less than the critical  $\alpha_{\text{eff}}$  value of 0.35 does not rule out nucleation in the system (refer Fig. 2.8) but is more often attributed to a magnetisation reversal dominated by pinning processes mainly as has been cited by [Kro88], [Tel97], [Che97], [Pin04].

Hence in conclusion, magnetisation reversal in  $\text{SmCo}_5$  films on  $\text{MgO}(100)$  substrates occurs mainly by nucleation and expansion of reverse domains (due to the inverse  $\cos \theta$  dependence of  $\alpha_{\text{eff}}$  from hysteresis measurements performed along  $0^\circ$  and  $45^\circ$  to the easy axis). The expansion of domain walls is further hindered by pinning of these domain walls at defect sites and inhomogeneities in these films (low  $\alpha_{\text{eff}} < 0.35$  from micro-magnetic model). The orthogonal grain boundary network, resulting from two orthogonal c-axes texture in  $\text{SmCo}_5$  films on  $\text{MgO}(100)$  single crystal substrates are seen as potential pinning sites resulting in high coercivities in these films besides pinning at other defect sites and stacking faults. The exact nature of pinning sites however, requires direct observation of these pinning centres by microscopy techniques which due to very small grain sizes ( $\sim 30\text{--}40$  nm) is still a challenge for these thin films.

### (b) $\text{Sm}_2\text{Co}_7$ Films on IBAD $\text{MgO}(100)$ Substrates

Qualitatively, the films on IBAD  $\text{MgO}(100)$  substrates are similar to Sm-Co films on single

crystal MgO(100) substrates besides a much larger in-plane texture spread of approx.  $10^\circ$  as observed in pole figure measurements. Temperature dependent hysteresis loops measured for a 120 nm thick Sm-Co film on an IBAD MgO substrate have been summarised in Fig. 6.7a. The film has a room temperature coercivity of 3.6 T and the in-plane hysteresis increases with decreasing measurement temperature as seen in Fig. 6.3 before. Furthermore, the switching of the sample occurs with a remarkably narrow switching field distribution and the reversal is more collective as compared to samples on single crystal substrates which showed a more gradual reversal.

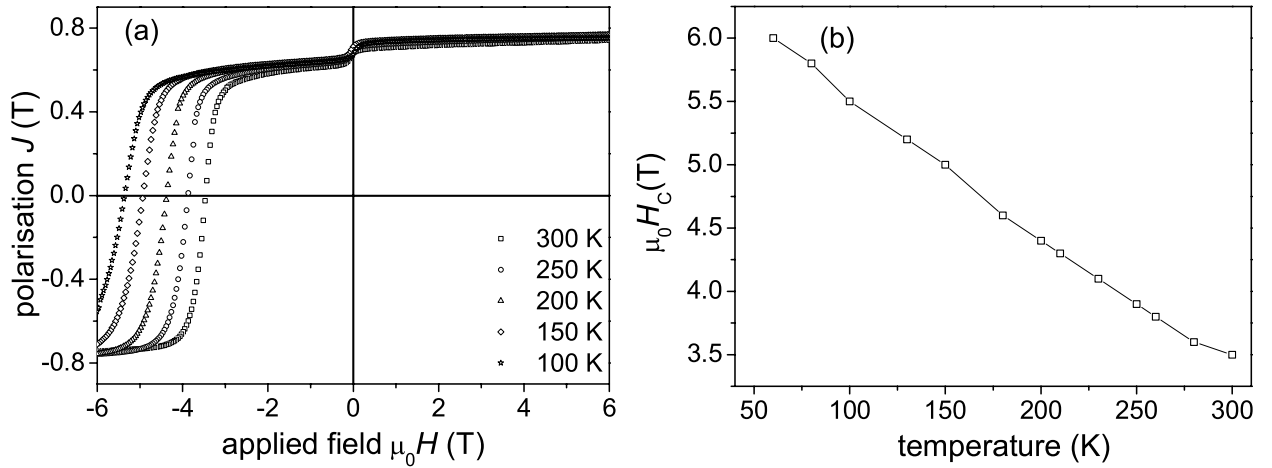


**Fig. 6.7:** Selective hysteresis loops measured on a thick Sm<sub>2</sub>Co<sub>7</sub> film on IBAD MgO(100) substrate (MgO/Si) at different temperatures along Si[100]. Summary of coercivity with temperature along Si[100].

As seen from Fig. 6.7b, the coercivity of the sample increases monotonically with reduced temperature, almost doubling in value at temperatures close to 50 K. The coercivity for this thick Sm-Co sample is approx. 40% higher than the coercivity of a comparably thick Sm-Co film on a MgO(100) single crystal substrate. Measured temperature variation of polarisation at 9 T (measured 'saturation polarisation') and expected saturation polarisation calculated on the basis of the room temperature  $J_S$  value of 1.14 T as cited by Buschow [Bus98] are plotted in Fig. 6.8. The small difference in calculated saturation polarisation and expected saturation polarisation can be attributed to the inaccuracy in thickness determination. The known decreasing trend of saturation polarisation with temperature is, however, clearly reproducible.

Micro-magnetic analysis was performed on this sample only along Si[100]<sup>1</sup>. The resulting plot of  $\mu_0 H_C / J_S$  vs.  $2\mu_0 K_1 / J_S^2$  is shown in Fig. 6.9.  $N_{\text{eff}} = 5.5$  and  $\alpha_{\text{eff}} = 0.15$  are obtained along Si[100] for a good linear dependence observed in measured data points. This  $\alpha_{\text{eff}}$  value is less than the

<sup>1</sup>The magnetic measurements along Si[100] are comparable to magnetic measurements along MgO[110] of MgO(100) single crystal substrates since the IBAD MgO buffer on Si grows  $36^\circ$  rotated in-plane and with a much larger texture spread of  $12^\circ$  it has the [110] direction parallel to Si[100] direction.

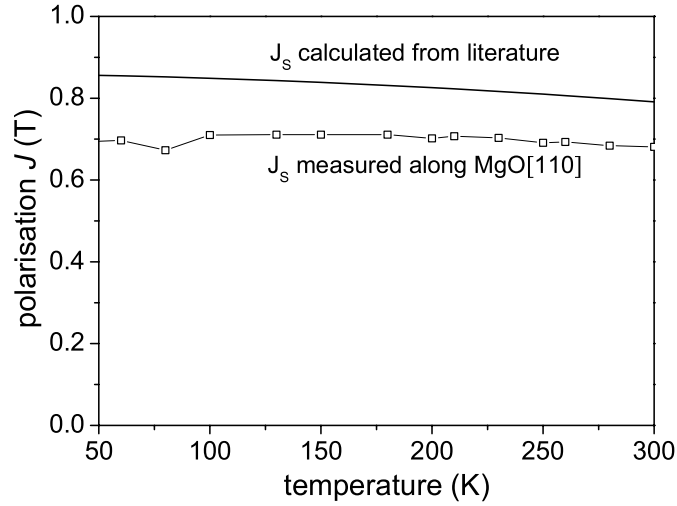


**Fig. 6.8:** Measured temperature dependence of  $J_s$  compared to calculated temperature dependence of  $J_s$  for  $Sm_2Co_7$ .

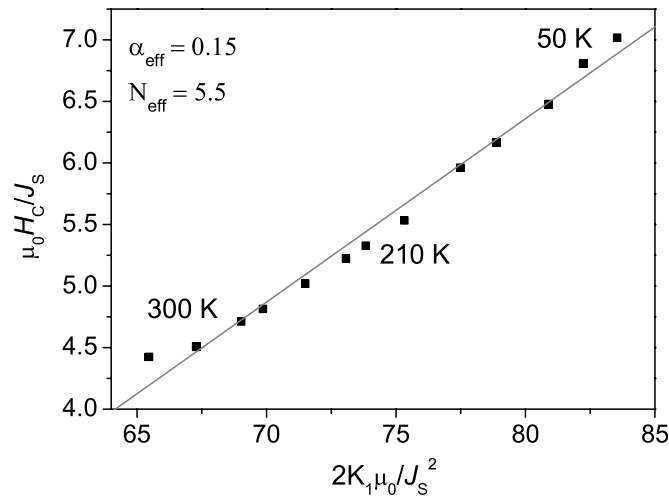


**Fig. 6.9:** Temperature dependent micro-magnetic model fit for  $Sm_2Co_7$  film on IBAD MgO. Values of  $\alpha_{eff}$  on IBAD MgO substrate are higher than for comparable films on single crystal MgO substrates, indicating more effective pinning on these substrates.

critical value of 0.35, which again indicates that pinning is the dominating mechanism governing magnetisation reversal. Moreover, this  $\alpha_{eff}$  value is larger than the value for a comparably thick Sm-Co sample on a single crystal MgO(100) substrate ( $\alpha_{eff} = 0.1$ ) indicating a stronger and more effective pinning in these films prepared on IBAD MgO. The effectiveness in pinning comes from the smaller grain size in  $Sm_2Co_7$  films on IBAD MgO substrates, which produces a much higher density of grain boundaries in the sample. These grain boundaries can pin the domain walls more effectively and block their easy passage through the entire sample. Of course the presumption with increased number of grain boundaries due to reduced grain sizes or other forms and types of

defects like stacking faults, dislocations etc., require extensive and effective TEM work for confirmation. The effectiveness of pinning on IBAD-MgO substrates compared to single crystal MgO substrates, however, finds sufficient evidence from magnetic measurements alone.

### (c) $\text{SmCo}_5$ Films on $\text{MgO}(110)$ Substrates

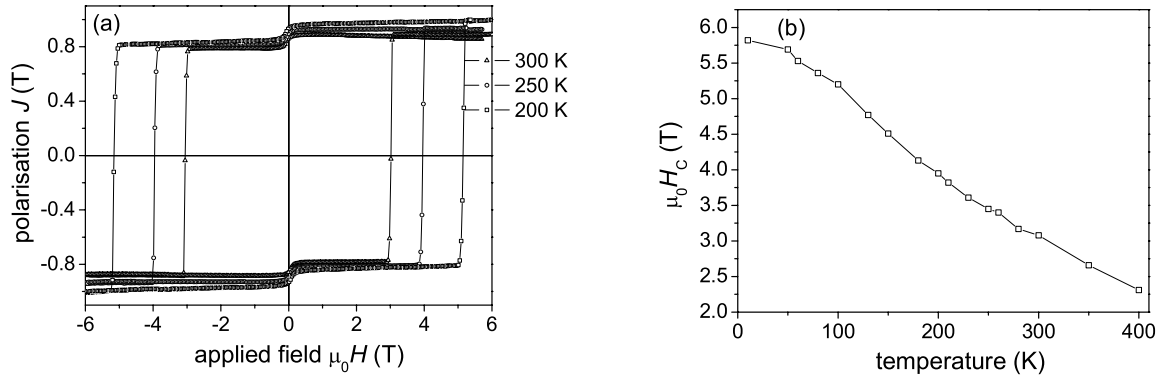


**Fig. 6.10:** Hysteresis measurements at different temperatures for uniaxially textured  $\text{SmCo}_5$  films on  $\text{MgO}(110)$  (Left). The hysteresis loops are ideally square-shaped with high coercivity, which increases with lowering measurement temperature up to almost 6 T at 50 K (right).

Temperature dependent coercivity analysis using the micro-magnetic model was performed on uniaxially textured  $\text{SmCo}_5$  thin films (50 nm) on  $\text{MgO}(110)$  single crystal substrates. The films possess an in-plane magnetic texture better than 0.02, with in-plane easy axis coercivity of 3.1 T. The  $c$ -axis is perfectly aligned in-plane along the  $\text{MgO}[001]$  direction with a texture spread of approx.  $3^\circ$ . Sharp and very abrupt switching of magnetisation occurs from one magnetisation state to the opposite at precisely the coercive field. Temperature dependent hystereses for this film are shown in Fig. 6.10 and along with it the variation of coercivity with temperature has been summarised. The coercivity increases from an already high value of 3.1 T at 300 K to its exact double at 10 K.

Measured saturation polarisation at 9 T follows the theoretical curve for saturation polarisation with an acceptable error induced due to film thickness determination (see Fig. 6.11 a). The decreasing trend of saturation polarisation with temperature is nicely reproduced in the measured data at 9 T. The dependence of the coercivity normalised to this saturation polarisation on a similarly normalised anisotropy field is linear with a slope ( $\alpha_{\text{eff}}$ ) of 0.18 as seen in Fig. 6.11 b. This value of  $\alpha_{\text{eff}}$  compares well with the  $\alpha_{\text{eff}}$  value on  $\text{MgO}(100)$  for similar thickness, measured along the easy axis. Although the twin-grain boundary network resulting from orthogonal easy-axis distribution of  $\text{SmCo}_5$  films on  $\text{MgO}(100)$  substrates are understandably the most effective pinning points on these substrates, the grain boundaries can not be equally efficient in  $\text{MgO}(110)$  single crystals due

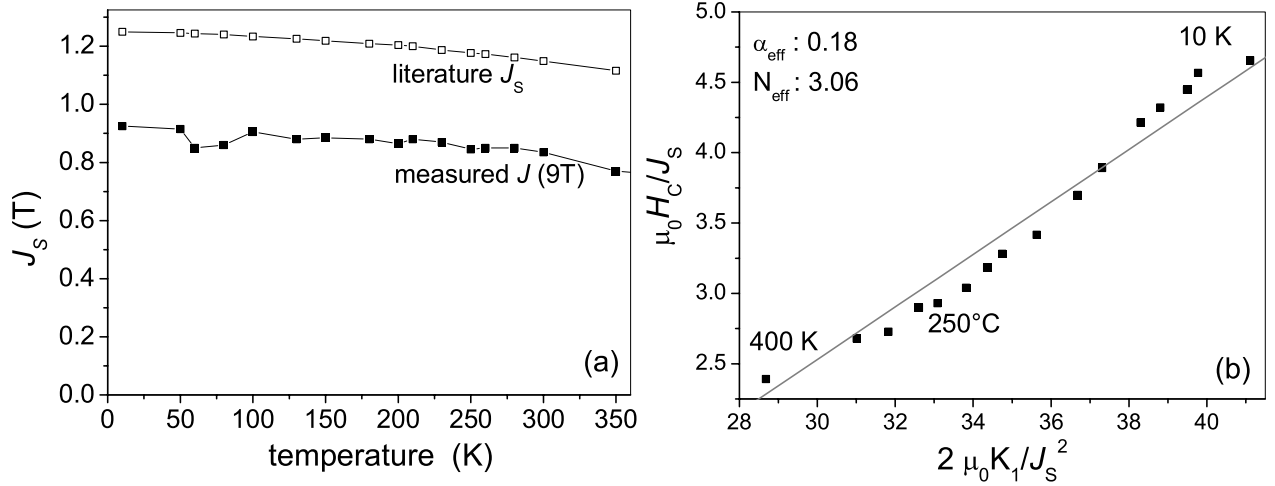


**Fig. 6.11:** Calculated and measured temperature dependence of  $J_s$ . The measured temperature dependence closely resembles the calculated temperature dependence (left). On the right image is the plot of micro-magnetic model, resulting in  $\alpha_{\text{eff}}$  of about 0.18, hinting to pinning in the system.

to single easy-axis orientation. The pinning of domain walls on MgO(110) substrates has to be considered taking *collective coupling processes* between several small  $\text{SmCo}_5$  grains (30–40 nm) into account (to be discussed in the next section). The small  $\text{SmCo}_5$  grains on this substrate do not behave as individual grains but many of them behave collectively as one big *crystallographic entity* or a *pseudo-grain*, due to the very good texture in these films. This larger pseudo-grain is the smallest, uniform, homogeneous and coherent magnetic structure of the sample and forms a single domain called an *interaction domain* and is the equivalent of the single classical domain that covers a single crystallographic grain. Therefore, magnetisation reversal requires the interaction domains to reverse their magnetisation and is affected by the pinning of these domain walls. The nature of pinning sites in these highly textured epitaxial films, therefore, depends on the coupling between the grains and the texture of the film and pinning has to be considered differently. The theory of magnetisation reversal, which very well explains the magnetisation reversal in classical domain systems, is still not so well developed in materials with interaction domains.

## 6.2 Verification of Intergranular Exchange Coupling

The phenomenon of intergranular exchange can have large effects on the magnetic properties of samples. This microscopic effect can be seen through magnetic measurements and, if large, can affect hysteresis loops. The absence of intergranular exchange is seen in a fulfilled Wohlfarth condition namely:

$$J_R^D(H_m) = J_R - 2J_R^m(H_m) \quad (6.3)$$

Since this equation is valid for perfectly non-interacting, single domain, ellipsoidal particles with uni-axial anisotropy, any deviation from this ideality would be largely the result of interactions in the system considering no violations of this law due to the average  $\text{SmCo}_5$  grain size in these films (50–100 nm) which is well below the single domain limit ( $> 500$  nm) and the system exhibits uni-axial anisotropy. Moreover, the restriction imposed by the ellipsoidal shape is relaxable again in these samples since the actual shape of the particle/sample largely affects the stray field contribution to the net anisotropy whose contribution is small compared to the huge magneto-crystalline anisotropy in these materials. Hence, any interactions in the system can be visualised as deviations  $\delta J$ , from the above equality.

### 6.2.1 Measurement of Recoil Loops - $\delta J$ Plot

Remanence loops were measured starting from a thermally demagnetised state with successively increasing applied fields in fine steps of 0.1–0.25 T up to a maximum applied field of 9 T. The process was repeated for the demagnetising hysteresis branch with similar field steps. These remanence loops for a 40 nm thick  $\text{SmCo}_5$  sample on  $\text{MgO}(100)$  single crystal substrates are shown in Fig. 6.12a. The magnetisation increases in very small steps all through the magnetising branch.

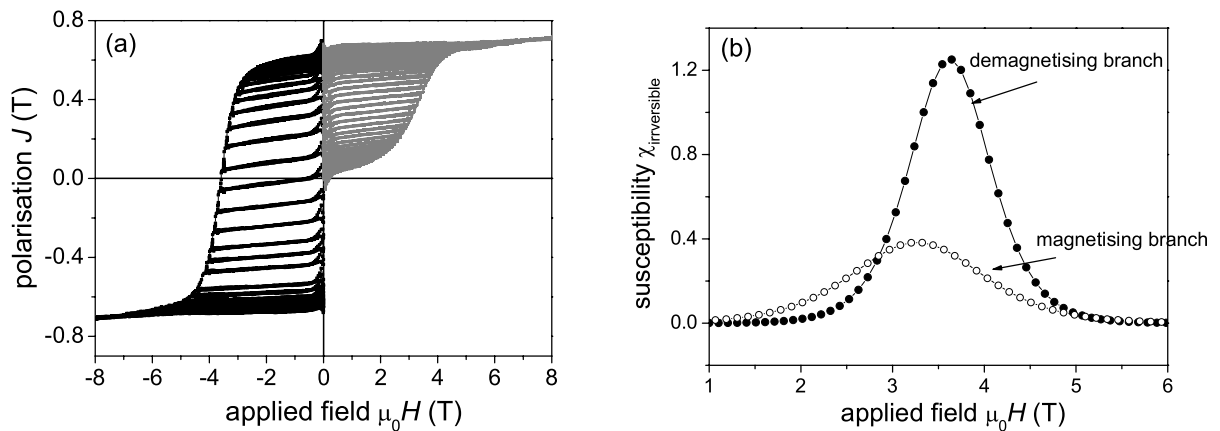


**Fig. 6.12:** (a) Recoil loops for a  $\text{SmCo}_5$  film on  $\text{MgO}(100)$  single crystal substrate measured along  $\text{MgO}[110]$ . The recoil loops are measured starting from a thermally demagnetised state and after applying reverse fields of increasing magnitude. (b) Comparison of irreversible susceptibility for the magnetising and demagnetising branches as a function of applied field.

It also changes slowly for small reverse field amplitudes in the demagnetising branch (Fig. 6.12b). However, for intermediate reverse fields ( $\sim 3.5$  T which is close to the coercive field) in the demagnetisation branch, with small increments in reverse field amplitude, a larger increase in the sample magnetisation is observed. Both these observations are clearly seen in Fig. 6.12b. For similar applied field increments, the change in magnetisation is more than twice as large in the demagnetisation

branch as compared to the magnetisation branch, seen as the larger amplitude of the gaussian distribution for the demagnetising branch than for the magnetising branch. The large magnetisation changes are due to a collective magnetisation reversal occurring within the grains where several grains reverse their magnetisation direction together for the same field value and therefore result in a sharper reversal field distribution. This already hints to the existence of exchange coupling in the system. More evidence on the nature of magnetic coupling is deduced by plotting  $\delta J$  plots (Fig. 6.13). The positive peak in  $\delta J$  vs. applied field shows that a definite exchange coupling is present in these systems along with a small amount of magnetostatic coupling, which is responsible for the negative undershoot seen in the figure. Similar  $\delta J$  measurements on a thicker  $\text{SmCo}_5$

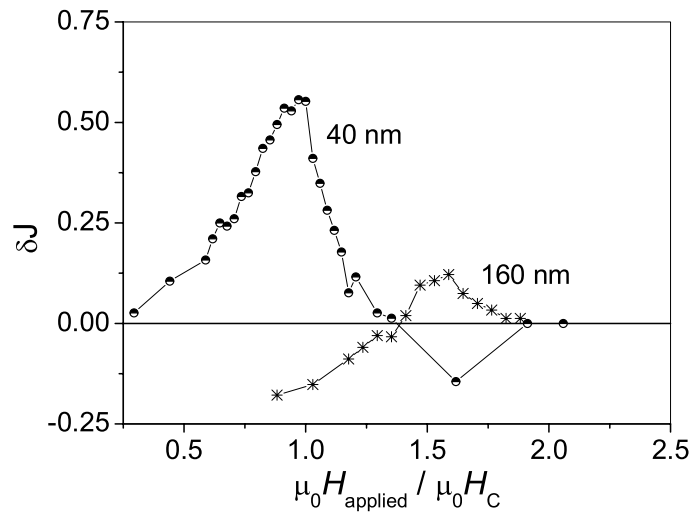


**Fig. 6.13:**  $\delta J$  plots calculated from recoil loops for two  $\text{SmCo}_5$  films of different thicknesses (40 nm and 160 nm) on  $\text{MgO}(100)$  substrate. The positive peak in  $\delta J$  plot indicates a system where exchange coupling dominates over magneto-static coupling.

film (150 nm) are also seen in the same figure. The positive peak is much smaller in amplitude and it is strongly shifted to the right (i.e. higher applied fields which are normalised to the coercive field). Both the findings indicate a weaker exchange coupling in thicker films [Bea91], which is due to a larger grain size and hence a reduced interaction surface for positive exchange.

The exchange coupling was investigated in small grained Sm-Co samples on IBAD MgO substrates by measuring similar recoil loops. The measurements were performed both, starting from thermally demagnetised state and after saturating the sample in 9 T field, for the demagnetising branch (Fig. 6.14a). The loops are qualitatively comparable to recoil loops of Sm-Co samples on single crystal MgO substrates, in both the directions. However, the switching field distribution  $\chi$  ( $(\partial M/\partial x)_{\max}$ ) in the demagnetising branch is narrower for films on these substrates compared to similar films on single crystal substrates (Fig. 6.14b) indicating a collective reversal in a narrow field range. Additionally, for similar small changes in reverse field magnitude, large irreversible changes in sample magnetisation are observed. These steps in the demagnetising branch for films

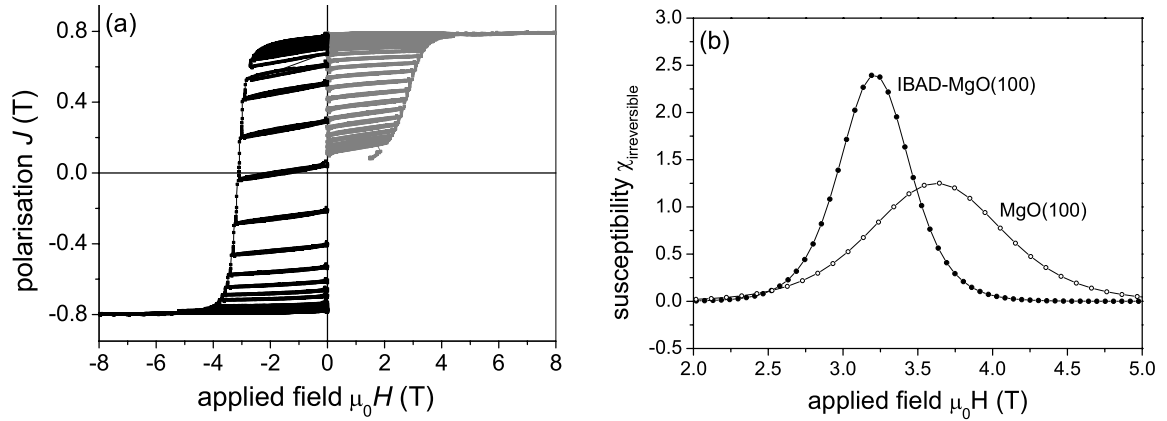


**Fig. 6.14:** (a) Recoil loops measured on  $\text{Sm}_2\text{Co}_7$  film on IBAD MgO substrate. (b) Comparison of irreversible susceptibility for a sample on IBAD MgO and a sample on single crystal MgO. The higher peak in the susceptibility curve indicates that the steps in the demagnetising branch are larger and more discrete for the film on IBAD MgO substrate compared to similar films on single crystal substrates.

on IBAD MgO are much larger as compared to steps in films on single crystal MgO (directly seen by comparing the amplitudes of the two gaussian distributions). These differences are understandable from the  $\delta J$  plot for a IBAD MgO sample (sample A; 120 nm thick) and comparable samples on single crystal MgO (Sample A'; comparable thickness  $\sim 160$  nm and Sample B; 40 nm thick) (refer Fig. 6.15). The  $\delta J$  peak is much higher in sample A and shifts to lower normalised magnetic fields as compared to samples B and A'. For comparable thicknesses, viz sample A and A', the  $\delta J$  on the IBAD MgO sample is more than 4 times larger. This indicates an extremely high exchange coupling in the sample on IBAD MgO and a negligible magnetostatic contribution compared to the sample on single crystal MgO, which has a non-negligible magnetostatic coupling as well. The small grains of Sm-Co samples on IBAD MgO substrate are more strongly exchange coupled, which is why they show collective magnetisation reversal. Although the reversal occurs at smaller normalised fields, it is more coherent and sharp.

The amount and effect of exchange coupling was also investigated on perfectly uniaxial Sm-Co thin films on single crystal MgO(110) substrates. The films were particularly interesting because due to the very well aligned easy axis, this system is the closest to studying the intrinsic properties of  $\text{SmCo}_5$  materials. Investigation on exchange coupled grains was performed by measuring recoil loops as before. The recoil loops for the  $\text{SmCo}_5$  sample have been summarised in Fig. 6.16.

Looking at the demagnetising branch, one can clearly see that the entire switching occurs at effectively one single field value indicating that the entire sample behaves as a strongly connected single domain system. The switching barrier does not change much from grain to grain and the film is extremely homogeneous in its magnetic properties. As expected,  $\delta J$  plots show a huge increase in positive value as compared to measurements on single crystal MgO(100) or even for

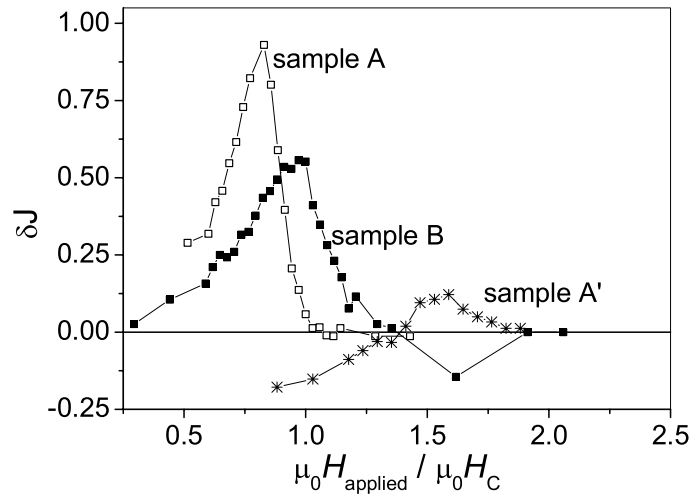


**Fig. 6.15:** Comparison between  $\delta J$  plot for a film on IBAD MgO substrate (sample A, which is 120 nm in thickness) and films on single crystal MgO(100) substrates (sample A' and sample B, 160 nm and 40 nm in thickness respectively). More than four times higher positive  $\delta J$  peak amplitude for sample A on IBAD MgO compared to sample A' on single crystal MgO substrate with comparable thickness indicates greater exchange coupling.

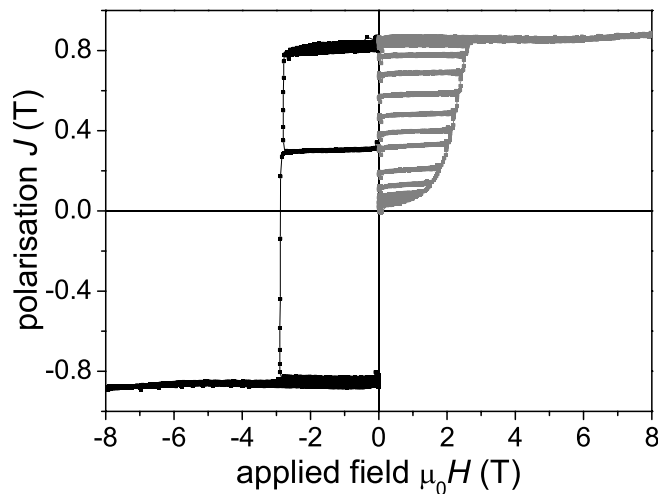


**Fig. 6.16:** Measured recoil loops for SmCo<sub>5</sub> film on MgO(110) substrate. Almost the entire sample magnetisation reverses at one reverse field value, indicating strong coupling between crystallites.

films on IBAD MgO substrate (Fig. 6.17). The value reaches the highest achievable value for  $\delta J$  ( $\delta J = 2$ ) from purely theoretical considerations, confirming once again that the grains are strongly exchange coupled. The origin of this strong exchange coupling in SmCo<sub>5</sub> films on MgO(110) substrates is believed to be the high quality of crystallographic texture with a grain misorientation angle as low as  $3^\circ$  (deduced from FWHM in pole figure measurements) along with the small grain sizes. Both the factors together lead to the formation of large, interaction domains spreading over

several sub-100 nm sized grains, which however needs absolute confirmation from MFM work.

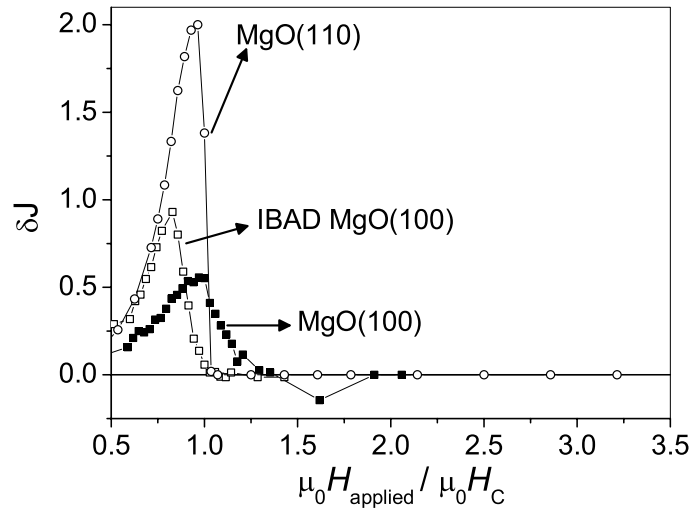


**Fig. 6.17:** Comparison of measured  $\delta J$  on MgO(110), MgO(100) and on IBAD MgO films. The strongest  $\delta J$  peak is observed in films on MgO(110) substrates, directly showing the maximum exchange coupling in the system due to strongly aligned crystallites.

## 6.2.2 Summary and Discussion on Intergranular Coupling

Epitaxially prepared SmCo<sub>5</sub> films and Sm<sub>2</sub>Co<sub>7</sub> films on different substrates, namely MgO(100) and MgO(110) single crystal substrates and MgO(100) buffered IBAD substrates, were investigated for verification of intergranular exchange. The intergranular coupling in the samples was probed by measuring  $\delta J$  plots, which give a measure of deviation from ideal Wohlfarth relation for non-interacting systems. All the samples, irrespective of the texture or orientation of the substrates, were found to be exchange coupled due to the observations of a positive peak in the  $\delta J$  plots [Bea91], [Min91], [Zha03]. However, the amount of exchange coupling, measured by the amplitude of the positive deflection in the  $\delta J$  plot, was found to be strongly dependent on the thickness of the SmCo<sub>5</sub> film and it increased with lowering the film thickness. This effect is attributed to the increase in grain size of the SmCo<sub>5</sub> layer with increasing film thickness, as seen through TEM studies, which lowers the interaction area and hence the exchange coupling. The grain sizes in Sm-Co samples could further be manipulated by using IBAD buffer layers on amorphous SiN/Si substrates. The small grain sizes of cube-textured MgO buffer layers prepared with IBAD on a-Si substrates are well replicated in the Sm-Co layer. The exchange coupling is found to increase by more than four times for films on IBAD MgO substrates as compared to films of similar thickness on single crystal substrates. This huge increase is brought about by the reduced Sm-Co grain size on IBAD substrates, which increases the interaction area effecting a stronger exchange coupling on these substrates compared to films on single crystal substrates. An independent and equally

important factor tuning exchange coupling in continuous Sm-Co films is the crystallographic texture of these films. Uni-axially textured SmCo<sub>5</sub> films with narrow texture spreads of approx. 3° on MgO(110) single crystal substrates, open the way to achieving highest possible limits of exchange coupling. The grains in the film show very sharp and collective reversal at one distinctly narrow switching field bringing the textured system close to behaving like a single grain system.

## 7 Conclusions and Future Work

The purpose of this work was to establish epitaxial growth of Sm-Co thin films with pulsed laser deposition on Cr buffered MgO substrates of different textures and orientations and to correlate the measured extrinsic magnetic properties with intrinsic magnetic properties of Sm-Co compounds and the film microstructure. Epitaxial growth of  $\text{Sm}_2\text{Co}_7$  was analysed on MgO(100) single crystal substrates. Films were deposited at several deposition temperatures with a constant laser repetition rate of 15 Hz. At deposition temperatures higher than 600 °C,  $\text{Sm}_2\text{Co}_7$  films grow epitaxially with two independent epitaxial relations, namely  $\text{Sm}_2\text{Co}_7[0001] (11\bar{2}0) \parallel \text{Cr}[110] (001) \parallel \text{MgO}[100] (001)$  and  $\text{Sm}_2\text{Co}_7(11\bar{2}16) \parallel \text{Cr}[110] (001) \parallel \text{MgO}[100] (001)$  confirmed from pole figure measurements. The first one results from (11 $\bar{2}$ 0) planes of  $\text{Sm}_2\text{Co}_7$  crystallites parallel to MgO(100) planes and, hence, corresponds to the  $\text{Sm}_2\text{Co}_7$  c-axis lying perfectly in-plane along MgO[100] and along MgO[010]. The latter results from a set of  $\text{Sm}_2\text{Co}_7$  crystallites which have their (11 $\bar{2}$ 16) planes parallel to MgO(100) planes and, therefore, have their c-axis pointing 60° out of plane. Overall, the film has weak in-plane magnetic anisotropy due to the two competing epitaxial relations. Although the first epitaxial relation was reported earlier by Liu *et al.* and Fullerton *et al.* [Liu95], [Ful97], the 60° tilted component has never been observed or reported before. Lower deposition temperatures improve magnetic and crystallographic anisotropy. At a deposition temperature of 550 °C, pole figure measurements show that the c-axis lies only along MgO[100] and MgO[010], i.e. perfectly in-plane and without 60° contribution. The best value of magnetic texture was, however, limited to 0.5 and therefore even lower temperatures were desirable which were, however, inaccessible due to incomplete phase formation below 450 °C. the phase formation was improved by lowering the laser repetition rate and thereby providing the growing film more time for rearranging its crystallites and enable complete phase formation. At 2 Hz repetition rate, films with magnetic texture better than 0.1 could be grown and lower repetition rates seem promising for extending the film growth to lower deposition temperatures. An extended temperature series of films from 600 °C down to 350 °C was attempted at 5 Hz laser repetition rate. Excellent magnetic texture of 0.02 and high coercivity of 2.4 T was obtained at 400 °C and 5 Hz repetition rate along the easy axis.  $\text{Sm}_2\text{Co}_7$  grows epitaxially at these low temperatures with two orthogonal c-axes in-plane.

The epitaxial growth of Sm-Co was extended to  $\text{SmCo}_5$  due to its superior intrinsic properties. This phase was grown epitaxially on Cr buffered MgO(100) substrates. Phase purity and texture

were confirmed by XRD and several pole figure measurements. The  $2\theta$  positions of several reflections were measured in the sample and matched with one or the other Sm-Co phase. For three of the four poles measured, namely the  $(11\bar{2}0)$ ,  $(11\bar{2}1)$ ,  $(0002)$  and  $(10\bar{1}7)$ , the  $2\theta$  positions were closer to the  $\text{SmCo}_5$  phase than to the  $\text{Sm}_2\text{Co}_7$  phase. Moreover, the complete absence of  $(10\bar{1}7)$  reflection in the sample is nicely in agreement with the film being  $\text{SmCo}_5$ , since this reflection exists in the  $\text{Sm}_2\text{Co}_7$  phase and is absent for the  $\text{SmCo}_5$  phase. Magnetic measurements show a higher remanence polarisation of 0.71 T along  $\text{MgO}[110]$  for this film which is about 40% higher than epitaxial  $\text{Sm}_2\text{Co}_7$  films and is very well in accordance with the maximum achievable remanent polarisation ( $0.7 J_S$ ) for the twin c-axis growth.

A successful increase in the remanent polarisation from  $\text{Sm}_2\text{Co}_7$  to  $\text{SmCo}_5$  with an increase in Co content motivated a film series to investigate the effect of varying Co content on magnetic properties. Films with a Sm content from 14 at.% to 23 at. % were epitaxially deposited. The monotonic increase in the d spacing with increasing Sm content indicated that the Sm-Co unit cell was actually following the intended structural variation. At low Sm contents ( $\sim 12\text{--}14$  at.% Sm) films with  $\text{SmCo}_7$  phase were realised, higher Sm contents (16 at.%) lead to  $\text{SmCo}_5$  and at even larger Sm contents the  $\text{Sm}_2\text{Co}_7$  phase was expected from the observed lattice spacing. Remanent polarisation increased with lowering Sm content up to 0.7 T at 14 at.% Sm along the easy axis while maintaining a high  $\mu_0 H_C > 2$  T and magnetic texture better than 0.1.

$\text{Sm}_2\text{Co}_7$  films were deposited on cube textured  $\text{MgO}(100)$  buffered amorphous  $\text{SiN}/\text{Si}(100)$  substrates for comparison. The rest of the layer scheme was kept the same and the Sm-Co layer was sandwiched between additional Cr buffer and cover layer. Pole figure measurements show an epitaxial growth of  $\text{Sm}_2\text{Co}_7$  films on the  $\text{MgO}(100)$  buffer with a higher texture spread of  $10^\circ$  which is directly taken over from the large texture spread of  $12^\circ$  for  $\text{MgO}$ . The film has a much higher  $\mu_0 H_C$  of 3.6 T at 120 nm thickness compared to 2 T for similar films on  $\text{MgO}(100)$  single crystal substrates. The much smaller grain size of 20 nm in  $\text{MgO}$  buffer, which is transferred to the  $\text{Sm}_2\text{Co}_7$  layer, is responsible for the higher coercivity. Perfectly square-shaped hysteresis along the easy axis and very flat and narrow hysteresis out-of-plane vouch for an ideal magnetic texture in these films. Since the coercivity increases inversely proportional to grain size, further modulation of the coercivity based on various different grain sizes controlled by the  $\text{MgO}$  buffer or by the Sm-Co film thickness would be some attractive future works.

The twin c-axes texture of  $\text{SmCo}_5$  on  $\text{MgO}(100)$  substrates prohibits remanences higher than 0.73 T in these films along any of the substrate directions. Although epitaxial growth of  $\text{SmCo}_5$  on  $\text{MgO}(100)$  makes the realisation of these high remanences feasible, it still is more than 30% smaller than the potential of  $\text{SmCo}_5$  ( $J_S = 1.1$  T). The only way to achieve these high remanences is to have a growth texture in these films that causes all the saturation polarisation of  $\text{SmCo}_5$  to drop along one direction. And this limitation requires uniaxial  $\text{SmCo}_5$  growth. On  $\text{MgO}(110)$  single

crystal substrates, epitaxial growth of SmCo<sub>5</sub> on Cr buffers was attempted. Cr grows epitaxially on MgO(110) substrate at 700 °C with the relation: Cr(211)[01 $\bar{1}$ ] || MgO(110)[1 $\bar{1}$ 0], however, from AFM investigations it was found that the morphology of the Cr buffer at a deposition temperature of 700 °C is very rough and discontinuous. Lowering the Cr deposition temperature from 700 °C to 300 °C improves Cr surface and it is found to be continuous with a low roughness of 0.2 nm. SmCo<sub>5</sub> films on these low temperature buffers grow perfectly epitaxial according to pole figure measurements as per: SmCo (10 $\bar{1}$ 0)[0001] || Cr (211)[00 $\bar{1}$ ] || MgO(110)[001] indicating a single growth direction of SmCo<sub>5</sub> c-axis parallel to MgO [001] direction. This texture is very well reproduced in magnetic measurements where a large square-shaped hysteresis is obtained only along the easy axis parallel to MgO[001] and the other two orthogonal MgO directions produce ideal hard axis loops. A remanence as high as 0.94 T with a coercivity > 3 T was obtained along the easy axis.

Epitaxial growth of Sm-Co on different substrates resulting in high coercivities and highest remanences, limited only by the texture on each individual substrate, was established. These films were ideal for analysing domain structures, magnetisation reversal mechanism or intergranular coupling. These investigations were performed on each of the individual Sm-Co textures. Detailed coercivity analysis in the framework of the micro-magnetic model by measuring temperature-dependent magnetic hystereses was performed. This kind of analysis, which correlates the extrinsic variable (coercivity) with the intrinsic property (anisotropy field) through the temperature independent variables  $\alpha_{\text{eff}}$  and  $N_{\text{eff}}$ , tries to answer the discrepancy between measured coercivities and the much higher theoretical anisotropy fields.  $\alpha_{\text{eff}} < 0.3$  is mainly attributed to predominant pinning in the system and vice versa, a higher  $\alpha_{\text{eff}}$  is due to nucleation dominated reversal. On MgO(100) substrates,  $\alpha_{\text{eff}}$  values of 0.17 and 0.08 are obtained respectively for a 50 nm and a 150 nm thick film. This decrease in  $\alpha_{\text{eff}}$  value for a thicker film suggests a weaker pinning ability of thick films and must result in lower coercivity as observed. Moreover, it is due to a deterioration of microstructure in thicker films, which however needs confirmation from TEM analysis. The analysis was performed along two independent in-plane directions, MgO[100] and MgO[110], of Sm-Co films on MgO(100) substrate, to investigate the effect of the twin c-axes distribution. The  $\alpha_{\text{eff}}$  values are higher along the MgO[110] direction for both the thick and the thin film and could be explained by considering the directional dependence of  $\alpha_{\text{eff}}$  coming from  $\alpha_{\phi}$ .  $\alpha_{\phi}$  follows an inverse  $\cos \theta$  dependence in pinning-dominated systems and, therefore, at 45° in-plane direction an increase of coercivity by a factor of 1.4 is expected. The measured increase in coercivity along 45° is in accordance with the expected value to within a 5% error. This investigation independently proves a pinning controlled magnetisation reversal in Sm<sub>2</sub>Co<sub>7</sub> thin films on MgO(100) single crystal substrates.

Similar analysis was performed on comparative films on MgO(100) buffered Si substrates. The

$\alpha_{\text{eff}}$  value of 0.15 was higher than the 0.1 value on MgO(100) single crystal substrates and in accordance with the higher coercivity on MgO buffered Si substrates than on single crystals. The higher coercivity on MgO buffered Si substrate is thought to arise from the smaller Sm-Co grain size which results in more grain boundaries and, hence, effective pinning.

SmCo<sub>5</sub> films on MgO(110) single crystals result in  $\alpha_{\text{eff}}$  of 0.18 which is the highest value for any other substrate measured along the easy axis. The high value of  $\alpha_{\text{eff}}$  suggests strong and more effective pinning of domain walls on MgO(110) substrates. The pinning is more effective on these substrates due to a much stronger and aligned c-axis which leads to larger interaction domains. Detailed TEM investigations complimented with lacking (Magnetic Force Microscopy) MFM work or other domain imaging techniques could provide the necessary insight into deeper understanding of pinning phenomena.

The amount of intergranular exchange was probed in Sm-Co samples on various substrates by measuring recoil loops and constructing  $\delta M$  plots. If  $\delta M$  is directly proportional to the amount of intergranular exchange, then on MgO(100) substrates thinner SmCo<sub>5</sub> films (50 nm) are more strongly exchange coupled compared to thicker SmCo<sub>5</sub> films. The exchange coupling in IBAD MgO(100) samples is then approx. four times stronger than for a comparable film on single crystal substrate, only to be surpassed by incomparable exchange coupling of SmCo<sub>5</sub> films on MgO(110) single crystals substrates. The amount of exchange coupling in SmCo<sub>5</sub> films is inversely proportional to the grain size and, therefore, the smaller the grain size the larger is the exchange coupling. Since Sm-Co grows columnar and the vertical grain dimension is the same as the film thickness, the simplest way of reducing the grain size was by reducing the film thickness and the effect is directly visible in thick and thin SmCo<sub>5</sub> films on MgO(100) substrate. IBAD MgO substrates offer another source of imposing a practical limit on maximum achievable grain sizes in the Sm-Co film by restricting the grain size of the pseudo-substrate. The highest exchange coupling was, however, observed on MgO(110) substrates for comparable grain sizes of Sm-Co films. Therefore, degree and nature of the crystallographic texture is another important parameter deciding intergranular exchange. An almost perfect parallel alignment of grains on MgO(110) substrates due to a good uniaxial Sm-Co texture, in contrast to orthogonal c-axis alignment, and therefore the Sm-Co grains on MgO(100) substrate can be argued as the reason for higher exchange in Sm-Co films on MgO(110).

# Bibliography

- [Aha58] A. Aharoni and S. Shtrikman. Magnetisation curve of infinite cylinder. *Phys. Rev.*, 109(5), 1522, 1958.
- [Aha60] A. Aharoni. Reduction in coercive force caused by a certain type of imperfection. *Phys. Rev.*, 119, 127, 1960.
- [Alo95] I. A. Al-Omari and D. J. Sellmyer. Magnetic properties of nanostructured CoSm/FeCo films. *Phys. Rev.*, 52, 3441, 1995.
- [Bar76] B. Barbara and M. Uehara. Anisotropy and coercivity in SmCo<sub>5</sub> based compounds. *IEEE Trans. Magn.*, MAG-12, 997, 1976.
- [Bea91] I. A. Beardsley and J. Zhu. Significance of  $\delta M$  measurements in thin film media. *IEEE Trans. Magn.*, 27, 5037, 1991.
- [Bec72] J. J. Becker. Angular dependence of nucleating fields in Co-rare earth particles. *From 17th annual conference on magnetism and magnetic materials*, 5, 1067, 1972.
- [Ben98] M. Benaissa, K. M. Krishnan, E. E. Fullerton, and J. S. Jiang. Magnetic anisotropy and its microstructural origin in epitaxially grown SmCo thin films. *IEEE Trans. Magn.*, 34, 1204, 1998.
- [Bre62] F. Breech and L. Cross. Optical microemission stimulated by a ruby maser. *Appl. Spectrosc.*, 16, 59, 1962.
- [Bol03] A. Bollero. Isotropic Nanocrystalline (NdPr)(FeCo)B *Dissertation*, 2003.
- [Bro45] W. F. Brown Jr. Virtues and weaknesses of the domain concept. *Rev. Mod. Phys.*, 17, 15, 1945.
- [Bud02] T. Budde and H. H. Gatzert. Patterned sputter deposited SmCo-films for MEMS applications. *J. Magn. Magn. Mater.*, 242, 1146, 2002.
- [Bus98] K. H. J. Buschow. Permanent magnet materials and their applications. *Trans. Tech Publications Ltd.*, 1998.

- [Coe96] J. M. D. Coey (Editor). Rare earth iron permanent magnets. *Oxford Science Publication*, 1996.
- [Cad87a] F. J. Cadieu, T. D. Cheung, L. Wichramasekara, N. Kamprath, H. Hegde, and N. C. Liu. The magnetic properties of high  $H_C$  Sm-Co, Nd-Fe-B and Sm-Ti-Fe films crystallised from amorphous deposits. *J. Appl. Phys.*, 62, 3866, 1987.
- [Cad87b] J. M. Cadogan, J. P. Gavigantt, D. Givordt, and H. S. Li. A new approach to the analysis of magnetisation measurements in rare-earth transition-metal compounds: Application to Nd<sub>2</sub>Fe<sub>14</sub>B. *J. Phys. F: Met. Phys.*, 18, 779, 1987.
- [Cad94] F. J. Cadieu and H. Hedge. In-plane magnetised YIG substrates self biased by Sm-Co based sputtered film coatings. *J. Appl. Phys.*, 76, 6059, 1994.
- [Cad98] F. J. Cadieu, R. Rani, X. R. Qian, and Li. Chen. High coercivity SmCo based films made by pulsed laser deposition. *J. Appl. Phys.*, 83, 6247, 1998.
- [Cad99] F. J. Cadieu, R. Rani, T. Theodoropoulos, and Li. Chen. Fully in plane aligned SmCo based films prepared by pulsed laser deposition. *J. Appl. Phys.*, 85, 5895, 1999.
- [Cam72] I. A. Campbell. Indirect exchange for rare earth in metals. *J. Phys. F: Met Phys.*, 2, L47, 1972.
- [Che93] K. Chen, H. Hedge, S. U. Jen, and F. J. Cadieu. Different kinds of anisotropies in Sm-Co thin films. *J. Appl. Phys.*, 73, 5923, 1993.
- [Che97] S. K. Chen, J. L. Tsai, and T. S. Chin. Coercivity and transmission electron microscopy study of nanocomposite Sm-Co powders by mechanical alloying. *J. Appl. Phys.*, 81, 5631, 1997.
- [Cho69] K. L. Chopra. Thin film phenomenon. *McGraw Hill, New York*, 1969.
- [Cre02] D. C. Crew, E. Girt, D. Suess, T. Schrefl, K. M. Krishnan, G. Thomas, and M. Guilot. Magnetic interactions and reversal behavior of Nd<sub>2</sub>Fe<sub>14</sub>B particles diluted in a Nd matrix. *Phys. Rev. B*, 66, 184418–1, 2002.
- [Cul72] Cullity. Introduction to magnetic materials. *Addison-Wesley Series in Metallurgy and Materials*, 1972.
- [Car31] CaRIne crystallograpy version. 3.1.
- [DeB59] R. W. DeBlois and C. P. Bean. Domain observations in iron whiskers. *J. Appl. Phys.*, 29, 528, 1959.

- [Der79] A. V. Deryagin. Magnetic moment, magnetic anisotropy and spin reorientation phase transition in (4f-3d)-intermetallic compounds. *Journal De Physique*, C5, 165, 1979.
- [Dij87] D. Dijkkamp, T. Venkatesan, X. D. Wu, S. A. Shaheen, N. Jisrawi, Y. H. Minlee, W. L. Mclean, and M. Croft. Preparation of Y-Ba-Cu oxide superconductor thin films using pulsed laser deposition from high  $T_C$  bulk material. *Appl. Phys. Lett*, 51, 619, 1987.
- [Elb91] D. Elbaz, D. Givord, S. Hirosawa, F. P. Missell, M. F. Rossignol, and V. Villas-Boas. Angular dependence of coercivity in sintered RFeB magnets. *J. Appl. Phys.*, 69, 5492, 1991.
- [Erm76] A. S. Ermolenko. Magnetocrystalline anisotropy of rare earth intermetallics. *IEEE transactions on Magnetism*, MAG-12, 992, 1976.
- [Fra49] F. C. Frank and J. H. van der Merwe. One-dimensional dislocations. *Proc. Roy. Soc. A* 189, 205, 1949.
- [Ful96] E. E. Fullerton, C. H. Sowers, J. P. Pearson, S. D. Bader, X. Z. Zu, and D. Lederman. A general approach to epitaxial growth of rare-earth-transition-metal films. *Appl. Phys. Lett.*, 69, 2438, 1996.
- [Ful97] E. E. Fullerton, C. H. Sowers, J. E. Pearson, S. D. Bader, J. B. Patel, X. Z. Wu, and D. Lederman. Structure and magnetism of rare-earth-transition-metal films. *J. Appl. Phys.*, 81(8), 5637, 1997.
- [Gar00] J. Garcia-Otero, M. Porto, and J. Rivas. Henkel plots of single-domain ferromagnetic particles. *J. Appl. Phys.*, 87, 7376, 2000.
- [Giv88a] D. Givord, P. Tenaud, and T. Viadieu. Angular dependence of coercivity in sintered magnets. *J. Magn. Magn. Mater.*, 72, 247, 1988.
- [Giv88b] D. Givord, P. Tenaud, and T. Viadieu. Coercivity mechanisms in ferrites and rare earth transition metal sintered magnets (SmCo<sub>5</sub>, Nd-Fe-B). *IEEE Trans. Magn.*, T-MAG, 1921, 1988.
- [Giv91] D. Givord, Q. Lu, and M. F. Rossignol. Coercivity in hard magnetic materials. *Sc. and Tech of Nano Stru. Magn. Mat. Edited by Hadjipanayis*, page 635, 1991.
- [Giv03] D. Givord. Magnetic materials: From the search of new phases to nanoscale engineering. *Europhysics News*, 34, 1, 2003.
- [God65] J. Goddard and J. G. Wright. Magnetic anisotropy in electrodeposited single crystal films of cobalt. *Brit. J. Appl. Phys.*, 16, 1251, 1965.

- [Gri98] M. Grimsditch, J. S. Jiang, E. E. Fullerton, and C. H. Sowers und S. D. Bader. Exchange-spring behavior in epitaxial hard/soft magnetic bilayers. *Phys. Rev. B*, 58, 12193, 1998.
- [Gut04] O. Gutfleisch, N. M. Dempsey, A. Yan, K.-H. Müller, and D. Givord. Coercivity analysis of melt-spun  $\text{Sm}_2(\text{Co, Fe, Cu, Zr})_{17}$ . *J. Magn. Magn. Mat.*, 272, 647, 2004.
- [Han03] U. Hannemann, S. Fähler, V. Neu, B. Holzapfel, and L. Schultz. Intrinsic and extrinsic properties of epitaxial  $\text{Nd}_2\text{Fe}_{14}\text{B}$  films. *Appl. Phys. Lett.*, 82, 3710, 2003.
- [Heg93] H. Hegde, S. U. Jen, K. Chen, and F. J. Cadieu. Film Sm-Co permanent magnets for biasing of thin permalloy strips. *J. Appl. Phys.*, 73, 5926, 1993.
- [Hen64] O. Henkel. Remanenzverhalten und Wechselwirkung in hartmagnetischen Teilchenkollektiven. *Physica Status Solidi*, 7, 919, 1964.
- [Hol92] B. Holzapfel, B. Roas, L. Schultz, P. Bauer, and G. Saemann-Ischenko. Off-axis laser deposition of  $\text{YBa}_2\text{Cu}_7\text{O}_{7-\delta}$  thin films. *Appl. Phys. Lett.*, 61, 3178, 1992.
- [Hüh01] R. Hühne, C. Beyer, B. Holzapfel, C.-G. Oertel, L. Schultz, and W. Skrotzki. Formation and destruction of cube texture in MgO films using ion beam assisted pulsed laser deposition. *J. Appl. Phys.*, 90, 1035, 2001.
- [Kir96] H. R. Kirchmayr. Permanent magnets and hard magnetic materials. *J. Phys. D: Appl. Phys.*, 29, 2763, 1996.
- [Kon40] E. Kondorsky. On hysteresis in ferromagnets. *J. Phys. USSR*, 2, 161, 1940.
- [Kou94] X. C. Kou, H. Kronmüller, D. Givord, and M. F. Rossignol. Coercivity mechanism of sintered  $\text{Pr}_{17}\text{Fe}_{75}\text{B}_8$  and  $\text{Pr}_{17}\text{Fe}_{53}\text{B}_{30}$  permanent magnets. *Phys. Rev. B*, 50, 3849, 1994.
- [Kro85] H. Kronmüller. The nucleation fields of uniaxial ferromagnetic crystals. *Phys. Stat. Sol. (b)*, 130, 197, 1985.
- [Kro87] H. Kronmüller, K.-D. Durst, and G. Martinek. Angular dependence of coercive field in sintered  $\text{Fe}_{77}\text{Nd}_{15}\text{B}_8$  magnets. *J. Magn. Magn. Mater.*, 69, 149, 1987.
- [Kro88] H. Kronmüller, K.-D. Durst, and M. Sagawa. Analysis of the magnetic hardening mechanism in RE-FeB permanent magnets. *J. Magn. Magn. Mater.*, 74, 291, 1988.
- [Kub99] M. Kubis, A. Handstein, B. Gebel, O. Gutfleisch, K.-H. Müller, and L. Schultz. Highly coercive  $\text{SmCo}_5$  magnets prepared by a modified hydrogenation-disproportionation-desorption-recombination process. *J. Appl. Phys.*, 85, 5666, 1999.

- [Kum86] K. Kumar and D. Das. Aligned plasma sprayed  $\text{SmCo}_5$  deposits. *J. Appl. Phys.*, 60, 3779, 1986.
- [Kum88] K. Kumar.  $\text{RETM}_5$  and  $\text{RE}_2\text{TM}_{17}$  permanent magnet development. *J. Appl. Phys.*, 63, R-13, 1988.
- [Liu95] Y. Liu, B. W. Robertson, Z. S. Shan, S. H. Liou, and D. J. Sellmyer. Microstructure of the Cr underlayer and its effect on Sm-Co thin films. *J. Appl. Phys.*, 77, 3831, 1995.
- [Liu96] Y. Liu, D. J. Sellmyer, and B. W. Robertson. Co-Sm  $(\bar{1}100)[0001]/\text{Cr}(\bar{1}2\bar{1})[\bar{1}01]$  epitaxy and its effect on magnetic properties of Co-Sm/Cr films. *J. Appl. Phys.*, 79, 5333, 1996.
- [Liu02] S. Y. Liu, J. Zhou, Y. Liu, R. Skomski, and D. J. Sellmyer. TEM of nanostructure of Cu and Ti doped Sm-Co magnetic materials. *Microscopy and Microanalysis*, 8, 1358, 2002.
- [Mad66] S. Mader. The use of thin films in physical investigations. ed. J. C. Anderson, *Academic Press, New York*, 1966.
- [Mei56] W. H. Meiklejohn and C. P. Bean. New magnetic anisotropy. *Phys. Rev.*, 105, 904, 1956.
- [Men74] A. Menth, H. P. Klein, J. Bernasconi, and S. Strässler. Magnetic properties of  $\text{RECo}_5$  permanent magnets. *American Institute of Physics - Conf. Proc.*, 18(2), 1182, 1974.
- [Min91] T. Min, J. Zhu, and J. H. Judy. Effects of inter-layer magnetic interactions in multilayered CoCrTa / Cr thin film media. *IEEE Trans. on Magnetism*, 27, 5058, 1991.
- [Neu98] V. Neu. Austauschgekoppelte nanokristalline Nd-Fe-B-Magnetpulver durch mechanisches Legieren. *Dissertation*, 1998.
- [Neu99] V. Neu and S. A. Shaheen. Sputtered Sm-Co films – microstructure and magnetic properties. *J. Appl. Phys.*, 86, 7006, 1999.
- [Neu02a] V. Neu, S. Fähler, B. Holzapfel, and L. Schultz. Hard magnetic Sm-Co thin films prepared by pulsed laser deposition. *J. Magn. Magn. Mat.*, 242, 1290, 2002.
- [Neu02b] V. Neu, U. Hannemann, S. Fähler, and L. Schultz. Effect of rare earth content on microstructure and magnetic properties of Sm-Co and Nd-Fe-B thin films. *J. Appl. Phys.*, 91, 8180, 2002.
- [Ohr91] M. Ohring. The material science of thin films. *Academic Press - London*, 1991.

- [Pas95] Y. G. Pastushenkov. Angular dependence of magnetisation reversal critical fields in individual grains of  $RE$ -Fe-B magnets. *J. Magn. Magn. Mag.*, 140, 1063, 1995.
- [Pas96] Y. G. Pastushenkov, O. B. Dyogteva, A. W. Shipov, and K. P. Skokov. Magnetostatic grain interaction and angular dependence of the nucleation field in Fe-Nd-B and  $SmCo_5$  permanent magnets. *J. Magn. Magn. Mag.*, 157, 67, 1996.
- [Pin04] E. Pina, M. A. Gracia, I. Carabias, F. J. Palomares, F. Cebollada, A. de Hoyos, R. Almazan, M. I. Verdu, M. T. Montojo, G. Vergara, A. Hernando, and J. M. Gonzalez. Temperature dependence of the hysteretic properties in SmCo films. *J. Magn. Magn. Mat.*, 272, 833, 2004.
- [Pow02] N. Powers, M. L. Yan, L. Gao, S. H. Liou, and D. J. Sellmyer. Magnetic intergranular interaction in nanocomposite  $Co_xPt_{100-x}:C$  thin films. *J. Appl. Phys.*, 91, 8641, 2002.
- [Pra99] C. Prados and G. C. Hadjipanayis. Sm(Co, Cu, Ni) thin films with giant coercivity. *Appl. Phys. Lett.*, 74, 430, 1999.
- [Rad87] R. J. Radwanski and J. J. Franse. Rare-earth contribution to the magnetocrystalline anisotropy energy in  $R_2Fe_{14}B$ . *Physical Review B*, 36, 8616, 1987.
- [Rad02] R. J. Radwanski, R. Michalskia, Z. Ropka, and A. Blauta. Crystal-field interactions and magnetism in rare-earth transition-metal intermetallic compounds. *Physica B*, 319, 78, 2002.
- [Reh97] Ch. Rehm, E. E. Fullerton, J. S. Ziang, C. H. Sowers, S. D. Bader, J. B. Patel, and X. Z. Zu. High coercivity, epitaxial Sm-Co films with uniaxial in-plane anisotropy. *Appl. Phys. Lett.*, 71, 1579, 1997.
- [Rei65] S. Reich, S. Shtrikman, and D. Treves. Angular variation of coercivity in orthoferrite single crystals. *J. Appl. Phys.*, 36, 140, 1965.
- [Ric98] M. Richter. Band structure theory of magnetism in 3d-4f compounds. *J. Phys. D: Appl. Phys.*, 31, 1017, 1998.
- [Roa88] B. Roas, L. Schultz, and G. Endres. Epitaxial deposition of  $YBa_2Cu_3O_{7-x}$  thin films by a laser evaporation process. *Appl. Phys. Lett.*, 53, 1557, 1988.
- [Rom00] S. A. Romero, D. R. Cornejo, F. M. Rhen, A. C. Neiva, M. H. Tabacniks, and F. P. Missell. Magnetic properties and underlayer thickness in Sm-Co/Cr films. *J. Appl. Phys.*, 87, 6965, 2000.

- [San75] S. G. Sankar, V. U. S. Rao, E. Segal, W. E. Wallace, W. G. Frederick, and H. J. Garrett. Magnetocrystalline anisotropy of  $\text{SmCo}_5$  and interpretation on a crystal field model. *Phys. Rev. B*, 11, 435, 1975.
- [Say05a] J. Sayama, T. Asahi, K. Mizutani, and T. Osaka. Newly developed  $\text{SmCo}_5$  films with perpendicular magnetic anisotropy. *J. Phys. D: Appl. Phys.*, 37, L1, 2005.
- [Say05b] J. Sayama, K. Mizutani, T. Asahi, J. Ariake, K. Ouchi, S. Matsunuma, and T. Osaka. Magnetic properties and microstructure of  $\text{SmCo}_5$  thin film with perpendicular magnetic anisotropy. *J. Magn. Magn. Mag.*, 287, 239, 2005.
- [Say05c] J. Sayama, K. Mizutani, and T. Asahi und T. Osaka. Thin films of  $\text{SmCo}_5$  with very high perpendicular magnetic anisotropy. *Appl. Phys. Lett.*, 85, 5640, 2005.
- [Sch03] W. Scholz, Th. Schrefl, J. Fidler, Th. Matthias, D. Suess, and V. Tsiantos. Micromagnetic simulation of the pinning and depinning process in permanent magnets. *IEEE Trans. Magn.*, 39, 2920, 2003.
- [Sht57] S. Shtrikman, E. H Frie, and D. Treves. Critical size and nucleation field of ideal ferromagnetic particles. *Phys. Rev.*, 103, 447, 1957.
- [Sko99] R. Skomski and J. M. D. Coey. Permanent magnetism. *Institute of Physics publishing – Bristol and Philadelphia*, 1999.
- [Sko03] R. Skomski. Nano-magnetics. *J. Phys.: Condens. Matter*, 15, R–841, 2003.
- [Smi65] H.M. Smith and A.F. Turner. Vacuum deposited thin films using a ruby laser. *Appl. opt.*, 4, 147, 1965.
- [Sow98] C. H. Sowers, J. S. Jiang, E. E. Fullerton, J. E. Pearson, and S. D. Bader. Structure and magnetic properties of exchange-spring Sm-Co/Co superlattices. *Appl. Phys. Lett.*, 72, 380, 1998.
- [Sto48] E. C. Stoner and E. P. Wohlfarth. A mechanism of magnetic hysteresis in heterogenous alloys. *Phil. Trans. Roy. Soc.*, 240A, 599, 1948.
- [Str67] K. Strnat, G. Hoffer, J. Olson, W. Ostertag, and J. J. Becker. A family of new cobalt-base permanent magnet materials. *J. Appl. Phys.*, 38, 1001, 1967.
- [Str72] K. J. Strnat. Hard magnetic properties of rare-earth transition metal alloys. *IEEE Trans. on Magn.*, 8, 511, 1972.

- [Str79] R. L. Streever. Individual Co site distributions to the magnetic anisotropy of  $R\text{Co}_5$  compounds and related structures. *Phys. Rev. B*, 19, 2704, 1979.
- [Str82] G. B. Stringfellow. Epitaxy. *Rep. Prog. Phys.*, 45, 469, 1982.
- [Szp79] B. Szpunar and P. A. Lindgard. On the origin of the large magnetic anisotropy of rare earth-cobalt compounds. *J. Phys. F: Metal Phys.*, 9, L55, 1979.
- [Tam05] R. Tamm, A. Singh, V. Neu, K. S. Rao, W. Skrotzki, C. G. Oertel, S. Fähler, L. Schultz, and B. Holzapfel. Temperature dependence of the texture of Sm-Co films. *Solid State Phenomena*, 105, 409, 2005.
- [Tan01] W. Tang, A. M. Gabay, Y. Zhang, G. C. Hadjipanayis, and H. Kronmüller. Temperature dependence of coercivity and magnetisation reversal mechanism in  $\text{Sm}(\text{Co}_{bal}\text{Fe}_{0.1}\text{Cu}_y\text{Zr}_{0.04})_{7.0}$ . *IEEE Trans. Magn.*, 37, 2515, 2001.
- [Tat70] E. Tatsumoto, T. Okamoto, H. Fujii, and C. Inque. Saturation magnetic moment and crystalline anisotropy of single crystals of light rare earth Co compounds  $R\text{Co}_5$ . *J. Phys. Colloq.*, 32(C1), 550, 1970.
- [Tel97] J. C. Telléz-Blanco, X. C. Kou, R. Groessinger, E. Estevez-Rams, J. Fiedler, and B. M. Ma. Coercivity and magnetic anisotropy of sintered  $\text{Sm}_2\text{Co}_{17}$ -type permanent magnets. *J. Appl. Phys.*, 82, 3928, 1997.
- [Tre05] E. du Tremolet de Lacheisserie, D. Gignoux, and M. Schlenker (Editors). Magnetism – Materials and Applications. *Springer*, 2005.
- [Tro90] S. R. Trout. Permanent magnets based on the lanthanides. *Proceedings of the international symposium on magnetism*, page 79, 1990.
- [Vel94] E. M. Velu, D. N. Lambeth, J. T. Thornton, and P. E. Russell. AFM structure and media noise of Sm-Co/Cr thin films and hard disks. *J. Appl. Phys.*, 75, 6132, 1994.
- [Wan03] Z. Wang, G. Christiani, and H.-U. Habermeier. Uniaxial magnetic anisotropy and magnetic switching in  $\text{La}_{0.67}\text{Sr}_{0.33}\text{MnO}_3$  thin films grown on vicinal  $\text{SrTiO}_3$  (100). *Appl. Phys. Lett.*, 21, 3731, 2003.
- [Woh58] E. P. Wohlfarth. Relations between different modes of acquisition of the remanent magnetisation of ferromagnetic particles. *J. Appl. Phys.*, 29, 595, 1958.
- [Yan00] F. Y. Yang, C. L. Chien, E. F. Ferrari, X. W. Li, G. Xiao, and A. Gupta. Uniaxial anisotropy and switching behaviour in epitaxial  $\text{CrO}_2$  films. *Appl. Phys. Lett.*, 77, 286, 2000.

- [Yan05] A. Yan, A. Handstein, T. Gemming, K.-H. Müller, and O. Gutfleisch. Coercivity mechanism of  $\text{Sm}_2(\text{Co}, \text{Cu}, \text{Fe}, \text{Zr})_{17}$ -based magnets prepared by melt-spinning. *J. Magn. Magn. Mat.*, 290, 1206, 2005.
- [Zan99] G. Zangari, B. Lu, Laughlin, and D. N. Lambeth. Structure and magnetic properties of Sm-Co thin films on Cr/Ag/Si templates. *J. Appl. Phys.*, 85, 5759, 1999.
- [Zha00] Z. D. Zhang, W. Liu, J. P. Liu, and D. J. Sellmyer. Metastable phases in rare-earth permanent-magnet materials. *J. Phys. D: Appl. Phys.*, 33, R217, 2000.
- [Zha03] H. Zhang, C. Rong, X. Du, J. Zhang, S. Zhang, and B. Shen. Investigation on intergrain exchange coupling of nanocrystalline permanent magnets by Henkel plot. *Appl. Phys. Lett.*, 82, 4098, 2003.
- [Zha05] J. Zhang, Y. K. Takahashi, R. Gopalan, and K. Hono. Sm(Co, Cu)<sub>5</sub>/Fe exchange spring multilayer films with high energy product. *Appl. Phys. Lett.*, 86, 122509, 2005.
- [Zho00] J. Zhou, R. Skomski, C. Chen, G. C. Hadjipanayis, and D. Sellmeyer. Sm-Co-Cu-Ti high temperature permanent magnets. *Appl. Phys. Lett.*, 77, 1514, 2000.
- [Zho05] J. Zhou, R. Skomski, A. Kashyap, K. D. Sorge, Y. Sui, M. Daniil, and L. Gao. Highly coercive thin-film nanostructures. *J. Magn. Magn. Mater.*, 290-291, 227, 2005.



# Publication List

Some of the results in this work are published in the following:

1. A. Singh, V. Neu, S. Fähler, L. Schultz and B. Holzapfel. Effect of composition on phase formation and magnetic properties of highly coercive Sm-Co films. *J. Magn. Magn. Mater.*, 290-291, Part 2, 1259, 2005.
2. A. Singh, R. Tamm, V. Neu, S. Fähler, C.-G. Oertel, W. Skrotzki, L. Schultz, B. Holzapfel. Epitaxial growth of highly coercive Sm-Co thin films using pulsed laser deposition. *J. Appl. Phys.*, 97, 093902, 2005.
3. A. Singh, V. Neu, R. Tamm, K. Subba Rao, S. Fähler, W. Skrotzki, L. Schultz and B. Holzapfel. Growth of epitaxial SmCo<sub>5</sub> films on Cr/MgO[100] *Appl. Phys. Lett.*, 87, 072505, 2005.
4. A. Singh, V. Neu, R. Tamm, K. Rao, W. Skrotzki, S. Fähler, L. Schultz, B. Holzapfel. Pulsed laser deposited epitaxial Sm-Co thin films with uniaxial magnetic texture. *J. Appl. Phys.* in Press.
5. R. Tamm, A. Singh, V. Neu, K. Subba Rao, W. Skrotzki, C.-G. Oertel, S. Leinert, S. Fähler, L. Schultz, and B. Holzapfel. Temperature dependence of the texture of Sm-Co thin films *Solid State Phenomena*, 105, 409, 2005.
6. S. Fähler, V. Neu, M. Weisheit, U. Hannemann, S. Leinert, A. Singh, A. Kwon, S. Melcher, B. Holzapfel, and L. Schultz. High performance thin film magnets *18th int. Workshop on high performance magnets and their applications*, Vol. 2, 566, 2004.
7. S. Fähler, U. Hannemann, M. Weisheit, V. Neu, S. Melcher, S. Leinert, S. C. Wimbush, A. Singh, A. Kwon, B. Holzapfel, and L. Schultz. High performance thin film magnets *Appl. Phys. A*, 79, 1529, 2004.
8. V. Subramanya Sarma, J. Eickemeyer, A. Singh, L. Schultz and B. Holzapfel. Development of high strength and strongly cube textured Ni-4.5% W/Ni-15% Cr composite substrate for coated conductor application. *Acta Mater.*, 51, 4919, 2004.



# Acknowledgements

This one's one section of my thesis, that I think has been the most difficult to write – to remember everybody who made significant contributions towards finishing this work, scientifically and non-scientifically. And then I begin to wonder, how tiny my own contribution has been! But let me start, by thanking Dr. Bernhard Holzapfel - my project leader. Having known him for more than four years, the respect I hold for him has only increased over the years. He is one person with tremendous patience and capable of maintaining such a relaxed environment around him, always able to motivate you again, in the shortest of time spans. I can definitely not express enough, my gratitude towards him for showing the kind of faith in me which I'm still not certain of.

I'm truly grateful to Dr. Volker Neu, who introduced me into magnetism. His clarity in ideas made working and understanding things seem so easy. Even though several times probably it didn't seem so, and now I have the opportunity to do it, I would like to honestly acknowledge his guidance throughout my PhD work.

Equally important for me is to thank my Professor in the IFW, Prof. Ludwig Schultz, who provided me the opportunity to study and work at the same time at the IFW, and without which all my previous and subsequent acknowledgements would be meaningless. He despite an ever increasing number of PhD students, had the time to show his keen interest in my work repeatedly. This has been an institute where I was provided complete scientific freedom to work as I wanted, when I wanted, an opportunity I think is truly rare.

A special thanks is on the way for Dr. Sebastian Fähler for having spent hours and hours discussing my work and the work of all my colleagues, in the informative "SFB Meetings" along with weekly seminars and joint discussions on any available occasion. I would also like to thank Dr. Ruben Hühne for the IBAD MgO buffered Si/SiN substrates along with Dr. Brigitte Schlobach for High Resolution SEM imaging of these samples.

My gratitude is due to Roland Tamm who not only made all the pole figure measurements for me, but also made several attempts to make me understand them Without this very fruitful collaboration, a great deal of science would have been missing in this work. I would thank K. Subba Rao for TEM information on several samples and extend my acknowledgements to Prof. Skrotzki, also from the TU Dresden, for his kind cooperation and collaboration.

Among technical staff, I would like to begin with Ulrike Besold, who with her warm and friendly

smile was always a pleasure to work with. I never saw her complaining, she seems to be the most committed technical staff member who truly enjoys her work and makes you want to do the same. I should also quickly thank Stefan Pofahl for his constant help and patience at the chamber and in the lab with innumerable transfers, and Sandra Sieber for patterning samples.

I should not forget to thank several other members of the IFW/IMW whom I got to meet through table rule and otherwise! Some among them even became besides helpful colleagues, nice friends. Dr. Martin Weisheit, Ah-Ram Kwon, Karin Leistner, Kerstin Knoth, Tim Niemeier, Julia Lyubina, Jörg Buschbeck... for being absolutely ideal office mates and colleagues. Chatting with them scientifically and non-scientifically, although sometimes consuming most of the working day, was indeed very relaxing and poured in new experimental ideas and thoughts, which alone I would have never thought upon. I even like this idea of four people in one office and would encourage that!

It is very important for me to thank Jens Hänisch without whose constant assistance and motivation this work would never have been completed. I would thank him for having been by my side through all good and bad times.

I am utmost indebted to my parents, and I'm sure I can't thank them enough, who let me take this opportunity in life and do all the time what I wanted to do, even though many times it was against their better judgement. I also wish to thank them for having shown the kind of faith in me when I most needed it and for having been by my side through all circumstances always. I'm sure these four years without me were tougher for them than for me here.



